Fall 12-18-2014

Design and Software Validation of Coded Communication Schemes using Multidimensional Signal Sets without Constellation Expansion Penalty in Band-Limited Gaussian and Fading Channels

Milton I. Quinteros
University of New Orleans, mquinter@uno.edu

Recommended Citation

Quinteros, Milton I., "Design and Software Validation of Coded Communication Schemes using Multidimensional Signal Sets without Constellation Expansion Penalty in Band-Limited Gaussian and Fading Channels" (2014). *University of New Orleans Theses and Dissertations*. 1937.
https://scholarworks.uno.edu/td/1937

Design and Software Validation of Coded Communication Schemes using Multidimensional Signal Sets without Constellation Expansion Penalty in Band-Limited Gaussian and Fading Channels

A Dissertation

Submitted to the Graduate Faculty of the
University of New Orleans
in partial fulfillment of the
requirements for the degree of

Doctor of Philosophy
in
Engineering and Applied Science
Electrical Engineering

by

Milton I Quinteros

B.S., EE, University of New Orleans, 2007
M.S., EE, University of New Orleans, 2009

December, 2014

Dedication

I dedicate my work to the loving memory of my father, Dr. Milton Quinteros Rountree, who I love and miss dearly! God Bless his soul. Additionally, My thesis document is dedicated with deep regard to my beloved mother, Lcda. Mabel Cabrera, who has given me endless emotional support, encouragement and constant love during this process. Mom, I love you so much, thanks for everything!

Acknowledgments

First I would like to thank God, who is the pillar of my strength, and my family, who has helped me unconditionally during my doctoral degree. In addition, I also would like to specially express an enormous gratitude to my major advisor, Dr. Edit J. Kaminsky Bourgeois, for all her continuous support during my graduate studies. Her illuminating guidance, and constructive discussions of my work have contributed greatly to complete my degree. I also want to express my endless thankfulness to Dr. Dimitrios Charalampidis, Dr. George Ioup and Dr. Juliette Ioup for all the support in the Fish Project. Finally, I also would like to thank my friends and co-workers: Dr. Nagendrakumar Beeravolu, Hussain Al Marhoon, Lloyd Carey, and Donald Bradford for all their valuable friendship. In addition, I want to express a meaningful thanks to Mark Allen for all the valuable time encouraging me in good technical writing practices, and his continuous support that allows me to complete my doctoral degree. Finally, I acknowledge my thesis committee members for their constructive and valuable comments.

Table of Contents

List of Figures

List of Tables

Abstract

It has been well reported that the use of multidimensional constellation signals can help to reduce the bit error rate in Additive Gaussian channels by using the hyperspace geometry more efficiently. Similarly, in fading channels, dimensionality provides an inherent signal space diversity (distinct components between two constellations points), so the amplitude degradation of the signal are combated significantly better. Moreover, the set of N-dimensional signals also provides great compatibility with various Trellis Coded modulation schemes: N-dimensional signaling along with a convolutional encoder uses fewer redundant bits for each 2D signaling interval, and increases intra-subset minimum squared Euclidean distance (MSED) to approach the ultimate capacity limit predicted by Shannon's theory. The multidimensional signals perform better for the same complexity than two-dimensional schemes. The inherent constellation expansion penalty factor paid for using classical mapping structures can be decreased by enlarging the constellation's dimension. In this thesis, a multidimensional signal set construction paradigm that completely eliminates the constellation expansion penalty is used in standard AWGN band-limited channels and in fading channels. Theoretical work on performance analysis and computer simulations for Quadrature-Quadrature Phase Shift Keying (Q^2PSK), Constant Envelope (CE) Q^2PSK, and trellis-coded 16D CEQ^2PSK in ideal band-limited channels of various bandwidths is presented along with a novel discussion on visualization techniques for 4D Quadrature-Quadrature Phase Shift Keying (Q^2PSK), Saha's Constant Envelope (CE) Q^2PSK, and Cartwright's CEQ^2PSK in ideal band-limited channels. Furthermore, a metric designed to be used in fading channels, with Hamming Distance (HD) as a primary concern and Euclidean distance (ED) as secondary is also introduced. Simulation results show that the 16D TCM CEQ^2PSK system performs well in channels with AWGN and fading, even with the simplest convolutional encoder tested; achievable coding gains using 16-D CEQ^2PSK Expanded TCM schemes under various conditions are reported.

Index Terms: Q^2PSK, CEQ^2PSK, bandlimited channel, constant envelope, signal trajectory diagram, eye diagram, visualization, fading channel.

Chapter 1 Introduction

Digital communication systems are limited in transmission power and in available spectrum; various modulation schemes have been created to use these resources efficiently. Shannon suggests in [1] that optimal schemes for band-limited Additive White Gaussian Noise (AWGN) channels consist of a dense packing of signal points within a sphere in high-dimensions; as a result, more points can be placed in the n-dimensional space to reduce the effect of Gaussian noise without decreasing minimum distance (average signal energy is not increased) under that of the equivalent lower dimensional set. The increment of transmission efficiency can be accomplished by adding dimensions to a constituent signal space[2–4].

Although the bandwidth-limited AWGN channel is a good starting point to describe basic additive disturbances in a communication system, the next step to model practical environments involves the study of fading effects and how to mitigate fading distortions. As wireless signal travels from the transmitter to the receiver, fluctuations in the received waveform's amplitude and phase may arise due to multiple reflective paths, variations of the density in the propagation medium, and other fading-type distortions that are well documented in [5]. In this scenario, the use of uncorrelated rendition of the signal (signal-space diversity) [3, 5] can help mitigate random amplitude distortion at the receiver end because the uncorrelated received waveform has the tendency to avoid consecutive distortions. Because fading disturbances over different space dimensions can be made statistically independent easily with the use of interleaving techniques and various waveform coding methods [3, 5–9], multidimensional signals offer an attractive means to mitigate amplitude distortions.

The efficient design of communication systems for a fading media which has a variety of constraints is an active research area [6, 10–12], and the adequate implementation of multidimensional constellations aimed at optimality on fading channels has become a current interesting topic in the digital communications field [13–18].

The objective of this dissertation is to further develop the state-of-the-art of multidimensional modulation systems by designing schemes based on a 4-D Quadrature-Quadrature Phase Shift Keying (Q^2PSK) [19] signal constellation. Work by Quinteros, Kaminsky and Cartwright [20–22] where multidimensional constellations based on Q^2PSK were used to help improve the bit error rate performance over uncoded systems is advanced in here. Due to the diversity of models, and uncountable fading parameters, the work presented in this manuscript is limited to specific situations such as explicit cases of bandwidths and fading situations as in [11]. Bandwidth-limited channels are simulated with ideal filters, and fading perturbations are based on modeled channels proposed in [23]. Software implementation using Matlab®Simulink, and methodologies such as Monte Carlo simulations are used to obtain the probability of bit error.

In this introductory chapter, an exposition of the fundamental theory involved in the TCM schemes is reviewed. The following sections briefly survey multidimensionality, expanded constellation 16-D CEQ^2PSK, a brief review of Trellis Coded Modulation (TCM), and software simulation methodologies that shall be used in this dissertation. We end with a description of the papers included as Chapters in this dissertation.

1.1 Multidimensional Constellations

In [1], Shannon develops a methodology to geometrically represent any communication system. It consists of a well-defined algebraic space with dimension $2TW$, where T represents the signal duration and W is the baseband bandwidth. In this way, Shannon defines a capacity based on a coordinate system, and acknowledges that the distortion of a signal can be interpreted as a distortion of the signal's Euclidean space coordinates. Heuristically, more dimensions implies more space to place points farther apart than in equivalent lower dimensions; therefore it is less likely to have a detection errors in each of the components. These ideas have inspired several researchers to explore the hyperspace world to achieve significant noise immunity [3, 20, 22, 24–26].

Forney and Wei [25] define an N-dimensional constellation as a finite set of N tuples, or points in N-dimensional space, where the size of the constellation is the number of its points. For instance, the linear combination of binary orthogonal signals such as sine and cosine can be represented as points in the two-dimensional space.

A simple way to generate a multidimensional constellation is by time concatenation of signals [27]; in other words, multidimensionality can be implemented as sequences of constituent one-, two- or four-dimensional signal intervals [28]. For example, Gersho and Lawrence [4] achieve four dimensions by concatenating two 16 Quadrature Amplitude Modulation (QAM) signals; similarly, Kaminsky [29] achieved eight dimensions by transmitting four consecutive QPSK. In the same fashion, Quinteros et al. [20] also use the time concatenation method to generate 16 dimensional signals.

Another way to generate further dimensions is the use of two data shaping pulses in addition to the two carriers, which are pairwise quadrature in phase, to create a four dimensional signal space [24] which is called Quadrature-Quadrature Phase Shift Keying (Q^2PSK). There are other methods to achieve higher dimensions such as the use of consecutive frequency intervals [30], the use of dual polarization as in Phase/Polarization, Phase/Frequency [31]. A good summary of other methods can be found in[32] and the references therein.

In this manuscript, a four dimensional Q^2PSK symbols are concatenated to yield a 16 dimensional signal. The following subsections aim to give a brief review of the multidimensional constellations used by the author.

1.1.1 4-D Q^2PSK

Quadrature-Quadrature Phase Shift Keying (Q^2PSK) is a four dimensional modulation scheme proposed by Saha in [33]. It uses available signal space dimensions in a more efficient way than two dimensional schemes such as quadrature phase shift keying (QPSK) and minimum shift keying (MSK). The definition of this constellation is covered in the publications of the author (see [34] and references therein) in significantly different ways; therefore, it is not covered in detail in this subsection.

1.1.2 4-D CEQ^{2}PSK

In [24] and [20], respectively, two constant envelope constellations of 8 symbols were introduced: Saha's CEQ^{2}PSK and Cartwright's CEQ^{2}PSK. Constant envelope is obtained at the expense of reducing the transmission rate from 4 bits/sec/Hz to 3 bits/sec/Hz, assuming Nyquist filtering. Each of these two sets of symbols have 8 4-D symbols, both have a minimum squared Euclidean distance (MSED) of 8 for unit energy, and both sets have constant envelope as proven in [20].

Constant envelope is achieved by using a simple rate 3/4 block encoder at the input of the Q^{2}PSK modulator which generates a 4-bit codeword for every 3 information bits, where the fourth bit is an odd parity check bit [33]. The theoretical probability of symbol error for CEQ^{2}PSK in AWGN channels was originally given by Saha in [33], but later corrected in [35].

The use of constant envelope is important [36] for nonlinear channels such as the satellite path with transmitter power amplifiers. A signal with constant envelope allows to easy identify a saturating phenomenon; this idea yields to make the constant envelope an attractive choice to use in the design of the system in this thesis.

1.1.3 Unexpanded 16-D CEQ^{2}PSK

In [20], 16-dimensional constellations were produced by concatenating four consecutive symbols from Saha and Birdsall's constant envelope constellation or four consecutive CEQ^{2}PSK from Cartwright's constellation. Each of these 16-D signal sub sets contains 4096 constant envelope points and retains an MSED of 8 between 16-D points. With all possible combinations of 4 consecutive symbols (from either one or the other constellation, but not both), we have the following two subsets:

$$\begin{aligned} \{S_{16}\} &= [S_i\, S_j\, S_k\, S_l]\,,\ i,j,k,l = 1,2,\cdots,8, \\ \{C_{16}\} &= [C_i\, C_j\, C_k\, C_l]\,,\ i,j,k,l = 1,2,\cdots,8. \end{aligned} \tag{1.1}$$

Table 1.1 shows the squared Euclidean distance (SED) distribution for either of these two 16D sets. Because each 16-dimensional set has 4096 signals, the distribution has a total of $(4096)^2$ distances because we show distances among all possible pairs.

Table 1.1: Squared Euclidean Distance distribution of the 16D CEQ^{2}PSK constellations $\{S_{16}\}$ or $\{C_{16}\}$.

d_k^2	$N(d_k)$
0	4096
8	98304
16	901120
24	3833856
32	7102464
40	3833856
48	901120
56	98304
64	4096

Within each set $\{S_{16}\}$ or $\{C_{16}\}$ the MSED between any pair of different points is still 8, and the peak energy is still equal to 2 per 2D, as they were in the 4D constituent constellations. The error coefficient, $N(d_{min})$, is 24 (i.e., 98304/4096); this means that each of the points has 24 neighbors signals at ED = 8 in 16D.

In Fading channels (to be discussed shortly), it is the Hamming Distance (HD) that is the primary concern. For even values of the Hamming distance, points of Saha's have a certain number of neighbors at that distance while points of Cartwright's points have more neighbors. The HD distribution, then, is not as symmetric as the SED distribution. As an example, Saha's 16D point [1 1 1 -1 1 1 1 -1 1 1 1 -1 1 1 1 -1] has 4097 neighbors at HD 16 (*all* of Cartwright's 16D points and one additional point from Saha's constellation), while Cartwright's points have all of Saha's and also 256 of Cartwright's, for a total of 4097+256=4353. This implies that Saha's points will have a slightly smaller probability of error in Fading channels than Cartwright's.

1.1.4 Expanded 16-D CEQ^{2}PSK

Constellations without expansion penalty can be implemented by using a similar method to that proposed in [31]. The union of two sets of 4096 16-D symbols each, S_{16} for Sahas or C_{16} for Cartwright's, can be formed as follows:

$$V = S_{16} \cup C_{16}. \tag{1.2}$$

V has 8192 points. Notice that the expanded constellation has twice as many points as either unexpanded 16-D CEQ^2 PSK constellation, but still maintains an MSED of 8. Table 1.2 shows the distance distribution of the expanded constellation, with d_k^2 indicating the SED and N(d_k) listing the number of neighbors at that distance. The 24 points (i.e., an error coefficient of 3 when normalized to 2-D) at MSED, as well as the second smallest squared distance of 9.373, with an error coefficient of 16, degrade the performance over the unexpanded constellation. This expanded constellation was used to allow for 1 bit of redundancy per 16-D to be introduced through a convolutional encoder in a TCM system. The improved probability of error performance in [21] is achieved while maintaining constant envelope with a slight increase in the complexity of the decoder. In that paper, we discussed the use of the expanded 8192-point 16-D CEQ^{2}PSK constellation without coding, where the additional bit is used to increase the throughput while slightly deteriorating the probability of error performance. In the following section, the application of the expanded constellation

Table 1.2: The Distance Distribution of Expanded 16-D CEQ^{2}PSK.

d_k^2	N(d_k)	d_k^2	N(d_k)
8.000	24	26.343	896
9.373	16	32.000	2854
15.029	128	37.657	896
16.000	220	40.000	936
20.686	448	43.314	448
24.000	936	48.000	220

is presented with an introductory survey about Trellis Coded Modulation.

1.2 Description of Trellis Coded Modulation

TCM is a joint coding and modulation technique for digital transmission that is especially appropriate for band-limited channels, and has become very popular during recent years because of the gains achieved without compromising bandwidth efficiency [28, 37, 38]. The key idea in TCM schemes is that modulation and coding are combined in order to map the information bits to a modulated constellation signal set. A functional diagram of a standard TCM system is depicted in Figure 1.1

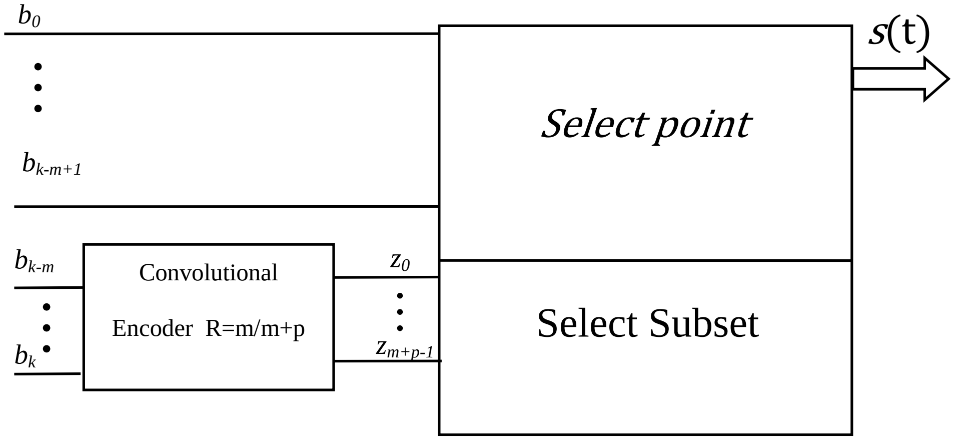

Figure 1.1: General structure of encoder/modulator for TCM

The TCM diagram shows that m bits are encoded to produce $m+p$ coded bits (z$_0$,…,z$_m+p-1$) that select a subset from the partitioned signal constellation. In addition, uncoded bits $(b_0, \ldots, b_{k-m+1})$ select a point within the selected subset, $s(t)$, which is the final signal transmitted. TCM systems require proper set partitioning of the constellation signal set; this task can be accomplished very easily if we have few points and the dimensionality of the signal is small. Ungerboeck [37] proposed certain rules for set partitioning 2-D signals, and Wei expanded this for multidimensional signal sets [39]. Trellis coding uses dense signal sets but restrict the sequences that can be used. This provides a gain in free distance and the code imposes a time dependency on the allowed signal sequences that allows the receiver to ride through noise bursts as it is estimating the transmitted sequence [28].

1.2.1 TCM expansion penalty

TCM schemes require more signal points than uncoded constellations. For example, Ungerboeck [28] went from a 4-PSK uncoded system that transmits 2 bits/sec to an expanded four state Trellis Code 8-PSK modulation. These additional points may be obtained at the cost of either increasing the energy in the system, or reducing the MSED of the constellation. Kaminsky presented in [31] an X8 constellation that can be expanded without increasing the energy of the system and without reducing the MSED of the uncoded constellations.

1.2.2 TCM decoding

Because TCM uses convolutional encoders, the Viterbi Algorithm (VA) is used to search the most likely coded information sequence embedded in a path of the trellis. In [40], TCM decoding is performed in two steps. The first step corresponds to the subset decoding which finds the most likely point in each transition (the closest point in Euclidean distance), and stores the point and the shortest Euclidean distance. The second step of the decoding procedure is to use the previous Euclidean distances to find the most likely path through the trellis by using the VA.

1.3 TCM with Expanded Constellation

Here, we briefly describe the system published in [21]. The transmitter and receiver use 13 coded bits to map onto the 8192 16D symbols. Figure 1.2 shows the block diagram of the transmitter where 13 coded bits are used to transmit 12 information bits $(b_0, , b_{11})$. At the transmitter, an information source generates bits at a fixed bit rate of $1/\mathrm{T}_b$. The output of the convolutional encoder (z_0, z_1, z_2) selects one of the eight subsets (A_k for Saha's constellation or B_k for Cartwright's constellation) obtained in [21]. Two other uncoded bits (b_8, b_9) select one of the W_{ij} or W_{ijr} Types from within the selected group. The rest of the information bits (b_0 through b_7) select one of the 256 points from within the selected 16-D

W_{ij} or W_{ijr} Types. The selected signal s(t) is transmitted. The generated waveforms are transmitted through the channel, assumed here to be AWGN with two-sided power spectral density $N_o/2$ in each component.

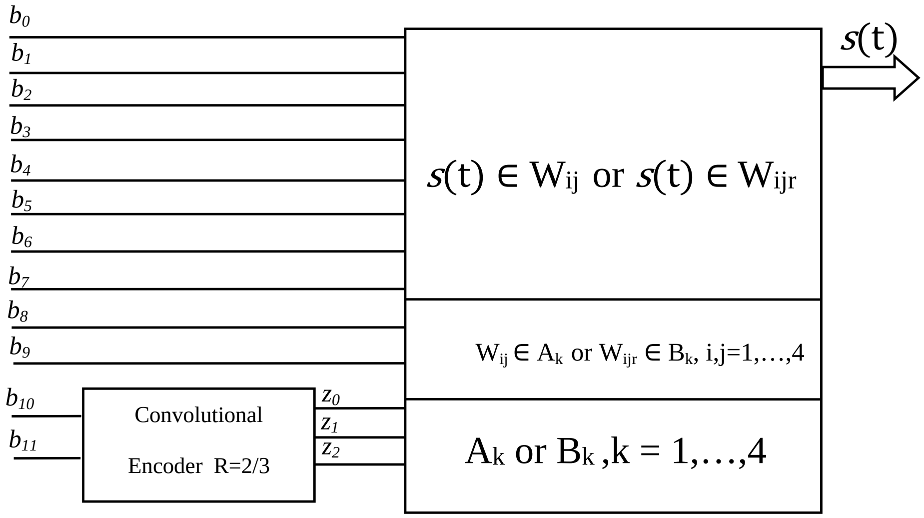

Figure 1.2: Block diagram of the encoder/modulator for 16-DCEQ^{2}PSK-TCM system

At the receiver, the noisy analog signals are correlated, every 2T, with the Q^{2}PSK basis vectors, with the use of multipliers followed by integrate-and-dump subsystems. Four consecutive signals are then concatenated with the aid of a buffer to generate a 16-D vector with real components which is the input of a soft decision Viterbi Decoder. The implementation of the decoder will be explained in Chapter 10.

1.4 Simulations

Software simulations complement the theoretical work. The author simulates particular implementations of the theoretical developments with different parameters and in various channels. We use Matlab[1]® and its Simulink toolbox for all our Monte Carlo simulations. The use of Simulink blocks helps reduce the burden of myriad long lines of code; furthermore, various channel scenarios are easily implemented using pre-defined channels with selectable parameters. The most important measure of performance of Communication Systems is the probability of error. In order to compute the error performance of the proposed sys-

---

[1] Matlab and Simulink are copyrighted trademark names from The Mathworks.

tems, Monte Carlo simulations are performed. In AWGN channels, for each SNR value, the simulation runs until twenty symbol errors are counted [41].

1.5 Description of submitted papers and funded project

Chapter 3 is an article published in the IEEEE GLOBECOM 2014 conference [34], where the authors present theoretical analysis and simulation results for Q^2PSK, CEQ^2PSK [33] and expanded 16D CEQ^2PSK [21] systems in ideal bandlimited channels. The authors' results show that 6.8 dB of SNR is needed for expanded 16D CEQ^2PSK system for a bit error rate of 10^{-5} in a bandwidth of $0.6/T$. In addition, a spectral analysis for 16D-CEQ^2PSK constellation [20] is introduced in this publication.

Chapter 4 is a manuscript submitted to the IEEE Wireless Communication and Networking Conference (WCNC) 2015 that presents three visual performance indicators for multidimensional signals. The diagrams use are: first, time-signal eye patterns for 4D passband representation; second, 2-D complex trajectory diagrams for 4D baseband representation; third, signal-time eye patterns at the matched filter receiver output.

Chapter 6 presents a modulation system that uses an expanded 16-Dimensional Constant Envelope Quadrature-Quadrature Phase Shift Keying (CEQ^2PSK) constellation to increase the transmission information rate of unexpanded 16-D CEQ^2PSK by one bit per 16-D, for a bandwidth efficiency of 3.25 bits/dimension [2]. The improvement in information transmission rate is achieved with similar energy requirements and the same constant envelope properties as for the unexpanded constellation. The increase in spectral efficiency over the unexpanded system is confirmed through computer simulations.

Finally, Chapters 7, 8, and 9 correspond to work performed for a project entitled *16-Dimensional Trellis Encoded CEQ^2PSK for non-linear mobile communication channels*, under Task Order 17 of contract N69250-08-D-0302 between SPAWAR and UNO. These chapters present the work performed over nine months by the UNO PI Dr. Edit J. Kaminsky

---

[2] Paper accepted and then withdraw by the authors.

Bourgeiois and her graduate assistant Milton Quinteros on design and development of a Simulink©-based system that implements a complete trellis encoded communication system using our 16-dimensional (16D) expanded CEQ^{2}PSK constellation. The system consists of the transmitter, the channel, and the receiver. The transmitter generates the random message, encodes and modulates it using Trellis Coded Modulation (TCM) 16D CEQ^{2}PSK, and sends the encoded and modulated message through the channel. The channel simulated fading Rician/Rayleigh and Additive White Gaussian Noise(AWGN).

Chapter 2 Communication Channel Models

This chapter briefly discusses the Additive White Gaussian Noise (AWGN) standard channel model, the Rayleigh Fading Channels, and the Rician Fading Channels. The author surveys the UHF channels originally described in [11] for which simulations with many parameter sets were run. These parameters are sampling rate, Doppler frequency, Rayleigh spectral characteristics, etc.).

2.1 AWGN channel

The Gaussian channel model is used to study the performance and limits of the various digital modulation systems. It is well known that Gaussian perturbation is present in all practical telecommunications systems, so the importance of increasing the noise immunity for this channel is paramount. The channel adds White Gaussian noise, AWGN, to the transmitted analog signals. The AWGN is characterized completely by its mean, which is zero, and its variance, which determines the SNR. The received signal therefore has the form

$$r(t) = h(t) * s(t) + n(t) \tag{2.1}$$

where $*$ denotes convolution, $h(t)$ is the channel impulse response, $s(t)$ is the sent signal, and $n(t)$ is the AWGN with one-sided power spectral density $\mathrm{N}_o/2$ W/Hz. The probability density function for $n(t)$ is Gaussian with zero-mean and variance σ^2 is:

$$f_x(x) = \frac{1}{\sqrt{2\pi}\sigma} \exp\left\{-\left(\frac{x}{\sigma}\right)^2\right\}. \tag{2.2}$$

The power of the noise (σ^2) is the determining factor in the quality of reception: the probability of error or bit error rate, BER.

Maximization of the MSED (i.e., the minimum possible Squared ED) is the design criterion for TCM systems in AWGN.

In chapter 3, the authors utilize an ideal filter for $h(t)$ that has flat frequency response over a particular one-sided frequency band B.

2.2 Fading Channels

Cellular land mobile channels are usually modeled as Rayleigh channels while land mobile satellite channels exhibit a direct line-of-sight (LOS) component as well as multipath components [42]. We discuss these in the next few Sub Sections.

Fading is a time-varying behavior in the received signal envelope, caused by multipath reflections. The envelope is affected (multiplied by) a Rayleigh or Rician process.

For fading channels with trellis coded modulation, the principal design criterion is to maximize the minimum Hamming distance of the trellis code. Secondary to this criterion, is the product Euclidean distance (the product of the SED between sequences that diverge and then converge) [43].

Remember, however, that our 16D CEQ^{2}PSK constellation points have components that may be 0, ± 1, and $\pm\sqrt{2}$. HD, then, should be slightly re-defined (because we no longer deal with just 0 or 1 or -1 and 1). We are using the term Hamming Distance (HD) for the *number of coordinates that differ*, regardless of how much they differ by. We then weigh this HD by the ED to obtain what we call a "Weighted Distance", WD.

To clarify this, let us consider a couple of pairs of possible points in an example: [1 1 1 1] and [-1 -1 -1 -1] have a (true) HD of 4, the same as the HD between [1 1 1 1] and [0 $\sqrt{2}$ 0 $\sqrt{2}$], because all coordinates differ. However, the weighted distance betwen the two former points is larger than between the latter 2. These examples are shown in Table 2.1, where we list the example 4D points, the HD, the SED, and the resulting WD obtained by using

$$WD = 4 \cdot \frac{HD \cdot SED}{64} \tag{2.3}$$

because we are using 4 dimensions, and the maximum (normalizing) SED is 16.

Table 2.1: Example of Distances

P_1				P_2				HD	SED	WD
1	1	1	1	-1	-1	-1	-1	4	16	4
1	1	1	1	0	$\sqrt{2}$	0	$\sqrt{2}$	4	2.34	0.584
1	1	1	1	0	$-\sqrt{2}$	0	$-\sqrt{2}$	4	13.66	3.416

2.2.1 Rayleigh Fading Channel

In a simple Rayleigh fading channel, the transmitted signal's envelope is multiplied by a random process with a Rayleigh distribution. The phase disturbance is ignored (or assumed known or estimated well). This multiplicative noise is caused by multipath. The parameter that determines the characteristics of the Rayleigh distribution is b. The mean of the Rayleigh pdf is $b\sqrt{\pi/2}$ and its variance is $(2-\pi/2)b^2$. AWGN is also included in this model, to obtain a received signal as in (2.4):

$$r(t) = d(t)s(t) + n(t), \tag{2.4}$$

where $d(t)$ is the multiplicative noise, whose amplitude has a Rayleigh pdf given by (2.5):

$$f_d(d) = \frac{d}{b^2} e^{\left(\frac{-x^2}{2b^2}\right)}, \tag{2.5}$$

where the Rayleigh pdf of the amplitude of d has parameter b.

Often, multipath is parameterized by the maximum Doppler frquency, f_d, instead of the Rayleigh parameter b. If $1/f_d$ is large with respect to the symbol duration, we have slow fading (i.e., a fading event affects many symbols). If f_d is large so that a single symbol or a part thereof are affected by a fading event, then the result is fast fading. Most of our simulations, but not all, were done in slow fading channels.

2.2.2 Rician Fading Channels

In Rician fading, there is a strong dominant component present and the mean value of (at least) one component will be non-zero. The PDF of the signal amplitude, ρ is given by

$$f_\rho(\rho) = \frac{\rho}{\sigma^2} exp\left(\frac{\rho^2 + c_a^2}{2\sigma^2}\right) I_0\left(\frac{c_a\rho}{\sigma^2}\right) \tag{2.6}$$

where I_0 is the Bessel function of the first kind and zero order, σ^2 is the local mean scattered power, and $c_a^2/2$ is the power of the dominant component.

Rician processes may be characterized by the Rician K-factor, K, the ratio of signal power in the dominant component over the scattered power:

$$K = \frac{c_a^2}{2\sigma^2} \tag{2.7}$$

The total local-mean power is the sum of the power in the line-of-sight (LOS) and the power of the scattered components:

$$\bar{p} = \frac{1}{2}c_a^2 + \sigma^2 \tag{2.8}$$

The local-mean scattered power is

$$s^2 = \frac{\bar{p}}{K + 1} \tag{2.9}$$

Moose, Roderick and North [11] detail three channels: the UHF LOS Channel #1 with one Rician and one Rayleigh path, the UHF LOS Channel #2 with one Rician and two Rayleigh paths, and the UHF LOS channel #3, again with one Rician and two Rayleigh paths. The propagation loss in each case is 135 dB. The relative time delays, T_{i-j}, the relative losses, L_{i-j}, and maximum Doppler or fade rates, f_d are given below.

- UHF LOS Channel #1
  - Path 1: Rician, $f_d = 1$ Hz,

  - Path 2: Rayleigh, $\mathrm{T}_{1-2} = 0.01\mu s$, $\mathrm{f}_d = 10$ Hz, $\mathrm{L}_{1-2} = -6$ dB.

- UHF LOS Channel #2
  - Path 1: Rician, $\mathrm{f}_d = 10$ Hz,
  - Path 2: Rayleigh, $\mathrm{T}_{1-2} = 0.07\mu s$, $\mathrm{f}_d = 10$ Hz, $\mathrm{L}_{1-2} = -5$ dB,
  - Path 3: Rayleigh, $\mathrm{T}_{1-3} = 0.8\mu s$, $\mathrm{f}_d = 10$ Hz, $\mathrm{L}_{1-3} = -15$ dB.

- UHF LOS Channel #3
  - Path 1: Rician, $\mathrm{f}_d = 25$ Hz,
  - Path 2: Rayleigh, $\mathrm{T}_{1-2} = 0.9\mu s$, $\mathrm{f}_d = 25$ Hz, $\mathrm{L}_{1-2} = -3$ dB,
  - Path 3: Rayleigh, $\mathrm{T}_{1-3} = 5.1\mu s$, $\mathrm{f}_d = 25$ Hz, $\mathrm{L}_{1-3} = -9$ dB.

In this dissertation, the UHF LOS Channel #1 discussed in [11] is implemented in software.

Chapter 3 Performance and Spectral Analysis of Q^{2}PSK and CEQ^{2}PSK Systems in Ideal Bandlimited Channels

3.1 Introduction

The search for appropriate classes of signals and methods to mitigate medium disturbances has driven much of communications research. Researchers have investigated the performance of different sets of signals on a variety of channels which are limited in transmission power and available spectrum. In classical uncoded modulation systems, an increase in transmission efficiency might be accomplished by increasing the dimensionality of the signal space (see [2] and references therein).

Over the last few decades, authors have shown interest in a four-dimensional (4D) modulation scheme proposed by Saha and Birdsall in [33]: Quadrature-Quadrature Phase Shift Keying (Q^{2}PSK). Because Q^{2}PSK uses the space more efficiently than conventional QPSK and Minimum Shift Keying (MSK), Q^{2}PSK provides increased spectral efficiency [27, 44–46]. Indeed, Q^{2}PSK and its variants have been considered by several authors because of the attractive possibility of spectral and power efficiency [21, 27, 35, 45–54].

Q^{2}PSK is reported to achieve 4 bits per modulation interval but lacks constant envelope which is a desired feature for nonlinear channels such as the satellite path [52]. If parity check coding is imposed at the input of the Q^{2}PSK modulator, 4D Constant Envelope Quadrature-Quadrature Phase Shift keying (CEQ^{2}PSK) is obtained [33],[44],[20] at the cost of a reduction in the information rate to 3 bits per modulation interval.

Westra et al. reported multilevel forms of Q^{2}PSK in [47] to increase the effective data throughput. Saha and El-Ghandour introduced differential phase Q^{2}PSK in [48], and Korn and Wei analyzed the performance on mobile satellite channels in [50]. Offset Q^{2}PSK, which attains lower peak to average power ratio than Q^{2}PSK, was presented in [53]. In [20], two 16D constellations that use four consecutive signalling intervals of CEQ^{2}PSK were introduced:

an unexpanded 16D CEQ^{2}PSK constellation of 4096 signal points and an expanded 16D CEQ^{2}PSK constellation of 8192 points. The unexpanded constellation has an information rate of 12 bits per 16D interval while the expanded constellation may be used to transmit 13 bits per 16D interval or to incorporate error correction coding [21].

Various implementations of Q^{2}PSK combined with bandwidth efficient coding techniques such as Multidimensional Trellis Coded Modulation (MTCM) [39] have been presented [52],[19]. In contrast to the conventional MTCM implementations, Quinteros et al. [21] used a technique proposed by Kaminsky in [31],[22] to obtain a 16D TCM CEQ^{2}PSK system that suffers no loss due to constellation expansion. Most recently, [54] used the same technique with a 32D CEQ^{2}PSK constellation.

In this paper, we further analyze the performance of 4D Q^{2}PSK in [44] and also present analysis for 4D CEQ^{2}PSK and a trellis encoded 16D CEQ^{2}PSK system in the bandlimited additive white Gaussian noise (AWGN) channel. In particular, we assume ideal filters of baseband bandwidth $\frac{0.6}{T}$ and $\frac{1}{T}$, where $2T$ is the 4D symbol interval (i.e., the bit interval, T_b is $T/2$) with perfect knowledge of the phase. In our simulations, we implement a receiver that assumes knowledge of the channel and one that doesn't (i.e., the receiver uses reference pulses which are not bandlimited). A discrete implementation of a finite-length maximum likelihood detector is employed in all cases; this is equivalent to the hardware detector in [35], optimum when no Inter-Symbol Interference (ISI) and no Cross-ISI (CISI) are present. In addition, we briefly present spectral analysis of all these systems.

We show that for very narrow channels the use of channel estimation aids the 16D TCM system more than the others and that knowledge of the channel is more important for Q^{2}PSK than for its 4D constant envelope counterpart at all bandwidths. Losses due to finite channel bandwidth are most severe for Q^{2}PSK. At the narrowest bandwidth considered here, $0.6/T$, the gain of the 16D TCM system is 2 dB at a probability of bit error of 10^{-5}. Furthermore, we show that the performance of Saha's bit-by-bit suboptimum detector [44] may be considerably improved upon with little increase in complexity.

The rest of this paper is organized as follows: In Section 3.2, brief descriptions of Q^{2}PSK, CEQ^{2}PSK, and 16D CEQ^{2}PSK are presented. In Section 3.3 we describe the channel model, followed in Section 3.4 by discussion of the receiver and the signals therein. Analysis of the probability of error in bandlimited channels with finite ISI and CISI is given in Section 3.5, along with presentation of the spectral analysis. Results are given in Section 3.6. Conclusions and suggestions for further work are given in Section 3.7, followed by cited references.

3.2 Brief Review of Q^{2}PSK

In this section, we briefly discuss the following constellations: 4D Q^{2}PSK [33], Saha's 4D CEQ^{2}PSK [44], Cartwright's 4D CEQ^{2}PSK [20], and both unexpanded and expanded 16D CEQ^{2}PSK [21].

3.2.1 4D Q^{2}PSK

The 4D Q^{2}PSK modulation technique was introduced in [33] and uses the following transmitted signal:

$$S_q(t) = \sum_{i=1}^{4} b_i(t) s_i(t), \tag{3.1}$$

where $b_i(t)$, $i = 1, \ldots, 4$, is the value of the original bit i of duration $T/2$ prior to the the serial to parallel conversion and of duration $2T$ after [33], and the passband modulating signal set $\{s_i(t)\}$, $i = 1, \ldots, 4$, is:

$$s_1(t) = p_1(t)\cos(2\pi f_c t), \quad |t| \leq T \tag{3.2a}$$

$$s_2(t) = p_2(t)\cos(2\pi f_c t), \quad |t| \leq T \tag{3.2b}$$

$$s_3(t) = p_1(t)\sin(2\pi f_c t), \quad |t| \leq T \tag{3.2c}$$

$$s_4(t) = p_2(t)\sin(2\pi f_c t), \quad |t| \leq T, \tag{3.2d}$$

with orthogonal half-sinusoidal pulses $p_1(t) = \cos(\pi t/2T)$ and $p_2(t) = \sin(\pi t/2T)$, for $|t| \leq T$, and 0 otherwise. The carrier frequency, f_c, should be $\frac{\mathrm{n}}{4T}$ with $\mathrm{n} \geq 2$, and T is the duration of 2 bits. There are 16 symbols that form this non-constant envelope signal set with efficiency of 4 bits per modulation interval.

Using the baseband equivalent model for (3.1), the k^{th} transmitted Q^{2}PSK signal is represented as:

$$\begin{aligned} S_k(t) = {} & b_{1,k}p_1(t-2kT) + b_{2,k}p_2(t-2kT) + \\ & -j[b_{3,k}p_1(t-2kT) + b_{4,k}p_2(t-2kT)]. \end{aligned} \tag{3.3}$$

3.2.2 4D CEQ^{2}PSK

In [33] and [20], two constant envelope 4D constellations were introduced, each with an MSED of 8 for unit energy: Saha's CEQ^{2}PSK and Cartwright's CEQ^{2}PSK, respectively. Constant envelope is obtained by using a rate-3/4 block encoder at the input of the Q^{2}PSK modulator, where the fourth output bit is an odd parity check bit [33]. Three information input bits $\{b_1, b_2, b_3\}$ generate code words $\{b_1, b_2, b_3, b_4\}$ such that the eight possible transmitted signals for Saha's CEQ^{2}PSK are $S_1 = [a, a, b, -b]$ and $S_2 = [a, -a, b, b]$. For Cartwright's CEQ^{2}PSK, we have $S_{1r} = [0, \sqrt{2}a, \sqrt{2}b, 0]$ and $S_{2r} = [\sqrt{2}a, 0, 0, \sqrt{2}b]$. In both cases, a, b are either ± 1. In order for the envelope to be constant, $b_1b_2 + b_3b_4 = 0$.

3.2.3 16D CEQ^{2}PSK

Unexpanded 16D CEQ^{2}PSK

In [20], two 16D constellations were produced by concatenating either four consecutive CEQ^{2}PSK symbols from Saha's constellation or four consecutive CEQ^{2}PSK from Cartwright's constellation. Each of these 16D signal sets contains 4096 constant envelope points and has an MSED of 8 for unit energy.

Expanded 16D CEQ^{2}PSK

The expanded 16D CEQ^{2}PSK constellation is the union of the two 16D CEQ^{2}PSK in subsection 1) above, and has 8192 points; the expanded constellation has twice as many points as either unexpanded 16D CEQ^{2}PSK constellation but still maintains an MSED of 8. There are 16 points (i.e., an error coefficient of 2 when normalized to 2D) at the second smallest squared distance of 9.373 which slightly degrades the performance over the unexpanded constellation, particularly for low SNR [20]. In [21], this expanded constellation was used to allow 1 bit of redundancy per 16D to be introduced through a convolutional encoder in a TCM system. This 16D TCM CEQ^{2}PSK system is also studied here. Improved probability of error performance is achieved while maintaining constant envelope with a slight increase in system complexity.

3.3 Channel Model

Most transmission media alter the transmitted signals in some way, especially when the channel has limited bandwidth [55]. In this section, we define the simple ideal bandlimited additive white Gaussian noise (AWGN) channel we use in our analysis and simulations, and show the effects of bandlimiting on Q^{2}PSK and CEQ^{2}PSK.

Forney and Ungerboeck defined the ideal bandlimited channel with flat frequency response within baseband bandwidth B in [2]. The signal $s(t)$ passes through a dispersive channel with impulse response $h(t)$ and zero-mean AWGN $n(t)$. The received signal is:

$$r(t) = s(t) * h(t) + n(t), \tag{3.4}$$

with $h(t)$ given by:

$$h(t) = \frac{\sin(2\pi Bt)}{\pi t}. \tag{3.5}$$

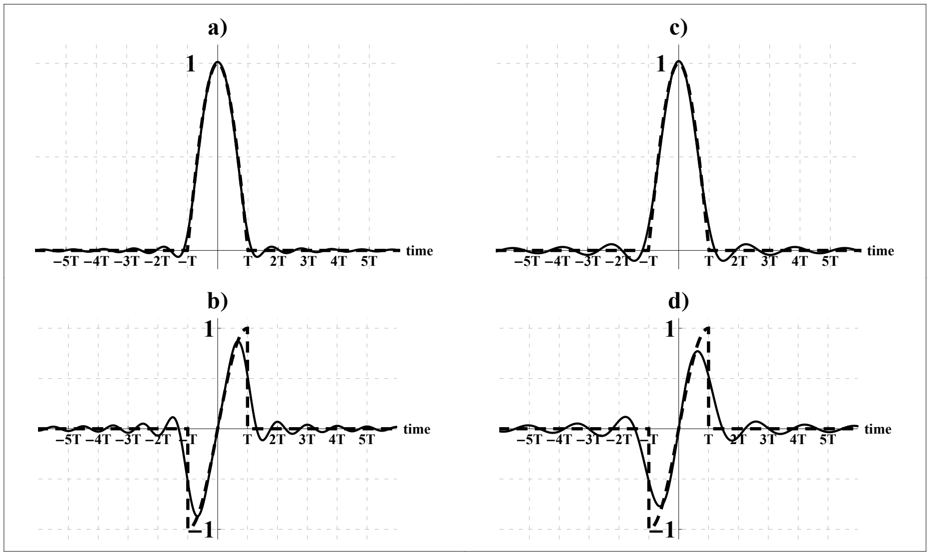

Figure 3.1: Filtered (continuous line) and unfiltered (dashed line) cosine and sine pulses. a) p_1 and $p_{1f}(t)$, B_1. b) p_2 and $p_{2f}(t)$, B_1. c) p_1 and $p_{1f}(t)$, B_2. d) p_2 and $p_{2f}(t)$, B_2 (with $B_1 = 1/T$, $B_2 = 0.6/T$).

We consider two channel bandwidths, defined in baseband (one-sided) as: $B_1 = \frac{1}{T}$ and $B_2 = \frac{0.6}{T}$, where $2T$ is the 4D signal interval. When the pulses $p_1(t)$ and $p_2(t)$ of (2) pass through the channel in (3.4, 3.5), they suffer from the combined effects of intersymbol interference (ISI), cross intersymbol interference (CISI) [46], and noise. If $p_{i,k}$ denotes pulse p_i at time $2kT$, i.e., $p_i(t-2kT)$, ISI is caused by $p_{i,j}$ interfering with $p_{i,k}$, $j \neq k$ and $i = 1, 2$, and CISI is caused by $p_{1,j}$ interfering with $p_{2,k}$ or $p_{2,j}$ interfering with $p_{1,k}$, for any j, k. The effects of filtering are shown in Fig. 3.1 for two bandwidths of interest, where the filtered pulses are denoted with the subscript f, and are given by (A.23) and (A.24) in the Appendix A.

In our performance analysis, we assume that only one past and one future symbol interfere with the current symbol being detected. A total of 83 % of the energy in the half-sine pulse and 99 % of the half-cosine pulse are within a bandwidth of $0.6/T$; of this energy, 99 % and 99.8 %, respectively, is within the interval from $-3T$ and $3T$ (i.e., from $k = -1$ to 1).

3.4 Coherent Receiver

At the receiver, the passband received signal is coherently detected in the correlation receiver by multiplying it by the cosine and sine carriers and by the half-cosine and half-sine pulses and then integrating and dumping. In baseband, the receiver ideally separates the real parts from the imaginary parts, and the cosine pulses from the sine pulses by multiplying the filtered signal $s_f(t) = \mathrm{Re}\{s_f(t)\} + j\,\mathrm{Im}\{s_f(t)\}$ by the original pulses $p_1(t) - jp_2(t)$ if no knowledge of the channel is available, or by the filtered pulses $p_{1f}(t) - jp_{2f}(t)$ if the channel is known. Due to ISI and CISI, the tails of the interfering past and future pulses affect the pulses currently being detected. Considering only the truncated sequence [56] of length equal to three signaling intervals ($k = -1, 0, 1$) and ignoring the noise for now, the signals at the input of the receiver, corresponding to the current signaling interval being detected ($|t| \leq T$) are:

$$\begin{aligned} s_f(t) = \sum_{k=-1}^{1} &\left[b_{1,k}p_{1f}(t-2kT) + b_{2,k}p_{2f}(t-2kT) + \right. \\ &\left. + j\left(b_{3,k}p_{1f}(t-2kT) - b_{4,k}p_{2f}(t-2kT)\right)\right], \end{aligned} \tag{3.6}$$

where p_{1f} and p_{2f} are the filtered pulses shown in Fig. 3.1 and defined in (A.23, A.24) in the Appendix, and $b_{i,k}$, $i = 1, \ldots, 4$ represents bit i at time $(t - 2kT)$; for example, $b_{2,-1}$ is the value of the second component of the 4D vector $[b_1(t+2T)\ b_2(t+2T)\ b_3(t+2T)\ b_4(t+2T)]$, i.e., the coefficient of the sine pulse p_2 on the cosine carrier, from the previous 4D signaling interval (the immediate past symbol).

We wish to show the output of the correlation receiver. To concisely write the expression for these output values, we use the following notation: Let $P_{i,j}(r,s) = \int_{-T}^{T} p_i(t-r)p_j(t-s)dt$. We also let $j = 2 - i \bmod 2$, $l = i - (-1)^i$, and $i = 1, \ldots, 4$. The coefficients at the output of the receiver, including (finite) ISI and the CISI are given by (3.7):

Table 3.1: Magnitude of the Coefficients in (3.7) for two channel bandwidths for Q^{2}PSK and Saha's CEQ^{2}PSK.

$B_1 = \frac{1}{T}$		$B_2 = \frac{0.6}{T}$			
$\hat{c}_1$ or $\hat{c}_3$	$\hat{c}_2$ or $\hat{c}_4$	$\hat{c}_1$ or $\hat{c}_3$	$\hat{c}_2$ or $\hat{c}_4$	N_1	N_2
0.989543	0.778107	0.975659	0.687676	128	16
0.992196	0.783469	0.979426	0.699171	256	32
0.994848	0.788830	0.983194	0.710665	128	16
0.994905	0.887331	0.987154	0.820393	256	32
0.997557	0.892692	0.990921	0.831888	512	64
1.000209	0.898053	0.994688	0.843383	256	32
1.000266	0.996554	0.998648	0.953111	128	16
1.002918	1.001915	1.002416	0.964605	256	32
1.005571	1.007276	1.006183	0.976100	128	16

$$\begin{aligned}\hat{c}_i = {} & b_{i,-1}P_{j,j}(0,-2T) + b_{i,0}P_{j,j}(0,0) + \\ & + b_{i,1}P_{j,j}(0,2T) + b_{l,-1}P_{j,3-j}(0,-2T) + \\ & + b_{l,1}P_{j,3-j}(0,2T).\end{aligned} \tag{3.7}$$

Given a single past, present, and future symbol, we can easily enumerate the resulting coefficients, which are ±1 for the unfiltered channel. For the receiver without channel information, these are shown in Table 3.1 for the two channel bandwidths we use; the negative value for each is also possible. The numbers listed under the last two columns, N_1 and N_2, indicate the number of occurrences of each for Q^{2}PSK and Saha's CEQ^{2}PSK, respectively; there are a total of 4096 sequences of length 3 in the former, and 512 in the latter.

3.5 Performance Analysis

We describe performance of the Q^{2}PSK systems based on probability of error versus SNR and spectral efficiency. We discuss each separately.

Table 3.2: Parameters of (3.8,3.9) for the Q^2PSK systems of interest.

	4D Q^2PSK	4D CEQ^2PSK	unexpanded 16D CEQ^2PSK	expanded 16D CEQ^2PSK
d_0^2	4	8	8	8
d_{min}^2	4	4	4	4
R	1	3/4	3/4	13/16
R_b	1	1	1	1
γ_c	1	3/2	3/2	13/8
K_d	2	3	3	3

3.5.1 Probability of Bit Error

We quickly derive the probability of error for the Q^2PSK systems in this section. We assume AWGN with (one sided) PSD N_0 in each component. If no bandlimiting occurs, such that there is no ISI/CISI, the probability of bit error may be written as [2]:

$$\mathrm{P}_{be} = \mathrm{K}_d \mathrm{Q}\left(\sqrt{\gamma_c \frac{2\mathrm{E}_b}{\mathrm{N}_o}}\right), \tag{3.8}$$

where K_d is the error coefficient normalized per two dimensions, and γ_c is the coding gain given by (3.9):

$$\gamma_c = \frac{d_o^2}{d_{\mathrm{min}}^2}\frac{\mathrm{R}}{\mathrm{R_b}}, \tag{3.9}$$

where d_0 and d_{min} are the minimum distances between points in the coded and uncoded constellations, respectively; R_b is the rate in information bits per dimension of the uncoded system and R is the rate of the coded system, again in information bits per dimension [2]. The values of these are shown in Table 3.2 for the four systems we discuss here.

A bit error is committed when the interference and noise cause the transmitted bit to cross the zero-threshold. The probability of bit error, P_{be}, for filtered (finite length) Q^2PSK and

CEQ^{2}PSK is given by (3.10):

$$\begin{aligned}\mathrm{P}_{be} &= \sum_{n=1}^{9} P(r < 0\,|\hat{c}_i)P(\hat{c}_i) = \sum_{n=1}^{9} P(n < -\hat{c}_i)P(\hat{c}_i) \\ &= \sum_{n=1}^{9} P(\hat{c}_i)\mathrm{Q}\left(\frac{\hat{c}_i}{\sigma}\right) = \sum_{n=1}^{9} P(\hat{c}_i)\mathrm{Q}\left(\sqrt{\frac{2}{N_0}}\hat{c}_i\right),\end{aligned} \tag{3.10}$$

where r is the appropriate component of the received signal, the coefficients are those listed in Table 3.1, and $P(\hat{c}_i)$ is $\mathrm{N}_1/2048$ for Q^{2}PSK and $\mathrm{N}_2/256$ for CE Q^{2}PSK. Notice that the probability of error is higher for the second and fourth components of the 4D vector than for the first and third; this is due to the significantly wider bandwidth of the half-sine pulse, $p_2(t)$, compared to the half-cosine pulse $p_1(t)$. Equations (3.8, 3.10) assume the received components are independent; this is never true for the fourth bit of CEQ^{2}PSK, and is not strictly true for any of these systems due to ISI and CISI. Nonetheless, we show in Section 3.6 that (3.10) is accurate for all SNR of interest.

We define the SNR in dB as $10\log_{10}\left(\frac{\mathrm{E}_b}{2\sigma^2}\right)$, where E_b is the energy per bit and σ^2 is the noise power in each component, so that SNR=$\mathrm{E}_b/\mathrm{N}_0$. We use unity bit energy here.

3.5.2 Spectral Performance

Van Wyk presented an expression for the baseband power spectral density (PSD) of coded and uncoded Q^{2}PSK in [57]. If the amplitudes of the waveforms are adjusted to unity, and using the symbol period $T_s = 4T_b = 2T$, Van Wyk's expression for Q^{2}PSK becomes:

$$\frac{S_{Q^2}(f)}{T_s^2} = \frac{4\left(1+64f^2T_b^2\right)}{\pi^2}\left(\frac{\cos\left(4\pi fT_b\right)}{1-64f^2T_b^2}\right)^2. \tag{3.11}$$

For CEQ^{2}PSK, due to the introduction of the parity check bit, $T_s = 3T_b = 2T$, where the the subscript b now indicates information bit; hence,

$$\frac{S_{CEQ^2}(f)}{T_s^2} = \frac{4\left(1+36f^2T_b^2\right)}{\pi^2}\left(\frac{\cos\left(3\pi fT_b\right)}{1-36f^2T_b^2}\right)^2, \tag{3.12}$$

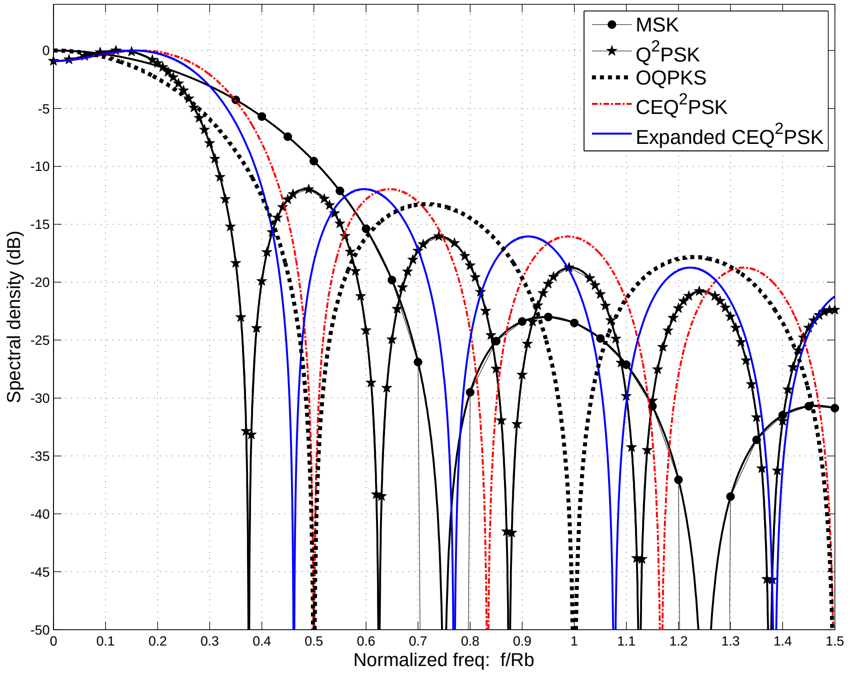

Figure 3.2: PSD for systems of interest.

which applies to both Saha's and Cartwright's CEQ^{2}PSK constellations.

Finally, for expanded CEQ^{2}PSK we have a 4D symbol period of $T_s = \frac{13T_b}{4} = 2T$ and (3.12) becomes

$$\frac{S_{\exp}(f)}{T_s^2}=\frac{4+169f^2T_b^2}{\pi^2}\left(\frac{\cos\left(13\pi f T_b/4\right)}{1-169f^2T_b^2/4}\right)^2 . \tag{3.13}$$

Fig. 3.2 shows the PSD for the systems of interest, in addition to MSK and OQPSK. Non-parametrical spectral estimation was performed using the periodogram method, with 200 spectral averages and using Bartlett windows before performing the FFT. Simulation results confirmed the derivation above (the plots of the simulated values are not shown as they overlap the theoretical lines).

We note that the -3 dB bandwidth of expanded 16D CEQ^{2}PSK is equal to that of MSK, and is 125 % of Q^{2}PSK's. CEQ^{2}PSK has the widest -3 dB bandwidth, and its PSD is similar to that of Offset QPSK [33], in the sense that the first null also occurs at normalized frequency of 0.5. The first null of the expanded constellation is $\frac{6}{13T_b} = \frac{0.4615}{T_b}$, 61 % of that of MSK, while it is 67 % for CEQ^{2}PSK and 50 % for Q^{2}PSK.

Q^{2}PSK has the narrowest main lobe, but the first side lobe has the same peak energy as those of both CEQ^{2}PSK systems. MSK's main lobe is the widest, with considerably lower and wider sidelobes. The sidelobe peaks derease most slowly for CEQ^{2}PSK (expanded and unexpanded).

3.6 Results

We present simulation results for 4D Q^{2}PSK, Saha's 4D CEQ^{2}PSK, and 16D TCM CEQ^{2}PSK for ideal bandlimited channels of baseband bandwidth $1/T$ and $0.6/T$, along with theoretical performance curves, when available. Unfilled markers show simulations results obtained counting at least 20 bit errors.

Fig. 3.3 shows a comparison of the bit error rates (BER) for filtered and unfiltered Q^{2}PSK, 4D CEQ^{2}PSK, and 16D TCM CEQ^{2}PSK at the two bandwidths of interest using no channel estimation. We see in Fig. 3.3 that the TCM system provides about 2 dB of gain over the equivalent uncoded system for all channel bandwidths, requiring only 7.3 dB in SNR for a probability of bit error of 10^{-5} when bandlimited to $0.6/T$ baseband bandwidth. We also confirm that Q^{2}PSK requires about 11.2 dB of SNR for a bit error rate (BER) of 10^{-5}, as stated by Saha in [44], for a filter of bandwidth $0.6/T$; we note, however, that Saha used a sixth-order Butterworth filter. Losses due to finite channel bandwidth are most severe for Q^{2}PSK.

Figs. 3.4 and 3.5 allow us to compare the receivers with channel knowledge (receiver 2) to those that do not assume any knowledge of the channel (receiver 1). Fig. 3.4 shows our results for a channel bandlimited to $0.6/T$ while Fig. 3.5 shows the same curves for a channel of bandwidth $1/T$. The gains achieved by using channel estimation are clearly shown on the plots.

Saha stated in [33] that MSK needs 9.6 dB of SNR to achieve $P_{be} = 10^{-5}$ when filtered at $0.6/T$ and, in [44], that CEQ^{2}PSK requires 10.3 dB using a sub-optimum bit-by-bit detector.

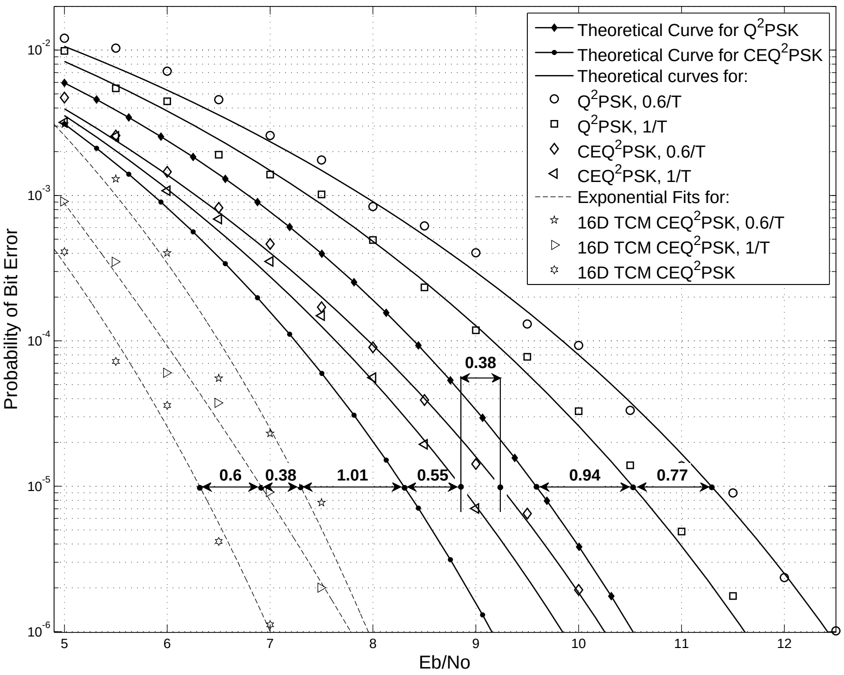

Figure 3.3: BER for Q^{2}PSK, CEQ^{2}PSK and 16D TCM CEQ^{2}PSK systems, filtered and unfiltered, when receiver has no knowledge of the channel.

We have shown in Fig. 3.4 that CEQ^{2}PSK achieves $P_{be} = 10^{-5}$ at an SNR of 9.3 dB if a sequence detector with no channel information is used instead, and only 8.8 dB if channel estimation is performed so that the filtered pulses are used in the receiver. Cartwright and Kaminsky [35] showed that an SNR of 8.3 dB is actually needed if the channel is not bandlimited, which is confirmed in Fig. 3.3.

For channel bandwidth of $0.6/T$, when TCM is used with the expanded 16D constellation, we achieve a BER of 10^{-5} with 7.3 dB if no knowledge of the channel is assumed (receiver 1) and with only 6.8 dB if knowledge of the channel (receiver 2) is assumed; the penalty paid for this gain is increased complexity in the receiver. The same conclusions are drawn about gains for channels with a bandwidth of $1/T$, as shown on Fig. 3.5. Notice, however, that at $1/T$ Q^{2}PSK gains less than the TCM system, while at $0.6/T$ the gain is larger. The gain due to knowledge of the channel is always smallest for 4D CEQ^{2}PSK.

Using channel estimation aids the 16D TCM system more than the 4D uncoded equivalent and knowledge of the channel is more important for Q^{2}PSK than for its constant envelope counterpart.

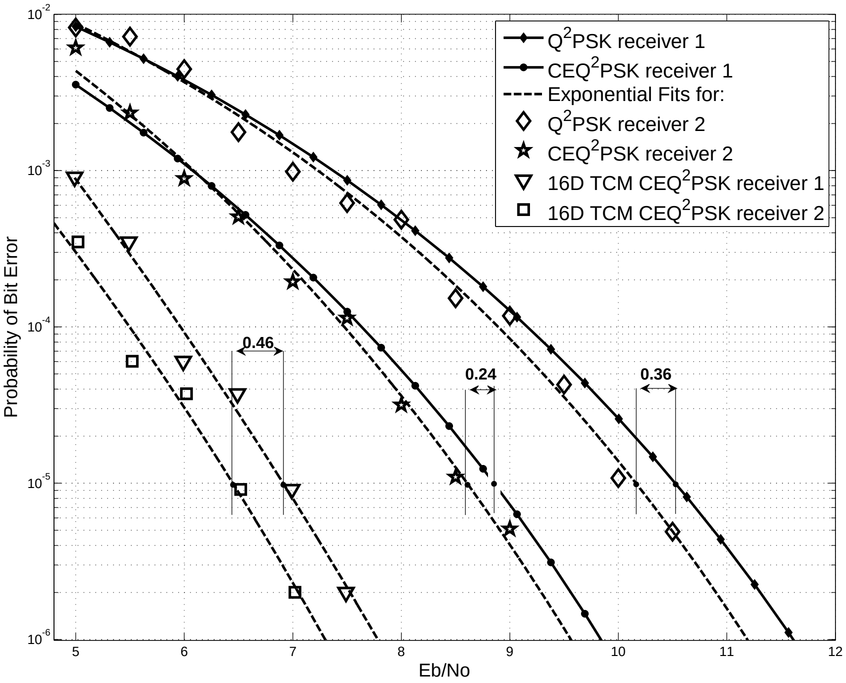

Figure 3.4: BER for Q^{2}PSK, CEQ^{2}PSK and 16D TCM CEQ^{2}PSK systems filtered at $0.6/T$ with receivers with and without channel knowledge (labeled receiver 2 and 1, respectively).

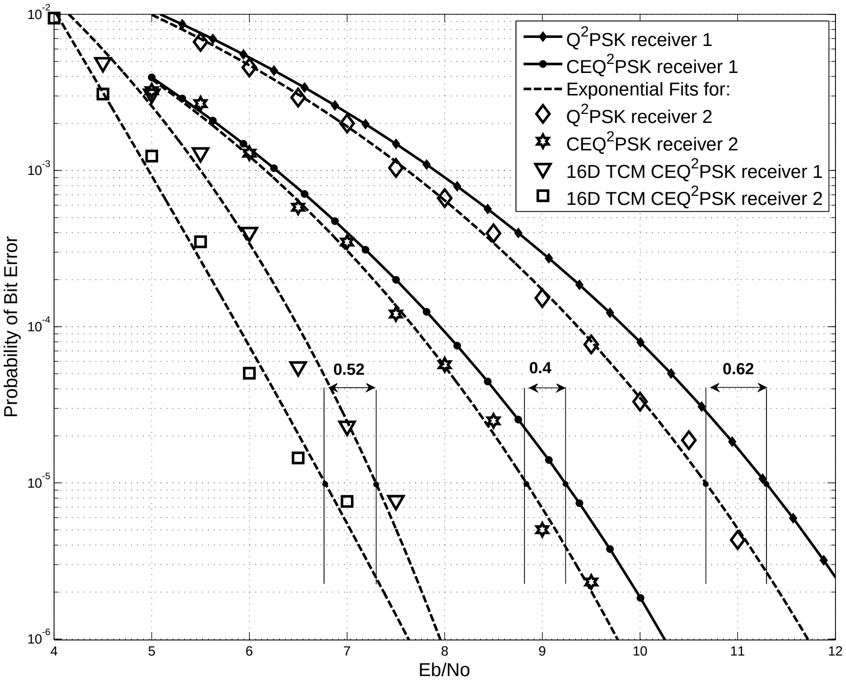

Figure 3.5: BER for Q^{2}PSK, CEQ^{2}PSK and 16D TCM systems filtered at $1/T$ with receivers with and without channel knowledge (labeled receiver 2 and 1, respectively).

3.7 Conclusions

We have presented the performance of Q^{2}PSK and its variants CEQ^{2}PSK and 16D TCM CEQ^{2}PSK in ideal bandlimited channels with and without channel knowledge at the receiver.

We have noted that the effect of bandlimitation to $0.6/T$, with T the 2D signaling interval, results in a needed increase of between 1 dB and 1.7 dB in SNR for a BER of 10^{-5} if no channel estimation is used and around 0.5 dB if knowledge of the channel is assumed. The best performance among the systems studied is that of the 16 TCM CEQ^{2}PSK system which requires less than 6.8 dB of SNR for that BER in the most severe bandlimitation, but requires a more complex receiver.

Future work will include simulations of the contant envelope 4D and 16D systems in fading channels and in the nonlinear satellite channel, where use of constant envelope systems becomes most important. Use of pulses that have narrower bandwidth such as those in [46] should also be evaluated in bandlimited channels. Phase estimation algorithms along with actual causal bandlimited channel models should be incorporated. We will also perform the analysis of ISI/CISI for Cartwright's CEQ^{2}PSK constellation, which is expected to be less affected by interference than Saha's.

Chapter 4 Visualization of Q^2PSK and CEQ^{2}PSK in ideal Bandlimited Channels

4.1 Introduction

Shannon proposed geometrical representations of signals in [1], where he discussed the association of information signals with Euclidean spaces, resulting in an understanding of the relationship between visual indicators and the performance of digital communications systems. Since then, effort has been devoted by other researchers to connect the multidimensional geometric representations to communication systems' waveforms and to visually represent these high-dimensional constellations in lower-dimensional spaces.

In [48, Fig.1], Saha and El-Ghandour present a 4D Q^2PSK signal space diagram where the four dimensions are decoupled into two 2D sub spaces associated with the half cosine and the half sine pulses; the diagram shows the decoupled phase points of Q^2PSK around each pulse axis. Similarly, in [58, Fig. 2.5] Cilliers describes a visualization of Q^2PSK where the signal constellations points are plotted around a frequency axis. Cilliers also discusses two graphical representations of the projection of the 4D Q^2PSK hypercube onto 3D cubes ([58, Figs. 2.10, 2.11]). These latter four representations aid in visualizing 4D systems, but provide no insight or information about the transmitted or received signals. Drakul and Biglieri [59, Figs. 2, 3] portray all pulses vs. time for one signaling interval and also eye patterns (see [59, Figs. 5, 7]) for an 8D Constant Envelope modulation Scheme (8D-CEMS). Malan shows in [60, Fig. 6.2] a complex 2D baseband envelope diagram of a 4D Direct Sequence Spread Spectrum (DSSS) signal to portray amplitude and phase distortions caused by a bandlimited channel.

In this paper, we discuss visualization methods for 4D Q^2PSK systems; in particular, we analyze Q^2PSK [33] and CEQ^{2}PSK [44, 20] systems with no channel bandlimitation as well as with ideal channel filters of baseband bandwidth $\frac{0.6}{T}$ and $\frac{1}{T}$, where $2T$ is the 4D symbol interval. Our first method, the time-signal eye pattern, consists of portraying the set of all possible 4D passband filtered signals versus time; we choose to display times from $-T$

to T, to show the entire 4D signaling interval, using the minimum carrier frequency. The second method is a 2D complex trajectory diagram in which the baseband in-phase and in-quadrature signals are plotted versus each other with time as a parameter. The third method represents the output of the matched filter (before the sample and hold operation) for each of the 4 components, versus time, for times between 0 and $2T$, to show the decision time in the middle.

The rest of this paper is organized as follows: The first section is a brief review of Q^{2}PSK and Saha's and Cartwright's CEQ^{2}PSK. Next, in Section 4.3, we present the visualization methods used. Results are presented and discussed in Section 4.4. Concluding remarks and proposals for future work are given in Section 4.5, followed by cited references.

4.2 Review of 4D Q^{2}PSK

In this section, we summarize Q^{2}PSK, Saha's CEQ^{2}PSK, and Cartwright's CEQ^{2}PSK.

4.2.1 Q^{2}PSK

Q^{2}PSK [33] is a 4D modulation scheme defined by:

$$\begin{gathered} S(t) = a_1 p_1(t)\cos(\omega_c t) + a_2 p_2(t)\cos(\omega_c t) + \\ + a_3 p_1(t)\sin(\omega_c t) + a_4 p_2(t)\sin(\omega_c t), \end{gathered} \tag{4.1}$$

where $\{a_i\}$, $i = 1, ..., 4$, are ± 1, the half-cosine and half-sine pulses, $p_1(t)$ and $p_2(t)$, are given by (4.2), the carrier angular frequency, ω_c, is $n\pi/2T$, with n $\geq$2, and T is the duration of 2 bits.

$$p_j(t) = \cos\left(\frac{\pi t}{2T} - \frac{(j-1)\pi}{2}\right), \quad |t| \leq T, \quad j = 1, 2. \tag{4.2}$$

Eq. (4.1) may also be represented as

$$S(t) = A(t)\cos\left(\omega_c t + \theta(t)\right), \tag{4.3}$$

where the amplitude and phase are given, respectively, by (4.4) and (4.5):

$$A(t) = \left(2 + (a_1 a_2 + a_3 a_4)\sin(\pi t/T)\right)^{1/2}, \tag{4.4}$$

$$\theta(t) = \tan^{-1}\left(\frac{a_3\cos(\pi t/2T) + a_4\sin(\pi t/2T)}{a_1\cos(\pi t/2T) + a_2\sin(\pi t/2T)}\right). \tag{4.5}$$

Equivalently, we could use a baseband model for (4.1) in which the k^{th} transmitted Q^2PSK signal is:

$$\begin{aligned} S_k(t) = {} & a_{1,k}p_1(t-2kT) + a_{2,k}p_2(t-2kT) + \\ & -j[a_{3,k}p_1(t-2kT) + a_{4,k}p_2(t-2kT)]. \end{aligned} \tag{4.6}$$

The real part of (4.6) is the in-phase component, I, and the imaginary part corresponds to the quadrature-phase, Q. There are 16 4D symbols that form this non-constant envelope Q^2PSK signal set. Saha's Q^2PSK points are listed on the left side of Table 4.1; we have separated the eight points that have constant envelope (listed in the bottom) from the other eight. The fourth component of the top eight Q^2PSK vectors is $a_4 = a_1a_2/a_3$ while for the bottom eight, this component is $a_4 = -a_1a_2/a_3$. For the top 8 points the phase is piecewise-constant with values $\theta(t) \in \{\pm 45°, \pm 135°\}$; the bottom 8 points have phase that increases or decreases piece-wise linearly.

4.2.2 CEQ^{2}PSK

In [44] and [20], respectively, two 4D constant envelope constellations were introduced: Saha's CEQ^{2}PSK and Cartwright's CEQ^{2}PSK. Constant envelope is obtained at the expense of a reduction in the transmission rate, by ensuring that $a_4 = -a_1a_2/a_3$. Each set has eight 4D symbols and makes $A(t)$ in (4.4) a constant value equal to $\sqrt{2}$ [20]. The original two CEQ^{2}PSK constelations are those listed on the bottom half of Table 4.1 as having magnitude $\sqrt{2}$. Notice that there are two constellations of Cartwright-type symbols: Cartwright's original constellation presented in [20], listed on the bottom right corner of Table 4.1, and

Table 4.1: 4D Q^2PSK points.

	Saha's				Cartwright's				
	a_1	a_2	a_3	a_4	a_1	a_2	a_3	a_4	
Magnitude: variable Phase: ±45° ±135°	-1	-1	-1	-1	0	$-\sqrt{2}$	0	$-\sqrt{2}$	Magnitude: $\sqrt{2}$ Phase: ±45° ±135°
	-1	-1	1	1	0	$-\sqrt{2}$	0	$\sqrt{2}$	
	-1	1	-1	1	$-\sqrt{2}$	0	$-\sqrt{2}$	0	
	-1	1	1	-1	$-\sqrt{2}$	0	$\sqrt{2}$	0	
	1	-1	-1	1	$\sqrt{2}$	0	$-\sqrt{2}$	0	
	1	-1	1	-1	$\sqrt{2}$	0	$\sqrt{2}$	0	
	1	1	-1	-1	0	$\sqrt{2}$	0	$-\sqrt{2}$	
	1	1	1	1	0	$\sqrt{2}$	0	$\sqrt{2}$	
Magnitude: $\sqrt{2}$ Phase: piecewise linear	-1	-1	-1	1	0	$-\sqrt{2}$	$-\sqrt{2}$	0	Magnitude: $\sqrt{2}$ Phase: piecewise linear
	-1	-1	1	-1	0	$-\sqrt{2}$	$\sqrt{2}$	0	
	-1	1	-1	-1	$-\sqrt{2}$	0	0	$-\sqrt{2}$	
	1	-1	-1	-1	$\sqrt{2}$	0	0	$-\sqrt{2}$	
	1	1	1	-1	0	$\sqrt{2}$	$\sqrt{2}$	0	
	1	1	-1	1	0	$\sqrt{2}$	$-\sqrt{2}$	0	
	1	-1	1	1	$\sqrt{2}$	0	0	$\sqrt{2}$	
	-1	1	1	1	$-\sqrt{2}$	0	0	$\sqrt{2}$	

another we are presenting here for the first time, listed on the top right corner of this same table. This constellation also has constant envelope with $A(t) = \sqrt{2}$, for all t, but has piecewise constant phase, while Cartwright's original CEQ^2PSK constellation has piecewise-linear phase.

4.3 Visualization Methods

In this section we explain the graphical representations used to visualize the signals of interest.

4.3.1 Time-signal eye patterns for 4D passband signals

The time-signal eye pattern is obtained by plotting (4.1) or (4.3) with $\omega_c = \pi/T$, or the channel-filtered version of these, for all combinations of possible 4D signals, versus time. Any other allowed carrier frequency may be chosen, but no further insight about the modulated signals is obtained by doing this. These signals are presented on the same graph over a period of $2T$ –the length of one 4D symbol– showing a complete 4D signaling interval from $-T$ to T. Notice that (4.1) and (4.3) depend on $[a_1\, a_2\, a_3\, a_4]$ which for CEQ^{2}PSK is a subset of the possible Q^{2}PSK vectors (see Table 4.1). By using this method, the amplitude and phase of the passband signal are shown graphically for all times.

4.3.2 2D complex trajectory diagrams for 4D baseband signals

With this method we look at the baseband version of the 4D modulated signal in the complex plane by showing parametric plots of the trajectories of the in-phase component versus the quadrature-phase component of the signal in (4.6), or a filtered version of it as shown in (6) of [34]. Effectively, the 2D complex trajectories are polar diagrams of the magnitude in (4.4) and the phase in (4.5) –or, again, filtered versions of these– with time as a parameter. The trajectory diagram clearly shows distortions caused by the ISI created by the bandlimited channel.

4.3.3 Time-signal eye pattern for the 1D outputs of the baseband matched filter

The baseband receiver, consisting of a bank of two pairs of matched filters, separates the real parts (in-phase) from the imaginary parts (quadrature-phase) and also the half-cosine pulses from the half-sine pulses. We also use time-signal eye diagrams to show each component of the baseband signals at the output of the matched filter. All possible signals for each component are superimposed, for a single signaling interval. The four signals at the output of the matched filter, if the channel has infinite bandwidth, are:

$$\begin{aligned} y_k(t) &= a_k p_1(t) * h_1(t) + a_{k+1} p_2(t) * h_1(t) \\ &= a_k y'_{11}(t-T) + a_{k+1} y'_{12}(t-T), \qquad (4.7a) \\ y_m(t) &= a_{m-1} p_1(t) * h_2(t) + a_m p_2(t) * h_2(t) \\ &= -a_{m-1} y'_{12}(t-T) - a_m y'_{22}(t-T), \qquad (4.7b) \end{aligned}$$

for $k = 1, 3$, $m = 2, 4$, and y'_{ij} given in (4.8). The matched-filter impulse responses are $h_1(t) = p_1(T-t)$ and $h_2(t) = p_2(T-t)$, with $p_j(t)$ given in (4.2).

$$\begin{aligned} y'_{ij}(t) = \frac{(-1)}{2}^{(i-1)(j-1)} &\cos\left[\frac{\pi}{2}\left(\frac{t}{T} - |i-j|\right)\right](2T - |t|) + \\ &+ \frac{T}{\pi}\sin\left(\frac{\pi|t|}{2T}\right)|3-i-j|, \quad |t| \le 2T, \qquad (4.8) \end{aligned}$$

for $i, j = 1, 2$.

The open parts of the time-signal eye patterns occur around decision time T. For Saha's signals there is a single eye, while for Cartwrights' there are two, as three levels are possible. The horizontal eye opening relates to the phase and shows the sensitivity to sampling instant shifts (i.e., synchronization). In addition, the amplitude distortion at the sampling time – which relates directly to the modified geometry of the 4D signals with ISI– also becomes obvious.

4.4 Visualization Results

In this section we present and discuss the results of our visualization analysis of Q^{2}PSK signals.

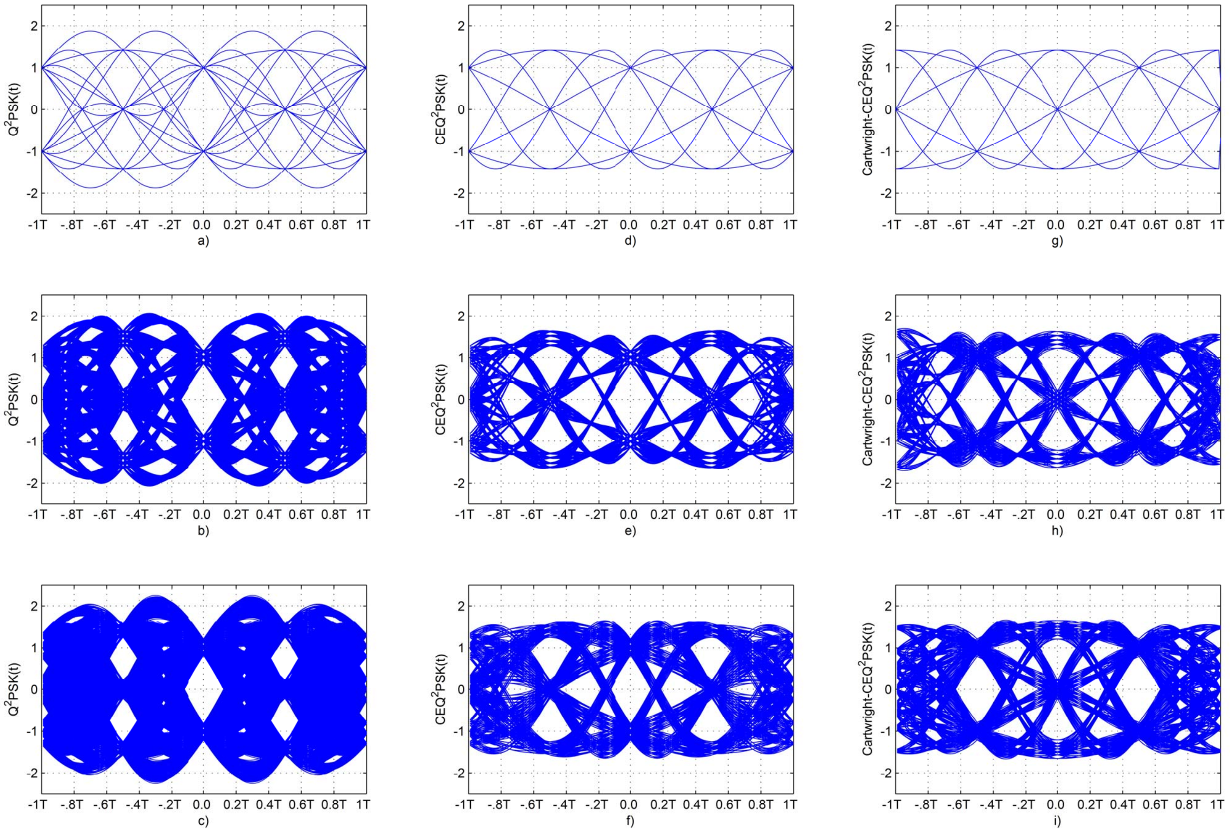

Figure 4.1: Time-signal eye patterns for 4D passband signals. Q^{2}PSK: a) unfiltered, b) filtered at B_1, c) filtered at B_2. Saha's CEQ^{2}PSK: d) unfiltered, e) filtered at B_1, f) filtered at B_2. Cartwright's CEQ^{2}PSK: g) unfiltered, h) filtered at B_1, i) filtered at B_2. $B_1 = 1/T, B_2 = 0.6/T$.

4.4.1 Time-signal eye patterns for 4D passband Q^{2}PSK

Figure 4.1 portrays the time-signal eye patterns for the three 4D passband systems of interest. The columns correspond, respectively, to Q^{2}PSK, Saha's CEQ^{2}PSK, and Cartwright's original CEQ^{2}PSK. The rows represent the bandwidth limitation: for the plots on the top row there is no channel filter, while the second and third rows have channels bandlimited to $\frac{1}{T}$ and $\frac{0.6}{T}$, respectively, where 2T is the 4D symbol interval. We see in a) the 16 traces of all possible Q^{2}PSK 4D symbols, with symbol transitions occurring at time 0 and $2T$ and possible phase changes of 0, ±90° and ±180°, as stated in [33]. For the filtered Q^{2}PSK signals there are 4096 traces on the 4D passband time-signal eye patters because one past, one present, and one future symbol affect the current symbol, and each one of these has 16 possible values. If one compares a) to b) and c), it becomes clear that amplitude distortion is introduced by the bandlimited channels. The possible values of the signal with ISI are no longer just ±1, and many new phase changes occur.

Results for Saha's and Cartwright's original CEQ^{2}PSK are portrayed in the second and third columns of Fig. 4.1, respectively. Because d) and g) show the signals without bandlimitation, there are 8 traces displayed. The symbol transitions again occur at time 0 and $2T$ and we also have possible abrupt changes in phase at those times. The possible phase shifts are still 0, ±90° and ±180°, as they were for Q^{2}PSK. Because e), f), h) and i) depict signals with ISI, there are 512 traces when the memory is truncated to three symbols. When Cartwright's original CEQ^{2}PSK is used, the possible values of the unfiltered 4D signal at time T are 0 and $\pm\sqrt{2}$; clearly, the 4D Euclidean distances at that time are equal for Saha's and Cartwright's constellations, but at time T the minimum distance has been reduced from 2 to $\sqrt{2}$ while the maximum distance has been increased from 2 to $2\sqrt{2}$.

4.4.2 2D complex trajectory diagrams for Q^{2}PSK signals

Figure 4.2 shows the complex trajectory diagrams for the systems of interest. Notice that both the amplitude and phase information of the 4D signals are shown with time as a parameter, by plotting the in-phase component vs. the quadrature-phase. Because time is not shown, the abrupt phase changes of the unfiltered signals are only easily seen in Fig. 4.2 a), i.e., for Q^{2}PSK. On the other hand, the constant envelope is obvious for the CEQ^{2}PSK untilftered systems shown in d) and g). It is also clear that the complex trajectory diagram for Cartwright's CEQ^{2}PSK is a 45° rotation of the diagram for Saha's CEQ^{2}PSK; as noted in [20], Cartwright's constellation is obtained by performing two 2D rotations of 45° on Saha's 4D points. Notice that the ISI-distorted CEQ^{2}PSK signals are no longer of constant envelope and may even be zero at certain instants.

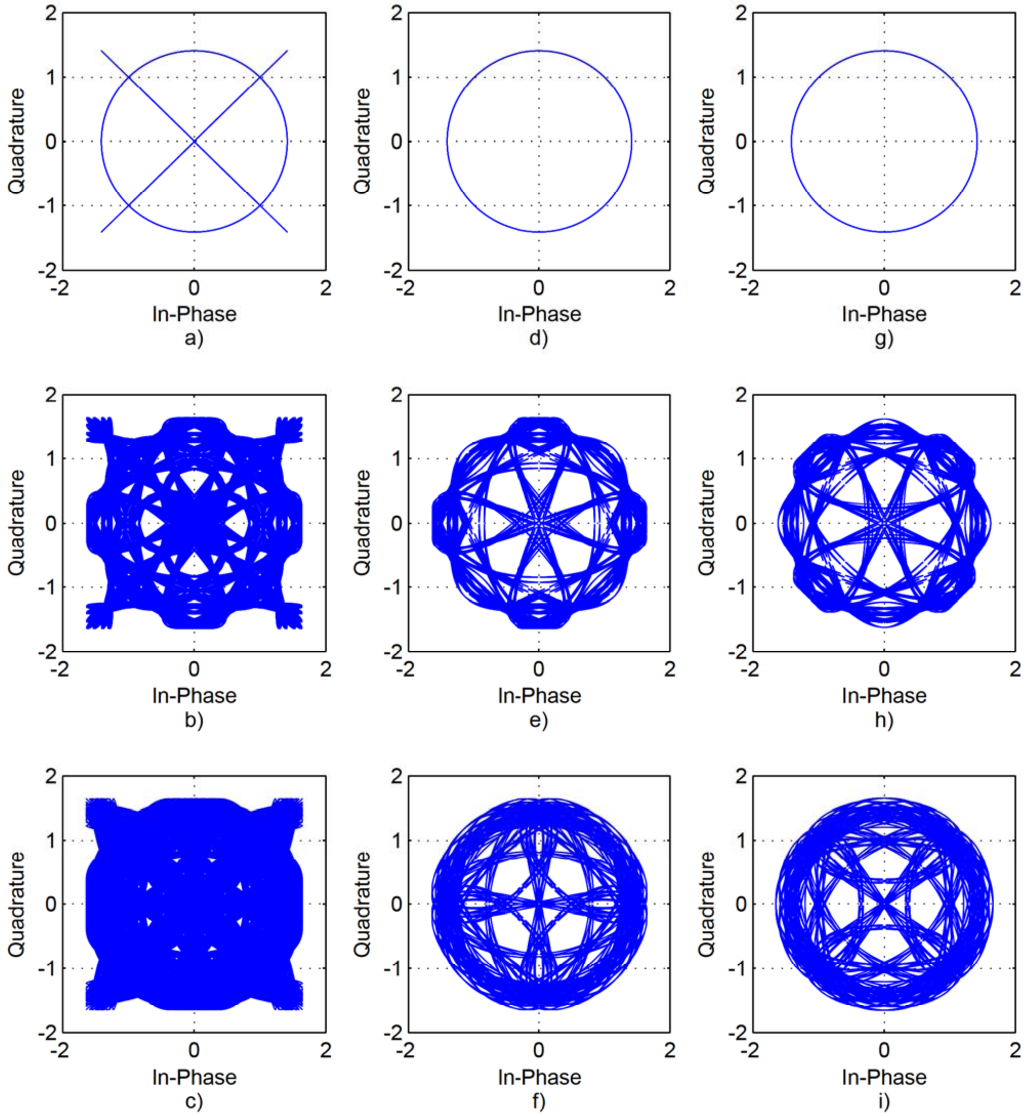

Figure 4.2: 2D complex trajectory diagrams. Q^2PSK: a) unfiltered, b) filtered at B_1, c) filtered at B_2. Saha's CEQ^2PSK: d) unfiltered, e) filtered at B_1, f) filtered at B_2. Cartwright's CEQ^2PSK: g) unfiltered, h) filtered at B_1, i) filtered at B_2. $B_1 = 1/T, B_2 = 0.6/T$.

4.4.3 Time-signal eye patterns of the 1D baseband matched filter outputs for Q^2PSK

The time-signal eye pattern at the output of the matched filter helps visualize the signal geometry because the new coefficients $\hat{c}_i$ that arise from the signal with ISI become clear at time T, the sampling time of the sample and hold device at the receiver. The possible values of (4.7a) and (4.7b) are plotted on the first row of Fig. 4.3; a) and d) correspond to Q^2PSK and Saha's CEQ^2PSK, while g) and j) are for Cartwright's original CEQ^2PSK. The computed values of these coefficients are given in Table 4.2 for Cartwright's original constellation at the two bandwidths of interest to us, and on Table I of [34] for Saha's constellation. These coefficients are the possible values at $t = T$ when the ISI is truncated to three signaling intervals. The numbers listed in the last column, N, indicate the number of occurrences of each coefficient in the new geometry; there are a total of 512 signal points.

Table 4.2: Magnitude of the Coefficients for two channel bandwidths for Cartwright's CEQ^{2}PSK.

$B_1 = \frac{1}{T}$		$B_2 = \frac{0.6}{T}$		
$\hat{c}_1$ or $\hat{c}_3$	$\hat{c}_2$ or $\hat{c}_4$	$\hat{c}_1$ or $\hat{c}_3$	$\hat{c}_2$ or $\hat{c}_4$	N
0	0	0	0	64
0.001915	0.007582	0.005313	0.016256	32
0.003751	0.073442	0.005448	0.085718	64
0.005666	0.081023	0.010759	0.101973	64
0.007582	0.154465	0.016207	0.187691	32
1.403177	1.107992	1.380991	0.988777	16
1.405092	1.181434	1.386439	1.074494	32
1.407008	1.189016	1.391751	1.160212	16
1.408843	1.254875	1.391887	1.090750	32
1.410759	1.262457	1.397199	1.176467	64
1.414509	1.270039	1.402510	1.192723	16
1.412674	1.335899	1.402646	1.262185	32
1.416425	1.343481	1.407958	1.278441	32
1.418340	1.416922	1.413406	1.364158	16

The vertical (amplitude) and horizontal (time) eye openings at the output of the matched filter are listed in Table 4.3 for the systems of interest, both filtered and unfiltered; we also show the percentage decrease in the length of the eye opening in each direction, as it is this decrease in the size of the eye that helps us visualize the likelihood of detection errors. We define the vertical aperture, VA, as the minimum 1D distance between possible amplitudes at sampling time T. The horizontal aperture, HA, for unfiltered signals is defined as the length of time between signal crossings (excluding those with 0-amplitude crossing). When the signals are filtered, we measure the corresponding minimum distance. Both VA and

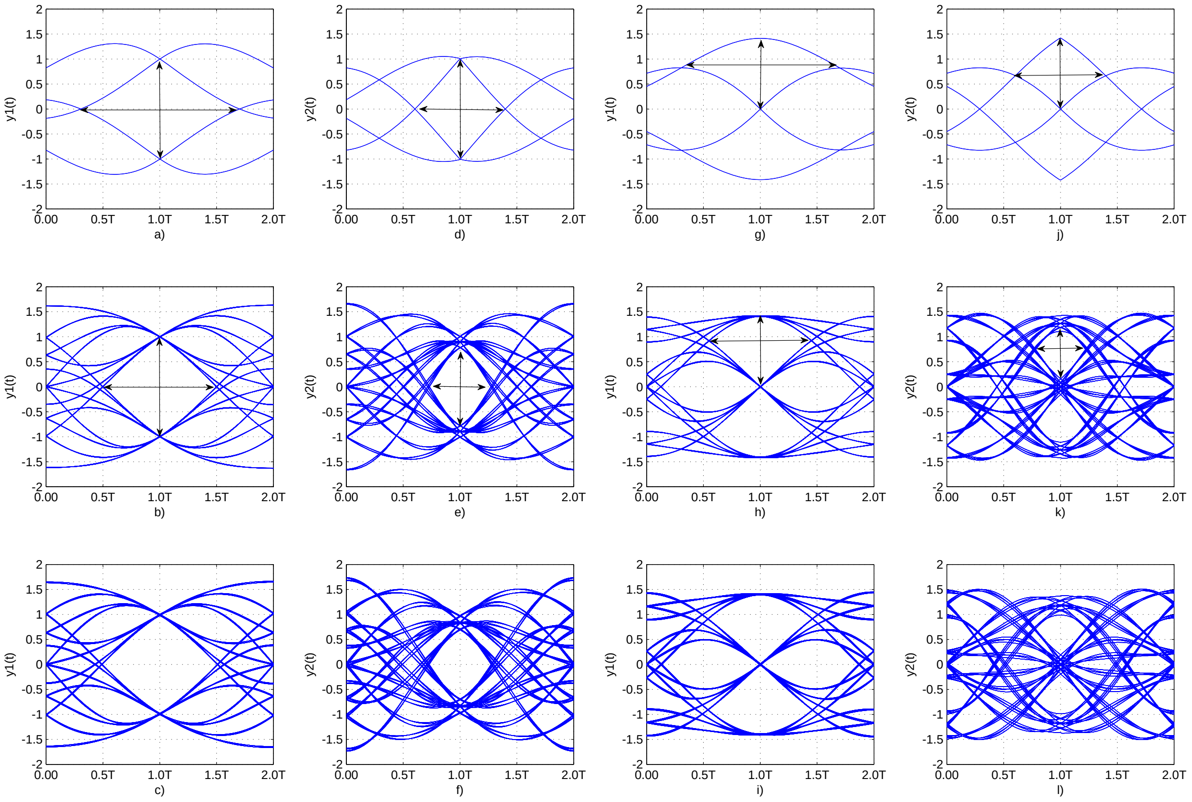

Figure 4.3: Time-signal eye patterns of the 1D output of the baseband matched filter. Q^2PSK and Saha's CEQ^2PSK: a) unfiltered a_1 and a_3, b) a_1 and a_3 filtered at B_1, c) a_1 and a_3 filtered at B_2, d) unfiltered a_2 and a_4, e) a_2 and a_4 filtered at B_1, f) a_2 and a_4 filtered at B_2. Cartwright's CEQ^2PSK: g) unfiltered a_1 and a_3, h) a_1 and a_3 filtered at B_1, i) a_1 and a_3 filtered at B_2, j) unfiltered a_2 and a_4, k) a_2 and a_4 filtered at B_1, l) a_2 and a_4 filtered at B_2. $B_1 = 1/T$, $B_2 = 0.6/T$.

HA are indicated with arrows on Fig. 4.3. The amplitude distortions that correspond to the cosine pulses is always small, while it is considerably larger for the sine pulses. The sine components are also more prone to timing errors, as seen by the eye narrowing in the horizontal direction. The probability of error performance in Additive White Gaussian Noise (AWGN) channels depends on the minimum Euclidean distance between 4D points. One must remember that for Cartwright's constellation, if the amplitude of one half-cosine pulse is not 0, the other one is and that the same applies to the half-sine pulses. This means that, without error correction, the apertures may be minimum in all components of Saha's constellation, while this is not possible in Cartwright's.

Table 4.3: Amplitude and time apertures at matched filter output.

			$B_o = \infty$	$B_1 = \frac{1}{T}$		$B_2 = \frac{0.6}{T}$	
			Aperture	Aperture	% decrease	Aperture	% decrease
Saha's Q^{2}PSK & CEQ^{2}PSK	$y_1(t)$	VA	2.00	1.98	1.00	1.95	2.50
		HA	1.4T	1.0T	28.57	1.0T	28.57
	$y_2(t)$	VA	2.00	1.56	22.00	1.37	31.50
		HA	0.8T	0.6T	25.00	0.6T	25.00
Cartwright's CEQ^{2}PSK	$y_1(t)$	VA	$\sqrt{2}$	1.40	1.00	1.36	3.83
		HA	1.4T	0.8T	42.85	0.8T	42.85
	$y_2(t)$	VA	$\sqrt{2}$	0.95	32.83	0.80	43.43
		HA	0.8T	0.4T	50.00	0.4T	50.00

4.5 Conclusions and Further Work

We have presented visualization aids for 4D Q^{2}PSK, both constant and non-constant envelope, as well as filtered and unfiltered. This is an effort to gain insight into the behaviour of these signals in bandlimitted channels. The diagrams shown help to visualize the causes of the degradation in probability of error performance when the channel is bandlimitted and therefore ISI is introduced.

Future work will include a thorough evaluation of the performance of both of Cartwright's CEQ^{2}PSK constellations in bandlimitted channels and a comparison to Saha's. Better models of bandlimitted and fading channels will be used.

We will also apply a continuous Morlet wavelet transform to Q^{2}PSK systems, which shall be used to visualize, simultaneously, the time-frequency behavior of the bandlimited signals and used to develop a wavelet-based receiver that estimates the phase-shift, ISI, and noise-type of actual channels. The performance of such receiver is expected to be superior to the standard matched filter –optimum in AWGN– when other deleterious effects are introduced by the channel, particularly in the presence of impulsive and colored noise.

Chapter 5 Spectral Analysis and Eye Diagrams for 16D CEQ^{2}PSK data rate

This Chapter discuss in more detail of some simulations performed for Chapter 4. Discussions about some work on the spectral efficiency issues are presented. The more compact the spectrum of the transmitted signals, the better, as less energy will be removed by filtering or less aliasing will be caused by sidelobes if not filtered fully. The size of the sidelobes –or the rate at which they decrease– is of much interest as well. Our spectral analysis is based on the Power Spectral Density (PSD) derivation and plots.

Eye diagrams or signal trajectory plots for the 16D system provide quite a bit of information regarding system performance. Information about distortion (e.e., by inter-symbol interference (ISI) or noise), synchronization, appropriateness of sampling times, and zero crossings, among others, may be derived or seen directly by analyzing signal trajectories and eye diagrams.

5.1 Power Spectral Density

The theoretical PSD, in dB, versus normalized frequency (fT_b), for the 16D original (non-constant envelope) Q^{2}PSK, the unexpanded 16D CEQ^{2}PSK (it is the same whether Saha's or Cartwright's points are used), and the expanded 16D CEQ^{2}PSK (where both Saha and Cartwright points are present), are shown in Fig. 5.1. This Figure, then, shows theoretial PSD. The PSDs obtained during simulation, averaged over 500 traces are shown in Fig. 5.2. Fig. 5.2, then, shows the experimental PSD of the systems and includes the PSD of our TCM 16D CEQ^{2}PSK system. We do not have a theoretical derivation of the PSD for the encoded system, but we have derived (and shown in Fig. 5.1) the theoretical values for the uncoded expanded and unexpanded systems. The 16D non-constant envelope Q^{2}PSK system, shown with large dashes is clearly the most compact of those evaluated. The first lobe is 0.375 wide in terms of normalized frequency. The expanded CEQ^{2}PSK system, without coding, may be used to transmit at higher bandwidth efficiency and still retain constant envelope. The

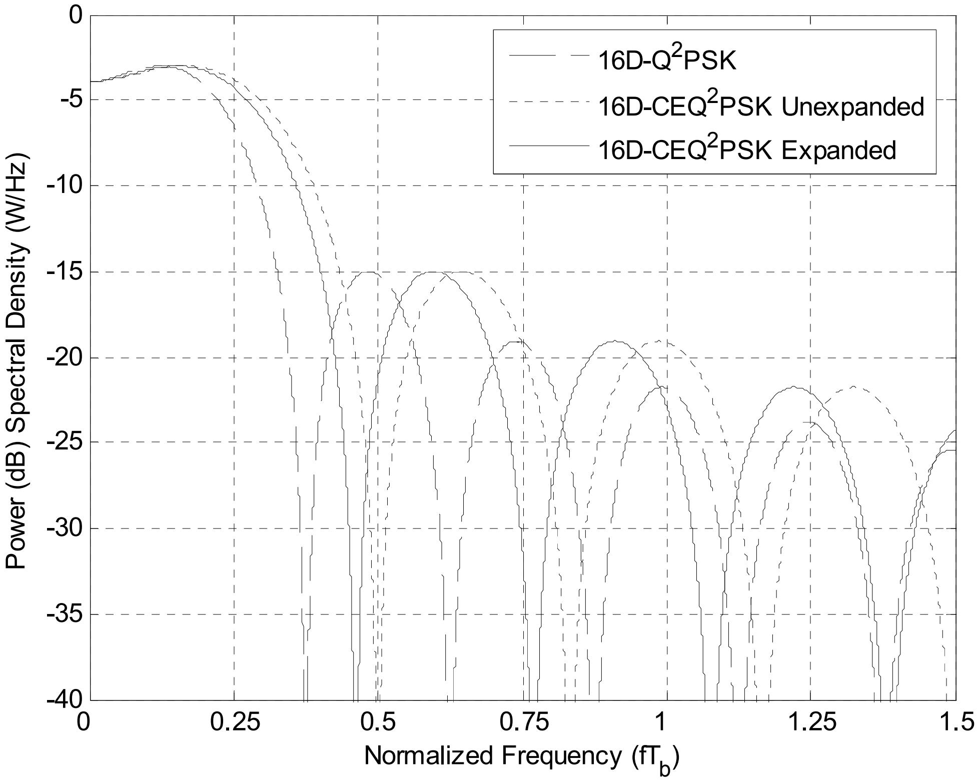

Figure 5.1: Theoretical PSD vs. normalized frequency for various 16D Q^2PSK schemes. Expanded and unexpanded constant envelope (CE Q^2PSK) systems and Saha's original (non CE) Q^2PSK are shown.

first lobe of the expanded constellation, compared to that of the unexpanded constellation's first lobe is narrower by about .12.

5.2 Eye Diagrams

This section briefly studied the signal constellation point trajectories and eye diagrams of our 16-D CEQ^2PSK system and similar ones. For CEQ^2PSK, the transitions versus time may start and end at 0, ± 1, and $\pm\sqrt{2}$. The diagram in time-series form is shown in Fig. 5.3. Our system does have four transitions which cross zero, but has many others which do not. Sensitivity to timing errors is elevated in 4 for CEQ^2PSK . Remember, though, that our expanded constellation allows for redundancy to be introduced.

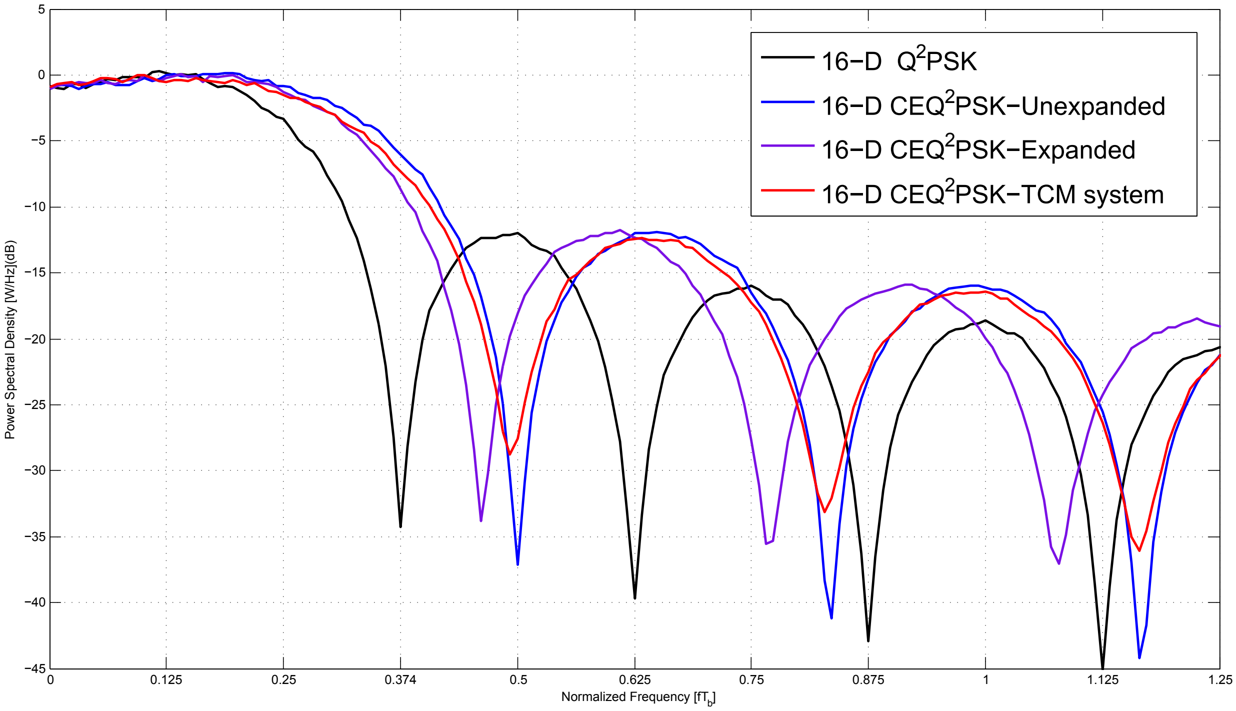

Figure 5.2: Practical PSD vs. normalized frequency for the 16D Q^2PSK schemes. Expanded and unexpanded constant envelope (CE Q^2PSK) systems and Saha's original (non CE) Q^2PSK are shown. Plots are averages of 500 simulations.

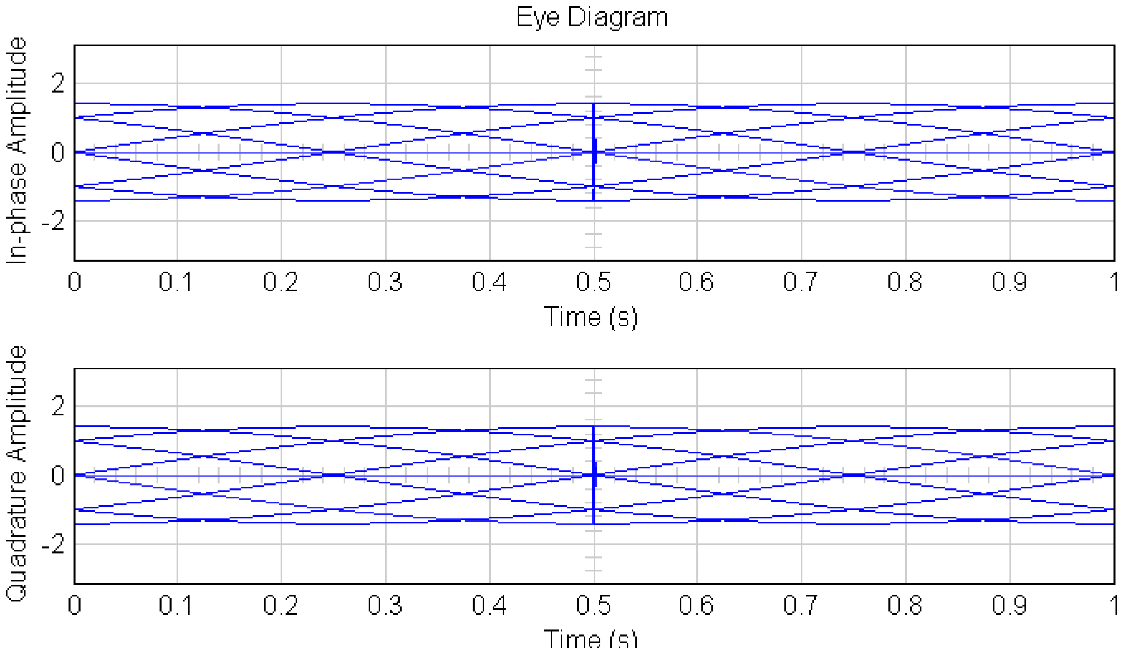

Figure 5.3: Signal transitions for CEQ^2PSK system for $T_{sym} = 1$ s.

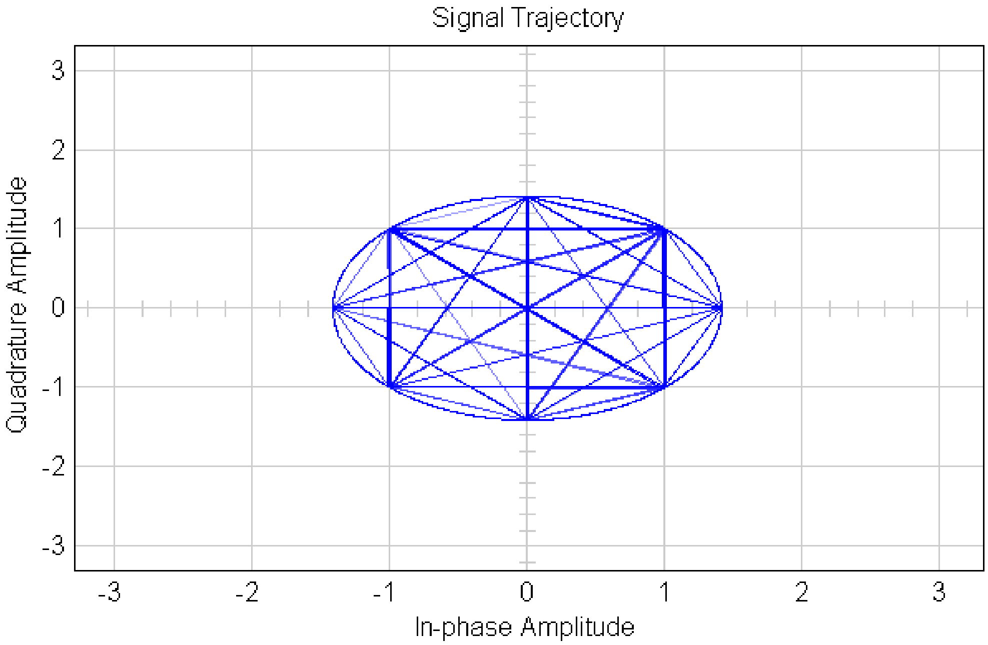

Figure 5.4: Signal trajectories (in 2D) for the CEQ^{2}PSK system.

Chapter 6 Information rate for 16-D CEQ^{2}PSK

In [21], the expanded constellation was used to allow for 1 bit of redundancy per 16-D to be introduced through a convolutional encoder in a TCM system. The improved probability of error performance in [21] is achieved while maintaining constant envelope with a slight increase in the complexity of the decoder. In this chapter, we discuss the use of the expanded 8192-point 16-D CEQ^{2}PSK constellation without coding, where the additional bit is used to increase the bandwidth efficiency while only slightly deteriorating the probability of error performance. The TCM system transmits 12 information bits per 16-D symbol while the current system transmits 13 information bits over the same 8T interval.

6.1 System Description

We briefly describe the implemented system in this Section; the transmitter and receiver use look-up tables to map 13 bits to the 8192 symbols, or 8192 symbols to 13 bits, respectively. Fig. 6.1 shows a block diagram of the proposed communication system.

6.1.1 Expanded 16-D CEQ^{2}PSK Transmitter

An information source generates bits at a fixed bit rate of $1/\mathrm{T}_b$, with $\mathrm{T}_b = 8\mathrm{T}/13$. During each 16-D signaling interval (8T), the source passes, through a buffer, 13 bits to a bit-to-integer converter which outputs an integer number between 0 and 8191. The transmitter look-up table receives one symbol index every $13\mathrm{T}_b$. The look-up table consists of 8192 16-D points; the top 4096 signal points are the 16-D CEQ^{2}PSK points from Saha's constellation and the other 4096 points are Cartwright's. The second buffer is used to effectively split the 16-D symbol into four consecutive 4-D symbols of the same type; each of these goes to the standard 4-D CEQ^{2}PSK modulators (which produce analog signals of duration 2T).

The generated analog waveforms are transmitted through the channel, assumed here to be

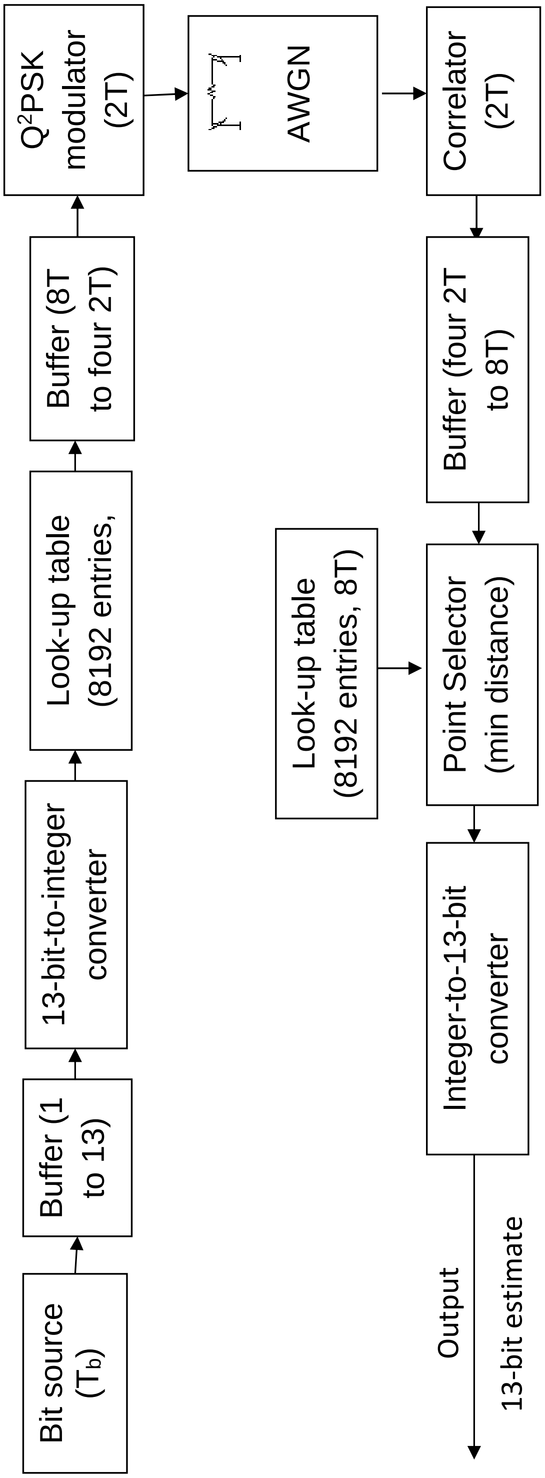

Figure 6.1: Functional block diagram of the increased-rate expanded 16-D CEQ^{2}PSK system.

AWGN with two-sided power spectral density $N_o/2$ in each component.

6.1.2 Expanded 16-D CEQ^{2}PSK Receiver

At the receiver, the noisy analog signals are correlated, every 2T, with the Q^{2}PSK basis vectors, with the use of multipliers followed by integrate-and-dump subsystems. Four consecutive signals are then concatenated with the aid of a buffer to generate a 16-D vector with real components. The Point Selector takes this vector and finds the entry in the receiver's look-up table which is closest in Euclidean distance to the received vector, and outputs an integer number between 0 and 8191. This integer is then converted to 13 output bits which are the estimates of the transmitted information bits.

The scheme implemented does not take advantage of knowing that the four consecutive 4-D signals in the 16-D symbol must come from either Saha's or Cartwright's constellations and is therefore sub-optimum (i.e., a correction is possible but not performed here). The optimum hardware detectors of [21] and [35] may be used to implement the receiver in an optimum manner.

6.2 Results

We analyze our system in terms of its probability of error versus SNR performance. In order to determine the performance of our system, Monte Carlo simulations were performed. For each SNR value, the simulations ran until twenty errors were counted [41]. Fig. 6.2 shows the results of these simulations as probability of bit error and probability of 16-D symbol error. The broken lines are the best exponential fits to the Monte Carlo results using expanded 16-D CEQ^{2}PSK at 3.25 bits/s/Hz. The continuous lines are the theoretical curves for the unexpanded (3 bits/s/Hz) CEQ^{2}PSK system (the bit error rate assumes 1.5 bits in error per 4-D CEQ^{2}PSK symbol error.) It is clear that the symbol (bit) performance of the expanded, higher-rate system is degraded by about 0.5 dB (.23 dB) at low SNR, when compared to the lower-rate, unexpanded 16-D CEQ^{2}PSK; however, at useful moderate SNR values, the symbol loss is less than 0.15 dB, as shown for $P_s(E) = 10^{-5}$ in Fig. 6.2. Notice that, effectively, we have traded about 0.15 dB of SNR for 0.25 bits/s/Hz in bandwidth efficiency by using the expanded constellation. The curves that show the probability of bit error tend to merge early because at high SNR the probability of the second nearest neighbor of the expanded constellation being selected as the transmitted signal approaches zero; i.e., the first approximation for expanded and unexpanded $P_b(E)$ are identical (because both have the same MSED and same number of nearest neighbors at this minimum distance.)

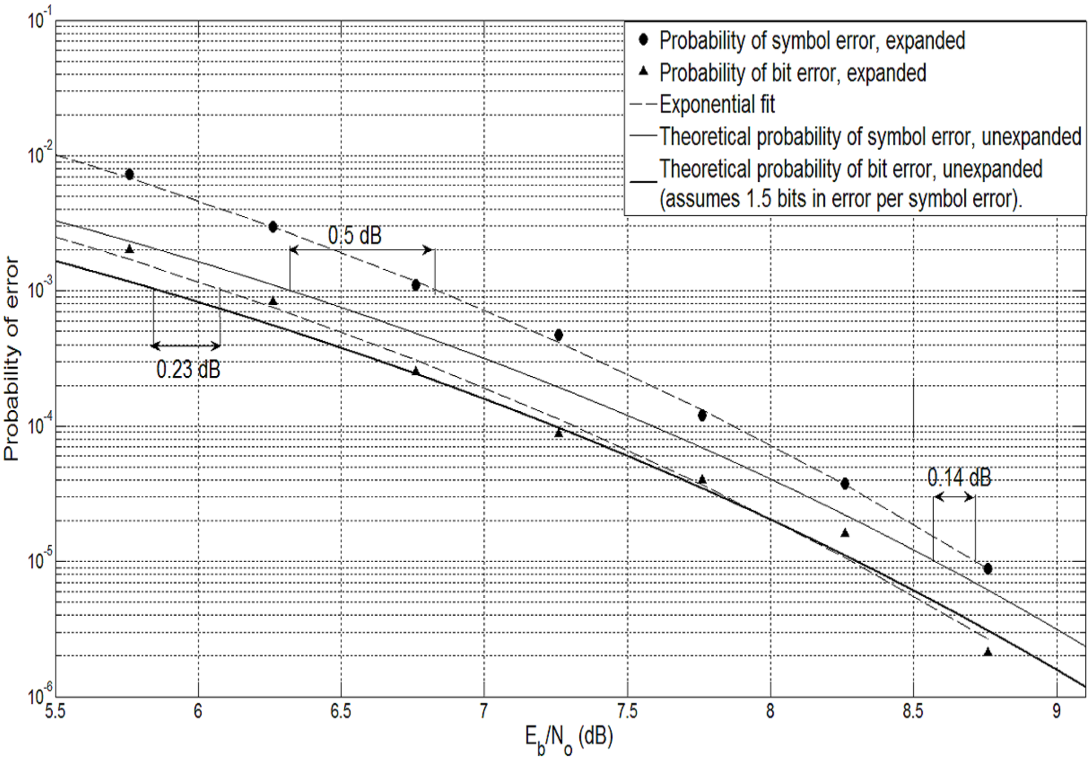

Figure 6.2: Symbol and bit error probabilities as functions of SNR, E_b/N_o, for expanded and unexpanded 16-D CEQ^{2}PSK.

6.3 Conclusions and Suggestions for Further Work

In this chapter we used the expanded 8192-point 16-D CEQ^{2}PSK constellation introduced in [20] to increase the information transmission rate over that of standard CEQ^{2}PSK from 3 bits/s/Hz to 3.25 bits/s/Hz. This increase is achieved at the cost of about half a dB for low SNR, and less than .15 dB for moderate to high SNR in AWGN. The system presented may be optimally implemented in hardware.

Chapter 7 TCM and Constellation Partitions for Fading Channel

Trellis-coded modulation schemes with multidimensional signals allow for improvement in performance over classical TCM with 2D constellations (see, for example, [32, 39]). These multidimensional schemes, however, all suffer from constellation expansion penalty as they increase the modulation level in order to introduce redundancy.

Acha and Carrasco [52] and Saha [19] utilize Saha's standard 4D Q^2PSK constellation for their TCM systems along with convolutional encoders of different rates. These schemes achieve some gains at the cost of reduced data rate. In addition, some of the Q^2PSK trellis codes proposed by Saha, Acha and Carrasco do not have constant envelope. Their constant envelope TCM systems are obtained by further reducing the data rate by half. The work on this thesis, based on Kaminsky's previous work reported in [22, 31] allows TCM to be implemented without constellation expansion penalty, i.e., without increasing the modulation level for a given MSED, an without reducing the data rate when using CEQ^2PSK.

For this dissertation, the expanded constellation discussed in Section 1.1.4 is used to implement simple multidimensional TCM systems that use low-rate convolutional encoders to achieve moderate gains over uncoded CEQ^2PSK in fading non-linear and AWGN channels. Because nonlinear channels require constant envelope signals, this 16D CEQ^2PSK TCM system is a good option in channels that require non-linear power amplifiers or that are inherently non-linear in themselves. Larger coding gains than those presented here are easily achieved with this constellation by using higher-rate encoders along with the appropriate partitions.

Hardware detectors for the constituent 4D CEQ^2PSK constellation were presented by Kaminsky and Cartwrigth and by Quinteros et al., respectively, in [35] and [21]. Although it is certainly possible and advantageous to use these hardware detectors in the actual implementation of the systems we present and evaluate here, we base all our current work on Matlab Simulink© models which don't implement these directly. Future work, however (see Section 11), should be done to develop an FPGA-based prototype of our 16D-TCM CEQ^{2}PSK systems.

7.1 Set Partitioning

TCM schemes require a proper set-partitioning [37] of the constellation in order to increment the free distance, d$_f$, of the code[1]. Details of the partition of the expanded 16D CEQ^{2}PSK constellation into 8 subsets optimum for AWGN –namely, Partition A or 1– are presented in [21]. This partition, along with two others (which are briefly presented in what follows) are used in the work reported here. We therefore have used three different partitions of our expanded constellation for this dissertation:

- The original 8-subset partition of [21], optimum for AWGN.
- A second 8-subset partition which is not optimum in AWGN channels, expected to perform better in Fading channels when the appropriate branch metric is used. Hamming Distance is used as the primary partition factor.
- A new 16-subset partition for Fading channels, to be used with a convolutional encoder of rate 3/4 and $\nu = 4$. No simulations have ben run with this partition.

7.2 Original Partition into 8 Subsets (Partition 1 or A)

As mentioned earlier, this partition –optimal in AWGN– was detailed in [21] and will not be described in detail here. Following Ungerboeck's [37] partitioning rules, with necessary modifications for multi-dimensional constellations which are not Cartesian products of the constituent 2D constellations [31], the 8192-point 16D CEQ^{2}PSK points, $\{V_i\}$, $i = 1, \cdots, 8192$, are partitioned into 8 subsets, denoted $\{A_i\}$ and $\{B_i\}$, $i = 1, \cdots, 4$. Each subset contains 8192/8=1024 points. The MSED within each partition subset is 16, twice as large as the MSED of the unpartitioned constellation. This allows us to achieve an asymptotic gain of

---

[1] All our codes have d_f determined by the parallel transitions.

3 dB with just 8 subsets and a simple 8-state convolutional encoder of rate 2/3. To achieve larger gains, further partitioning is needed, along with a trellis with more states. Refer to the Appendix D for code that generates the 8 subsets (denoted by E_0-E_7 in the code).

7.3 Partition into 8 Subsets for Fadig Channels (Partition 2 or B)

The original subset partition mentioned in the previous Subsection and detailed in [21] is optimum in AWGN where only the Euclidean Distance (or MSED) is of interest. When dealing with fading channels, the ED becomes a secondary parameter and the Hamming Distance is the primary concern. Using a criterion which first ensures that there are as many coordinates that differ as possible within each subset and then maximizes the ED between signals within each subset, we have arrived at a second partition into 8 subsets. Each of the 8 subsets contains 1024 points. We name these sets $\{G_i\}$, $i = 0, \cdots, 7$.

Intuitively, one knows that multiplicative Rayleigh noise cannot, on its own, change the sign of the transmitted signal; therfore, if only this impairment is present in the channel, the received version of a signal in a subset cannot be received with a change of sign in any coordinate. So, for example, [1 1 1 -1] cannot be corrupted by multiplicative noise alone into [-1 -1 -1 1] or any other point with -1's in the coordinates where 1's were present in the transmitted signal or 1 where -1's were transmitted. The same applies to $-\sqrt{2}$ vs. 1 and $\sqrt{2}$. In high SNR (Gaussian noise) situations, then, it is fine to have signals inside a subset even if they are close in ED, as long as they are far in HD (large number of coordinates that differ). The weighted measure shown in (2.3) can be used to obtain appropriate partitions. The lower the SNR, the higher the ED should be weighted, and vice-versa.

7.4 Partition into 16 Subsets

The partition into 16 subsets achieves an intra-subset symbol Hamming distance of 4 (i.e, four coordinates differ between any two points in the same subset. Within the subsets, unfortunately, the squared Euclidean distance remains at 8, as it is before the partition.

The partition process starts with the four dimensional constituent constellations (Saha's $\{S_i\}$ and Cartwright's $\{C_i\}$). A total of 8 groups of two 4D points each, four from each, are formed so as to mazimimeze the Hamming distance between the points inside each group. We denote the 4 groups from Saha's $\{Q_i\}$ and the 4 from Cartwright's $\{QR_i\}$, $i = 1, \cdots, 4$ (using R for 'rotated'). All these 8 groups have HD of 4 but the SED in Saha's is 16 while the SED in Cartwright's is 8. Next, we generate the 8D types by performing the cartesian products $Q_i \times Q_j$ and $QR_i \times QR_j$, $i, j = 1, \cdots, 4$, yielding 16 types Q_{ij} and 16 types QR_{ij} with 8 points in each 8D type.

Now, we create 8D groups named $\mathrm{W}_i, i = 1, \cdots, 4$, each with 16 8D points inside and $\mathrm{WR}_j, i = 1, \cdots, 8$, each with only 8 points inside. We do this by grouping four Q_{ij} together or two QR_{ij} together while ensuring we keep the HD at 4 in each case.

We now generate groups of 16D signals by performing the cartesian product of $\mathrm{W}_i \times W_k$, for $i, k = 1, \cdots, 4$ for a total of 16 groups of 256 16D points (of Saha's type); we will refer to these sets as $\mathrm{W}_{ik}, i, k = 1, \cdots, 4$. For the rotated points, we do the cartesian product of $\mathrm{WR}_j \times WR_m$ for $j, m = 1, \cdots, 8$ for a total of 64 groups of 64 16D points, $\mathrm{WR}_{jm}, j, m = 1, \cdots, 8$. The minimum HD in 16D is still 4 for all these subsets. We now join, through union, four of these 64 together, and we do this 4 times ensuring that the minimum HD is still 4. We denote these 16 groups of Cartwright's type of points by $\mathrm{G}_p, p = 1, \cdots, 16$.

Finally, to arrive at the final 16 subsets to be assigned to the trellis partitions for the rate 3/4 convolutional encoder, we join, again through the union operation, one subset from Saha's W_{ik} and one from Cartwright's G_p. Each of the final 16 subsets, which we denote $F_p, p = 1, \cdots, 16$, has 512 16D points (half of them have coordinates ± 1 and half of them have coordinates of the type $0, \pm\sqrt{2}$ or $\pm\sqrt{2}, 0$). The subsets are generated by the code in Appendix G.

Remember that the minimum HD within the partitioned sets is 4, four times as large as the minimum HD of the expanded CEQ^{2}PSK constellation. However, this is 2 times the HD of Saha's 16D constellation and 4 times that of Cartwright's 16D constellation.

7.5 Other Partitions

In [43], the authors propose a partitioning method based on Wei's [39] original AWGN method. They construct 4D and 6D trellis codes with rectangular constellations, by partitioning the constituent 2D constellations. Partition is both into subsets with enlarged MSED and also subrings with equal energy points. The minimum HD of their signal points equals N for the 2N-D constellations. This might be a better way to attempt to partition our constellation; we leave this for future research.

Chapter 8 Trellis Coded Modulated 16D CEQ^{2}PSK for Fading Channel

8.1 TCM encoder

Our multidimensional TCM systems use feedback convolutional encoders from [37] and [39]. The first has rate 2/3 and constraint length $\nu = 3$ and is shown in Fig. 8.1; this is used with either of the two partitions into 8 subsets (i.e., partitions 1 or 2). The second convolutional encoder is of rate 3/4, constraint length $\nu = 4$, and is shown in Fig. 8.2. The corresponding trellis diagrams are shown in Figs. 8.3 and 8.4, respectively. Remember that our TCM system has a CEQ^{2}PSK modulator over four consecutive modulation time intervals, each of duration 2T, for a total symbol duration of 8T. This is indicated in the memory boxes of the convolutional encoders depicted. For the subset assignment to the trellis, we only show the assignment for Partition A shown in Fig. 8.3. The assignment for Partition B is similar, with A_1 through A_4 replaced by F_0 through F_3 and B_1 through B_4 replaced by F_4 through F_7.

Fig. 8.5 depicts the complete 16-D CEQ^{2}PSK-TCM system for the encoder with 8 states. Referring to Fig 8.5, we see that two of the 12 bits of information, (b_{10}, b_{11}), arriving every four signaling intervals enter the convolutional encoder to produce three coded bits (z_0, z_1, z_2). The output of the convolutional encoder selects one of the eight subsets $\{A_i\}$ and $\{B_i\}$, $i = 1, \cdots, 4$ or one of the subsets $\{G_i\}$, $i = 1, \cdots, 8$. Two other uncoded bits (b_8, b_9) select

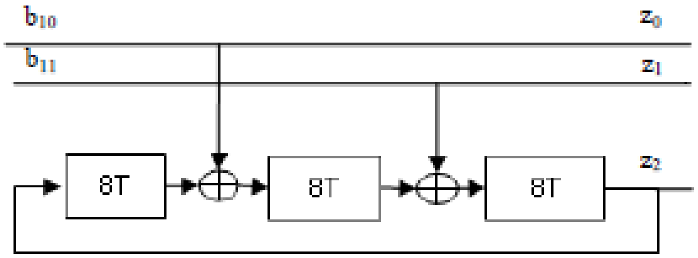

Figure 8.1: Convolutional Encoder of rate 2/3 and $\nu = 3$ to be used with an 8-subset partition.

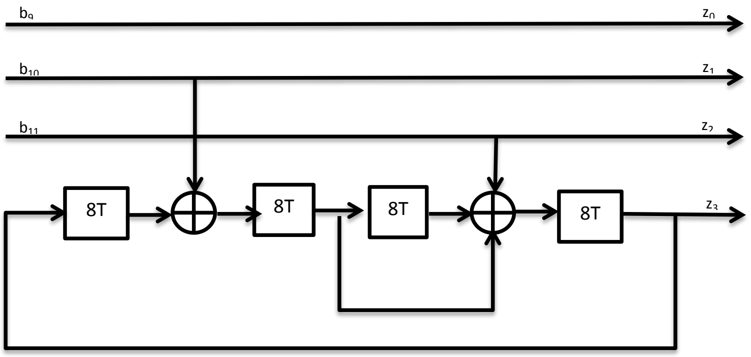

Figure 8.2: Convolutional Encoder of rate 3/4 and $\nu = 4$ used with the 16-subset partition.

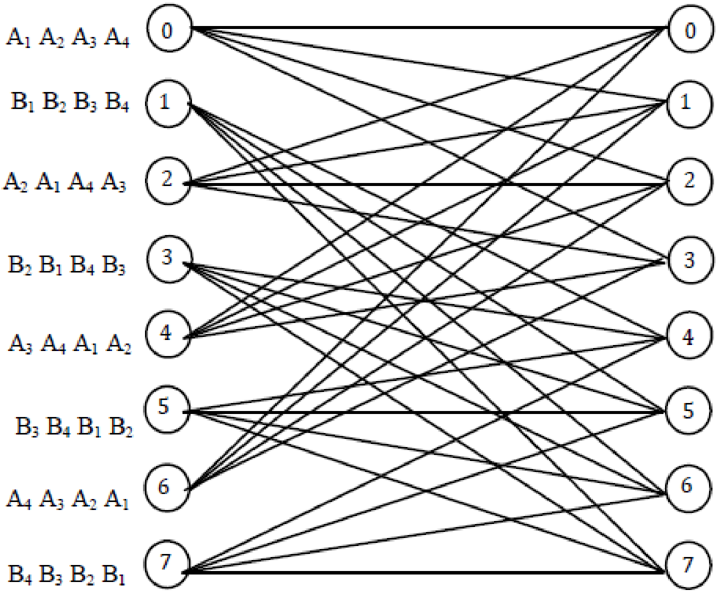

Figure 8.3: Trellis diagram for the rate 2/3 covolutional encoder.

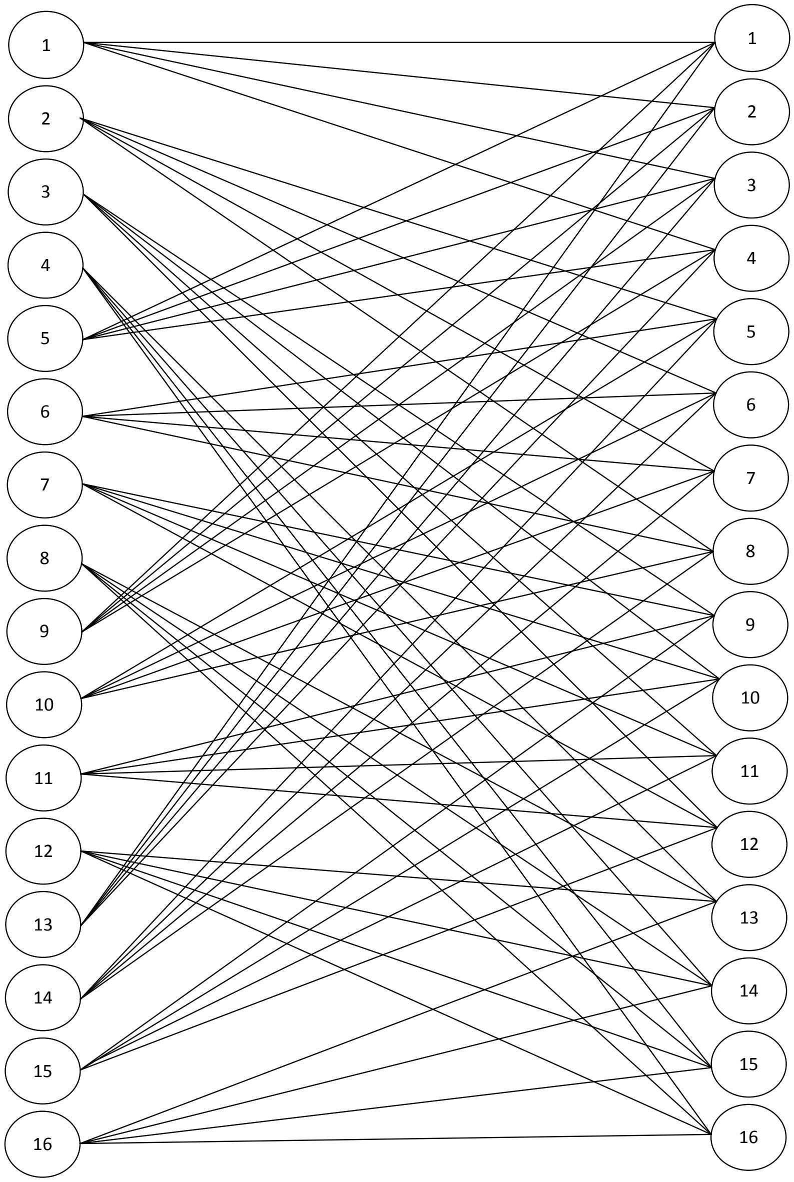

Figure 8.4: Trellis diagram for the rate 3/4 covolutional encoder.

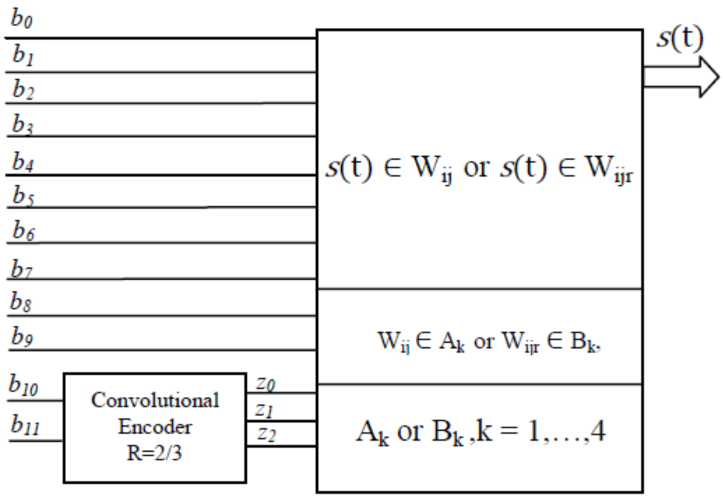

Figure 8.5: Complete TCM encoder system using a convolutional encoder of rate 2/3.

one of the types (W_{ij} or WR_{ij}) from within the selected group [21]. Finally, the rest of the information bits (b_0 through b_7) select one of the 256 points from within the selected 16-D Types. The signal *s(t)* corresponding to the 16D point selected is transmitted.

8.2 TCM Decoder

In our TCM system, the received signals corrupted by noise are decoded by using a soft-decision maximum-likelihood sequence decoder [28, 38], although we also tested the sub-optimum hard detector where each coordinate of the received signal is hard limitted before being used in the decoder (i.e., before computing the branch metric).

We use the Viterbi decoding algorithm [61, 62] to search the trellis and find the most likely path, given the received sequence of subsets. The trellis is shown in Fig. 8.3 with the subset assignment given in the usual top-down fashion. Because the first convolutional encoder has a constraint length of 3 and rate 2/3, and the second has $\nu = 4$ and rate 3/4, a decoding depth of 24 (i.e., 8ν or 6ν, respectively, for the rate-2/3 and rate 3/4 encoders was used in the decoder implementation [62]. According to Forney [26], about 5.4 ν is sufficient as decoding depth.

The mapping from input symbols to output bits is performed as follows: First, the VA estimates the most likely of the state transitions and the corresponding subset for that transition after 24 16D intervals of modulation; therefore, by using the state transitions and the subset, the two information bits (b_{10}, b_{11}) can be decoded. Finally, the other 10 bits are obtained by using a look-up table of 1024 rows, corresponding to the 1024 symbols in the estimated subset.

Chapter 9 Results: Probability of Error for Fading Channel

We divide this Chapter into several parts, all detailing results of our 16D CEQ^{2}PSK TCM system performance in various scenarions, in several different channels, and with different quantities as parameters. Discussion in this Chapter relates to probability of error (or bit error rate, BER) vs. signal-to-noise ratio (SNR) simulation results.

The simulation parameters for all cases discussed and presented in this Report are given in Table 9.1. It details the channel parameters, the number of errors counted, and the number of simulations per point.

Table 9.1: Simulation Parameters

Channel	No. Simulations per point	No. Errors per point	Comments
AWGN	1	20	Standard AWGN determined by E_b/N_o
Rayleigh Slow Fading	500	20	Doppler of 10 flat fading Sampling at 1/512 Hz
Raleigh Fast Fading	1	20	80 KHz Jakes and flat fading
UHF LOS # 1	500	100	Detailed in [11] Sampling at 1/512 Hz

9.1 Distance Properties and Expected Coding Gains

Table 9.2 lists the smallest 12 squared Euclidian distances (SED) of the expanded CEQ^{2}PSK constellation. The column labeled d_k^2 represents the SED, and the values in the column named $N(d_k)$ are the number of points at SED d_k^2. The MSED for the uncoded constellation (CEQ^{2}PSK) is $d_u^2 = 8$, and has $N_u = 24$ points at that distance. The free distance of our simple TCM system is given by the parallel transitions in the trellis. For Parition 1, the coded squared Euclidean distance is $d_c^2 = 16$ with an error coefficient (in 16D) of $N_c = 76$. These values determine the asymptotic gain of the coded system [28,37,38]:

$$G_a = 10\log_{10}\left(\frac{d_c^2}{d_u^2}\right), \tag{9.1}$$

which yields 3.01 dB because the squared free distance is doubled without increasing the energy over that of the uncoded system. However, we also have to take into consideration the loss caused by the number of neighbors at MSED [22,26]; this loss normalized to 2D, λ, is [35]:

$$\lambda = \frac{\log_{10}(N_c/N_u)}{\log_{10}(32)}, \tag{9.2}$$

which gives a loss of 0.33 dB for our simplest code (i.e., the system of rate 12/13 with a convolutional encoder of rate 2/3). The effective gain is therefore

$$\gamma_{eff} = G_a - \lambda = 2.67\,\text{dB}. \tag{9.3}$$

Higher gains are possible with encoders of higher rate; the achievable asymptotic gains are also listed in Table 9.2. The boldface line shows the achieved SED and gain achieved by the 8-subset partition Partition 1.

The Hamming Distance distribution becomes the primary concern in Fading Channels. This distribution is shown in Table 9.3. The boldface row shows the achieved HD obtained with the 16-subset partition.

It is known that the minimum Euclidean distance is the primary parameter (i.e., that which should be maximized) in AWGN channels. However, in fading channels, the MSED becomes less important. Divsalar and Simon proposed rules for designing TCM codes in fading situations [63]. The first optimization objective in fading channels is to maximize the diversity parameter of the code; this is really the Hamming distance of the code in terms of 2D signals. A secondary objective is to maximize the squared product of branch distances (SPD) along the paths with minimum diversity, and is therefore determined by the Euclidean distances.

Table 9.2: SED and asymptotic gains achievable in AWGN for the expanded 16D CEQ^{2}PSK TCM system.

d_k^2	$N(d_k)$	G_a (dB)
8.000	24	0
9.373	16	0.69
15.029	128	2.74
16.000	**220**	**3.01**
20.686	448	4.13
24.000	936	4.77
26.343	896	5.17
32.000	2854	6.02
37.657	896	6.73
40.000	936	6.99
43.314	448	7.34
48.000	220	7.78

Table 9.3: Hamming distance distribution of our expanded 16D CEQ^{2}PSK constellation.

HD	Number of neighbors at HD
1	8
2	24 or 28
3	56
4	**86** or **220**
5	152
6	268 or 938
7	328
8	337 or 1734
9	480
10	592 or 936
11	384
12	220 or 352
13	512
14	24 or 256
15	0
16	4097 or 4352

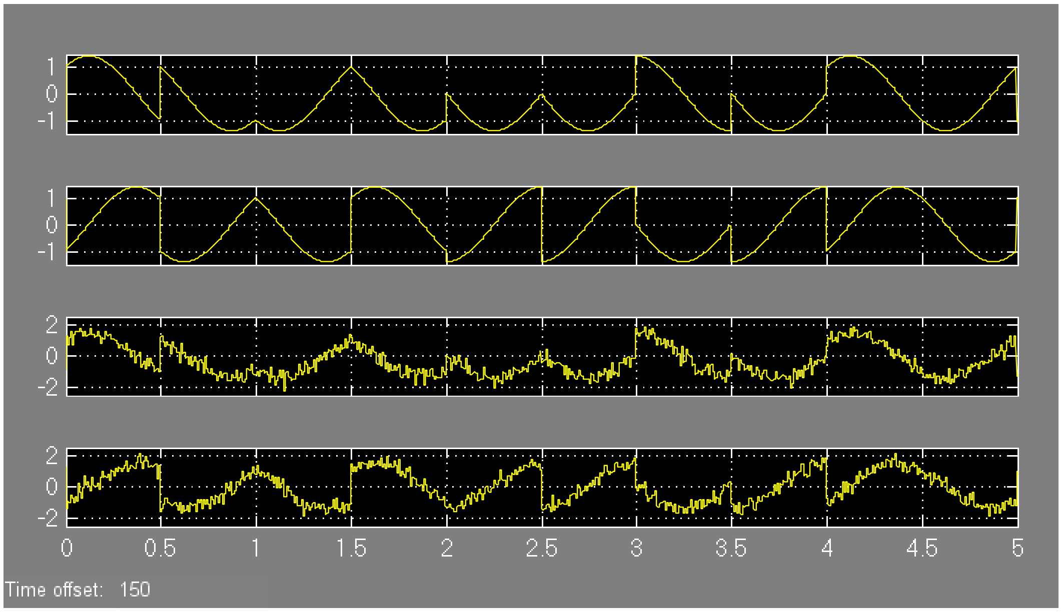

Figure 9.1: Baseband in-phase and quadrature-phase CEQ^{2}PSK signals at the transmitter and receiver when AWGN is present.

The effective diversity order for a two-sequence test is equivalent to the symbol Hamming distance. Diversity order is the effective number of independent propagation channels obtained in time, frequency, or space diversity transmission systems and this number represents the slope of the error probability versus SNR on a log-log display [64].

9.2 TCM System Simulation Results in AWGN

We first show plots of the baseband versions of the in-phase (I) and Quadrature-phase (Q) components of the CEQ^{2}PSK signals at the transmitter and at the receiver, after WGN has been added. These are shown in Fig. 9.1 where the first and third plot represent the In-phase transmitted and received signals, respectively, while the second and bottom plot shows the quadrature phase components. The horizontal scale is in seconds, and the symbol rate is 0.5 s. The SNR for the noisy plots shown is 25 dB. The corresponding passband signals are depicted in Fig. 9.2.

The performance of our implementation of our multidimensional TCM CEQ^{2}PSK system was corroborated by using Monte Carlo Simulations in the simplest channel first: Additive White

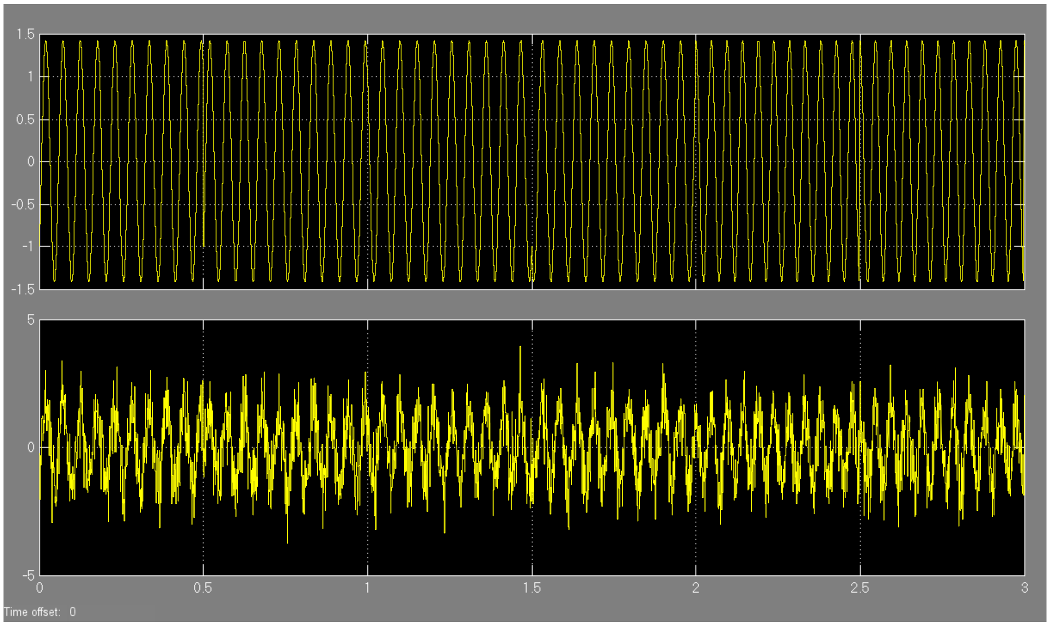

Figure 9.2: Passband CEQ^{2}PSK signal at the transmitter and receiver when AWGN is present.

Gaussian Noise (AWGN). A total of at least 20 errors are counted before the simulation stops, at which time the probability of error is computed. We first made sure that our receiver works for both Saha's and Carwright's 4D constellations (Saha's with coordinates ± 1 and Cartwright's with coordinates $(0, \pm\sqrt{2})$ or $(\pm\sqrt{2}, 0)$). These results are shown in Fig. 9.3 and were obtained with the implementation of the optimum hardware detectors for each of the two constellations. We re-ran the simulations with the newer implementation of the detectors (which do not directly implement the hardware detectors) and obtained the same results.

The two almost overlapping plots in Fig. 9.3 corrobarate that the receiver functions as expected. In Fig. 9.3 we show the BER of the system in AWGN alone. The small discrepancies, barely visible, are due to the randomness and could be further decreased by counting more than 20 errors before stopping the simulation and computing the BER.

Fig. 9.4 shows the results in terms of bit and symbol error probabilities versus signal to noise ratio (SNR) for the reference uncoded 16D CEQ^{2}PSK and the trellis-coded 16D system that uses the expanded CEQ^{2}PSK constellation and decoding depth of 24. Comparison of the

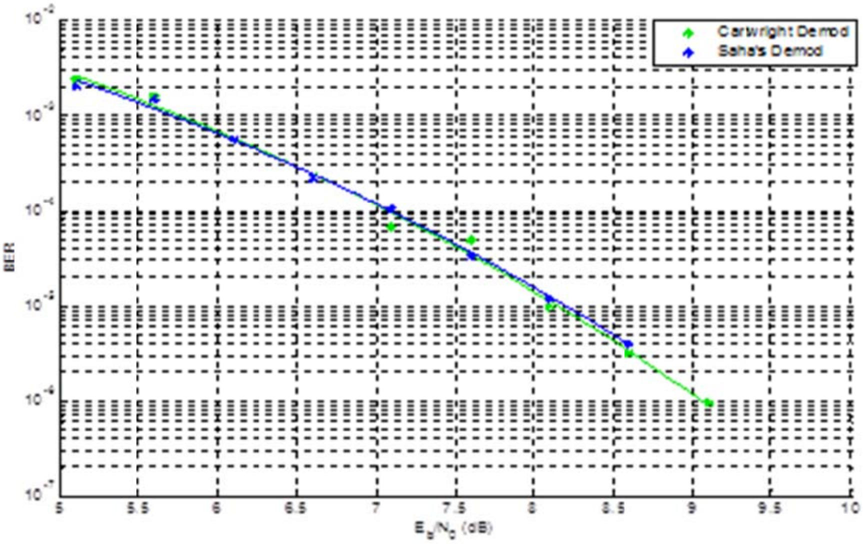

Figure 9.3: Probability of bit error vs. SNR in AWGN channels for the 4D CEQ^{2}PSK constellations $\{S_i\}$ and $\{C_i\}$.

curves corresponding to the coded and uncoded probabilities of symbol error indicates that the effective gain of 2.67 is not yet achieved at a SNR of slightly over 8 dB; the gain, however, increases with increasing SNR, and also with increasing decoding depth. The gain in bit error rate (BER) is slightly less because it cannot be guaranteed that a single bit is in error if a symbol is in error; as SNR increases, the likelihood of a single bit error per symbol error increases, so the bit and symbol probability of error curves tend to merge at large SNR.

We tested the (sub-optimum) hard decoding Viterbi Decoder as well as the soft-decision VA implementations. Results for the 4D and 16D systems are shown in Fig. 9.5. We see that the performance using the hard decision detector is considerably worse than when soft decisions are made. The soft decision encoded system's performance shows a gain for all SNRs, and the gain increases with increasing SNR. The achieved gain at 6.5 dB is about 1.4 dB while at 7.5 dB the gain is about 1.9 dB and at slightly over 8dB the gain has increased to about 2.7 dB. The hard-decision detector tested, however, was not implemented correctly because in addition to hard-limitting each of the 16 coordinates received, a decision was actually made as to the transmitted point for that particular branch and when the cummulative metric was computed this erroneous partial branch metric was used. The actual performance of a

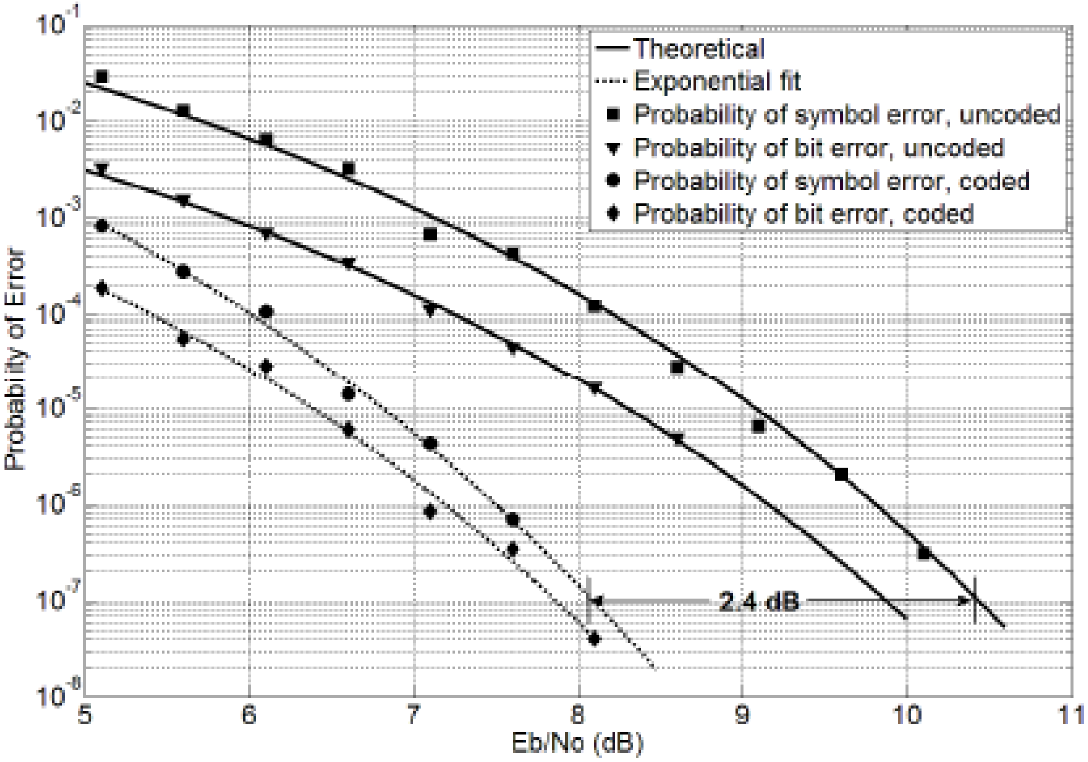

Figure 9.4: Probability of symbol and bit error vs. SNR in AWGN channels for the 16D CEQ^{2}PSK systems with and without trellis encoding.

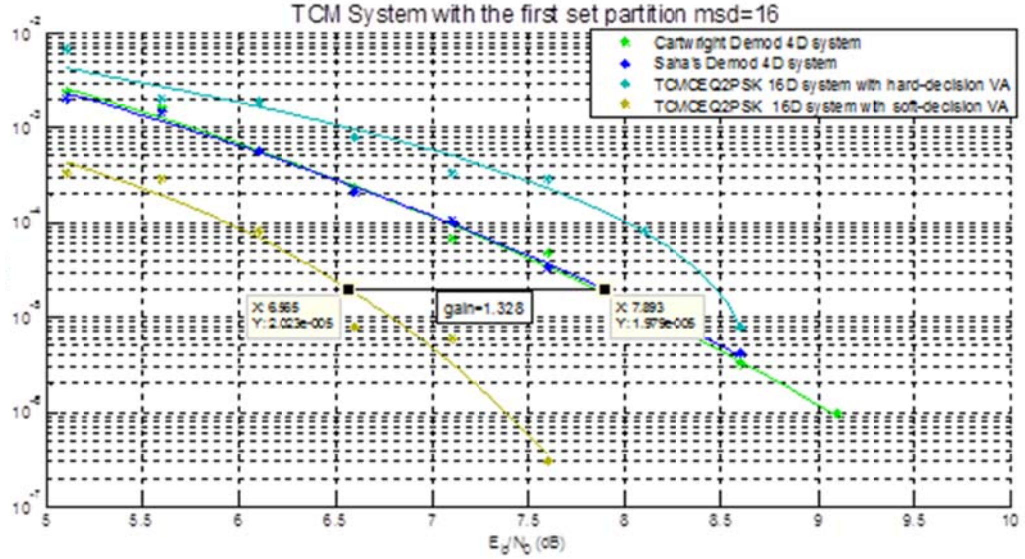

Figure 9.5: Probability of error vs. SNR in AWGN channels using Hard- and Soft-decisions in the Viterbi decoder.

correctly implemented hard-decision decoder would not be so poor. We abandoned pursuing this avenue of investigation until we work on a hardware implementation of the receiver at which time hard decisions will be likely. For software simulations, there is no real advantage in using a hard detector. We have included these results only for completeness.

We also evaluated the effect of sampling rate on the performance. Ideally, any rate above the Nyquist rate will perform well; we know that in reality this isn't the case due to the various filtering operations that are performed directly (the integrator in the correlator receiver, a first order LPF) or indirectly (such as Matlab's own filtering to twice the sampling frequency whenever sampling is performed). These results are shown in Fig. 9.6 for a few of the baseband sampling rates tested.

As expected, the higher sampling rate produces somewhat better results at the expense of longer simulation times and increased storage requirements (because more samples per symbol must be stored and processed). The difference, however, is not significant.

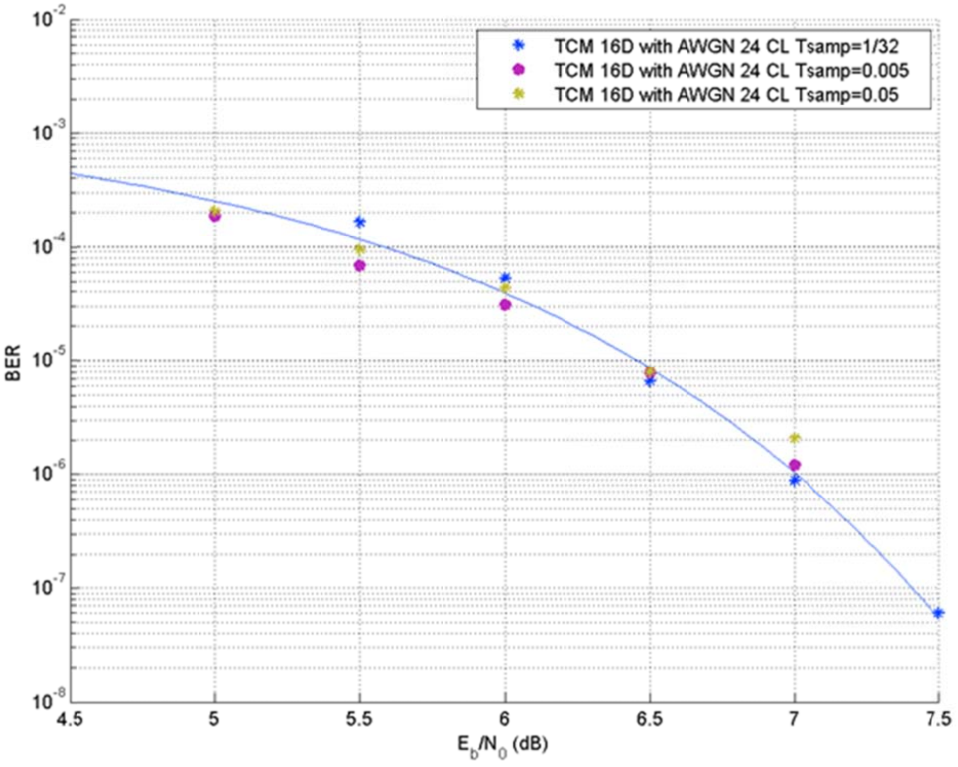

Figure 9.6: Probability of error vs. SNR in AWGN channels using different (baseband) sampling rates for a symbol length of 0.5 s.

9.3 TCM System Simulation Results in simple Rayleigh Fading Channel

In Rayleigh fading channels, the envelope of the transmitted signal is multiplied by a sample from a random process with a Rayleigh distribution. Clearly, when this random quantity multiplies the signal, it may reduce (or increase) it drastically, but it may never on its own change the plarity of any coordinate. In the worst case, a coordinate may become 0. We performed simulations on Rayleigh Fading for both Saha's and Cartwright's constellations and we have the same performance with the sub-optimum (in fading channels) distance measure used (SED). When a better metric, i.e., one that first detects change in coordinates (as Hamming distance does), followed by SED, the performance of Saha's constellation is expected to be superior to the performance of Cartwright's constellation. We leave this for another phase of this reasearch.

To see the effect of fading, we present some graphical depictions in Fig. 9.7. The top two plots in Fig. 9.7 show the I and Q components of the transmitted signal; the two waveforms in the middle are these I & Q components after the signals go through the UHF LOS#1 channel. We chose the horizontal axis of the display to clearly show a severe fading event affecting the amplitude of the signals. The signals at the baseband receiver are the latter two with the addition of AWGN and are shown in the bottom two plots.

We note that no interleaver was used in our simulations; this means that fading events affect many bits (and many symbols) consecutively. furthermore, the fading in the I and Q components are not uncorrelated. Decorrelation may be performed through the use of interleavers as well.

Finally, we also evaluated the effect of various models (the spectrum filter or spectral shape) of the Rayleigh fading. We show results with flat and Jakes Rayleigh fading channels for both 8-point partitions. Partition 1 (or A) is optimum in AWGN while partition 2 (or B) should perform better in fading channels when the appropriate branch metric is used. The performance in AWGN without fading is also shown as a baseline. The sampling rate (baseband) is 1/512 Hz. These results are shown in Fig. 9.8.

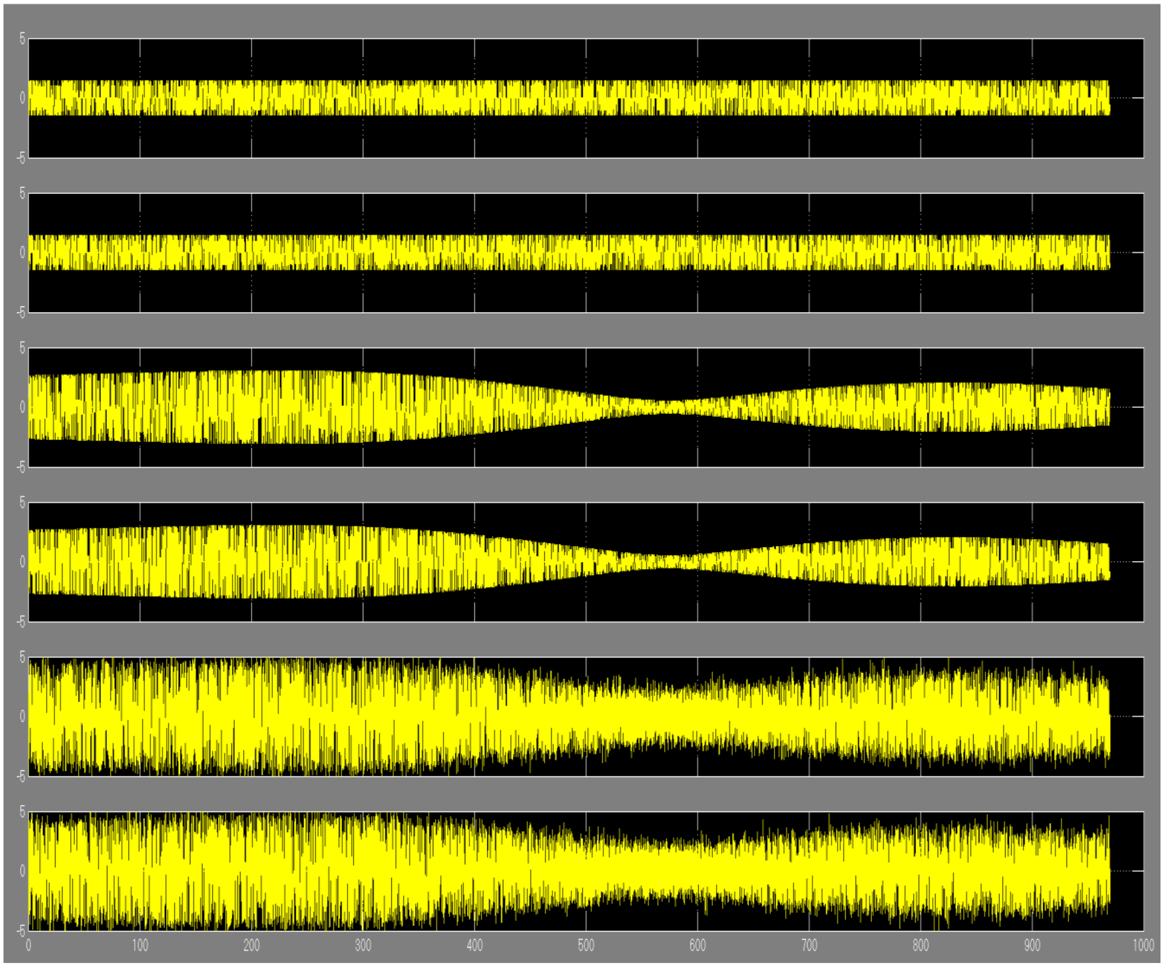

Figure 9.7: Waveforms for our CEQ^{2}PSK system in Rician fading channel UHF LOS #1. The waveform on the top are the clean I and Q components of the CEQ^{2}PSK baseband signal; the middle waveforms are the faded I/Q waveforms, and the bottom signals are the received I/Q signals (faded with AWGN)

.

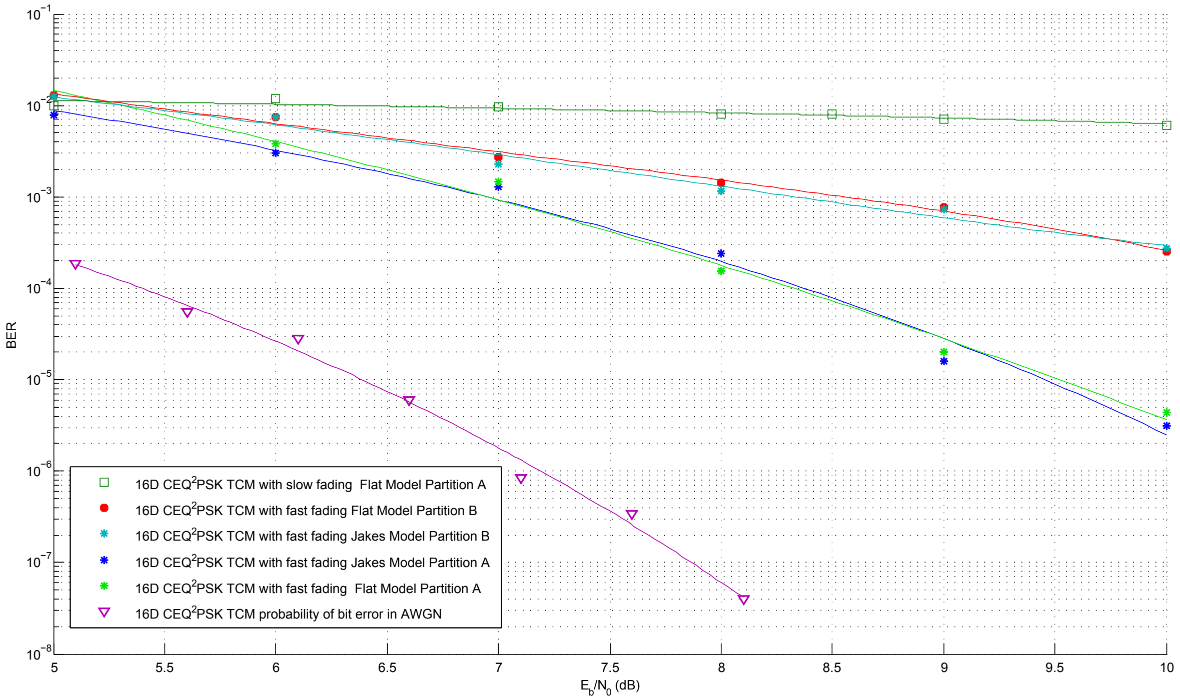

Figure 9.8: Probability of error vs. SNR in flat and Jakes Rayleigh fading channels using two different 8-subset partitions for fast and slow fading.

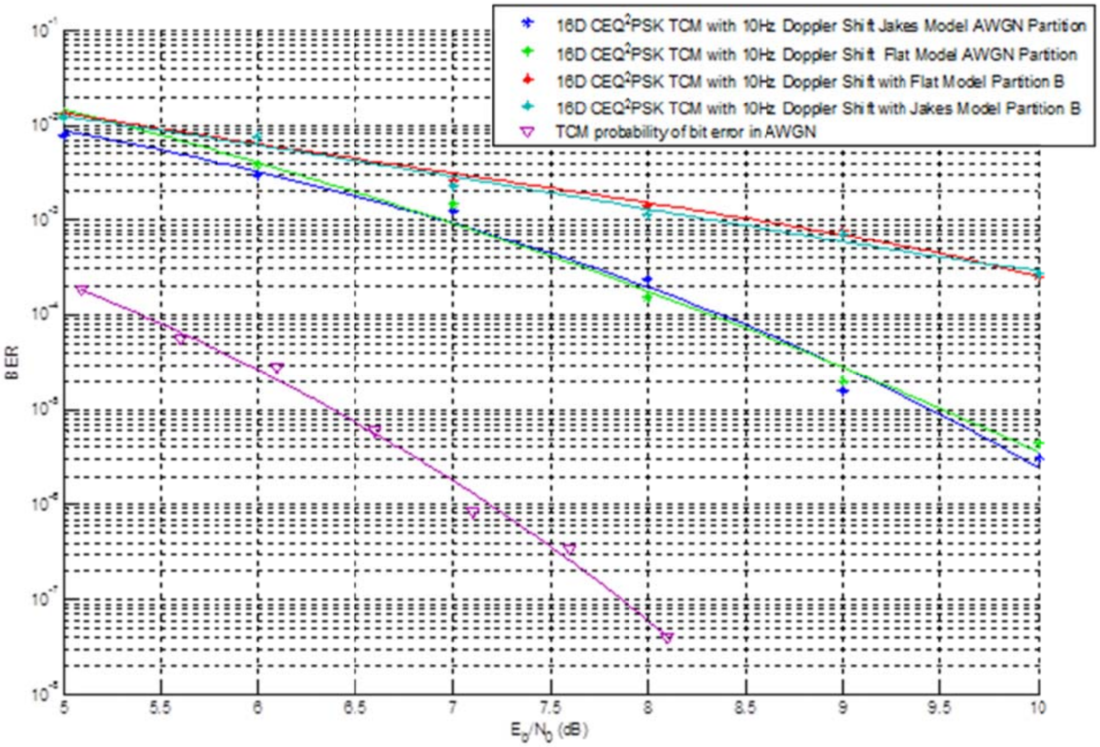

Figure 9.9: Probability of error vs. SNR with flat fading of two different rates.

9.4 TCM System Simulation Results in UHF LOS Channel # 1

Simulation results for the fading channel #1, a single line-of-sight Rician channel with a single Rayleigh diffuse component are shown on Fig. 9.10. Generation of this figure (or similar) is very time consuming. With Rician and Rayleigh rays we have enormous randomness in the resulting probability of error. In order to try to obtain meaninful results, we averaged over 500 realizations of the fading for each realization of SNR; for each of the latter, we counted 100 errors.

For the UHF LOS #1 channel, in order to achieve a BER of 10^{-3}, the SNR must be about 25dB, on the average, but there is large variability.

To see the wide range of results obtained for a given fading channel, refer to Fig. 9.11 where the 455 values of the BER (counting 100 errors each time) are shown for a SNR of 31 dB. To obtain the average BER for these, we do not average the BER over the 500; instead, we add the total number of errors (which is not necessarily exactly 100 because we only stop with integer number of symbols or 13 transmitted encoded bits) and divide that sum by the sum of of the number of transmitted bits. This average used is also shown (as the red line) in Fig. 9.11, while simply averaging the obtained PE for each realization is shown in green.

We also show, in Fig. 9.12, the histogram of the 455 values of probability of error obtained for SNR = 31 dB. Notice that the BER axis is given in logarithmic scale. The statistics for thes 455 realizations are shown in Table 9.4. Clearly, ther is a wide range of values among realizaitons for the BER obtained.

The results presented in Fig. 9.10 are expected to improve if an interleaver/deinterleaver pair are used in the transmitter/receiver. These results were obtained without interleaving and therefore fading events are likely to cause many consecutive errors.

Table 9.4: Statistics of BER obtained for 455 realizations of the channel UHF LOS #1.

BER Statistic	Value
Average of BERs	$4.284E^{-4}$
BER average	$2.795E^{-4}$
Variance	$4.091E^{-7}$
Mode	$1.612E^{-4}$
Median	$3.055E^{-4}$
Minimum	$7.842E^{-5}$
Maximum	$9.000E^{-3}$

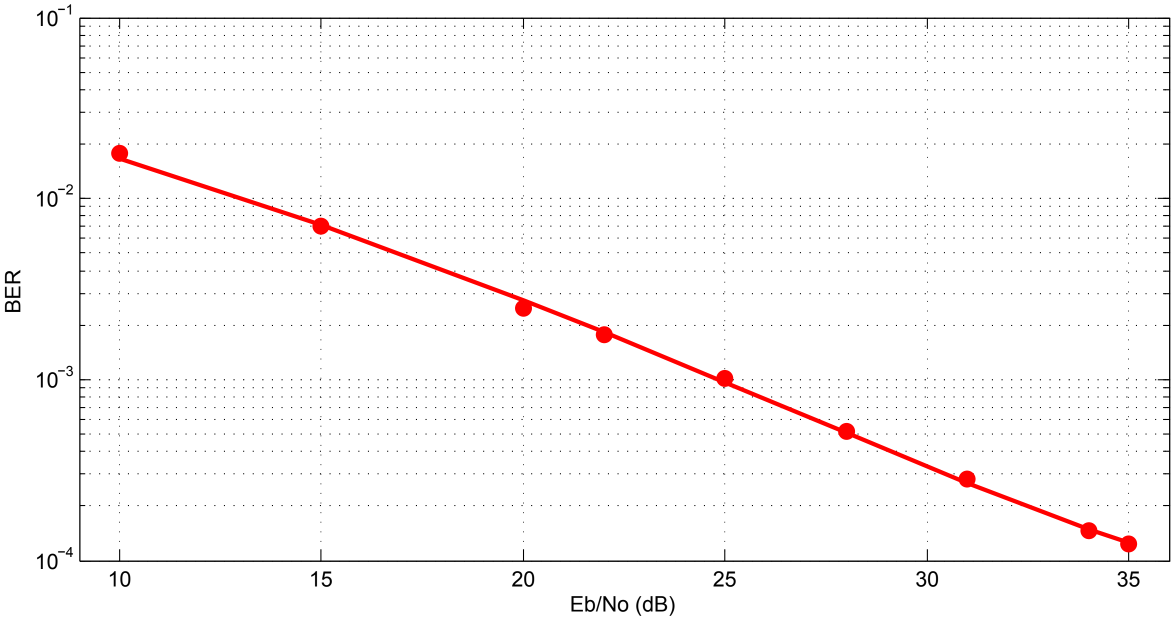

Figure 9.10: BER simulation results in the fading Rician channel UHF LOS # 1.

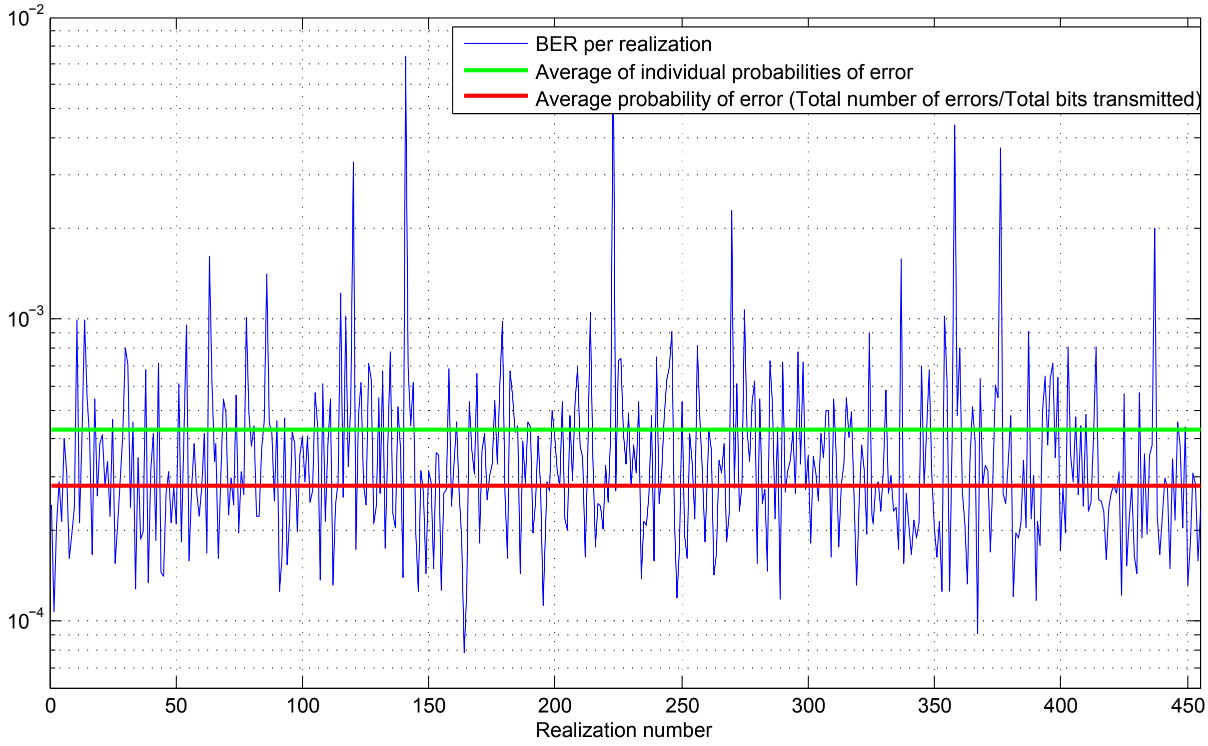

Figure 9.11: Results for 500 realizations of the Rician channel UHF LOS # 1. We show the individual 500 BER, the average of the individual BER, and the average BER as the total number of errors over all realizations over the total number of bits transmitted for SNR = 31 dB.

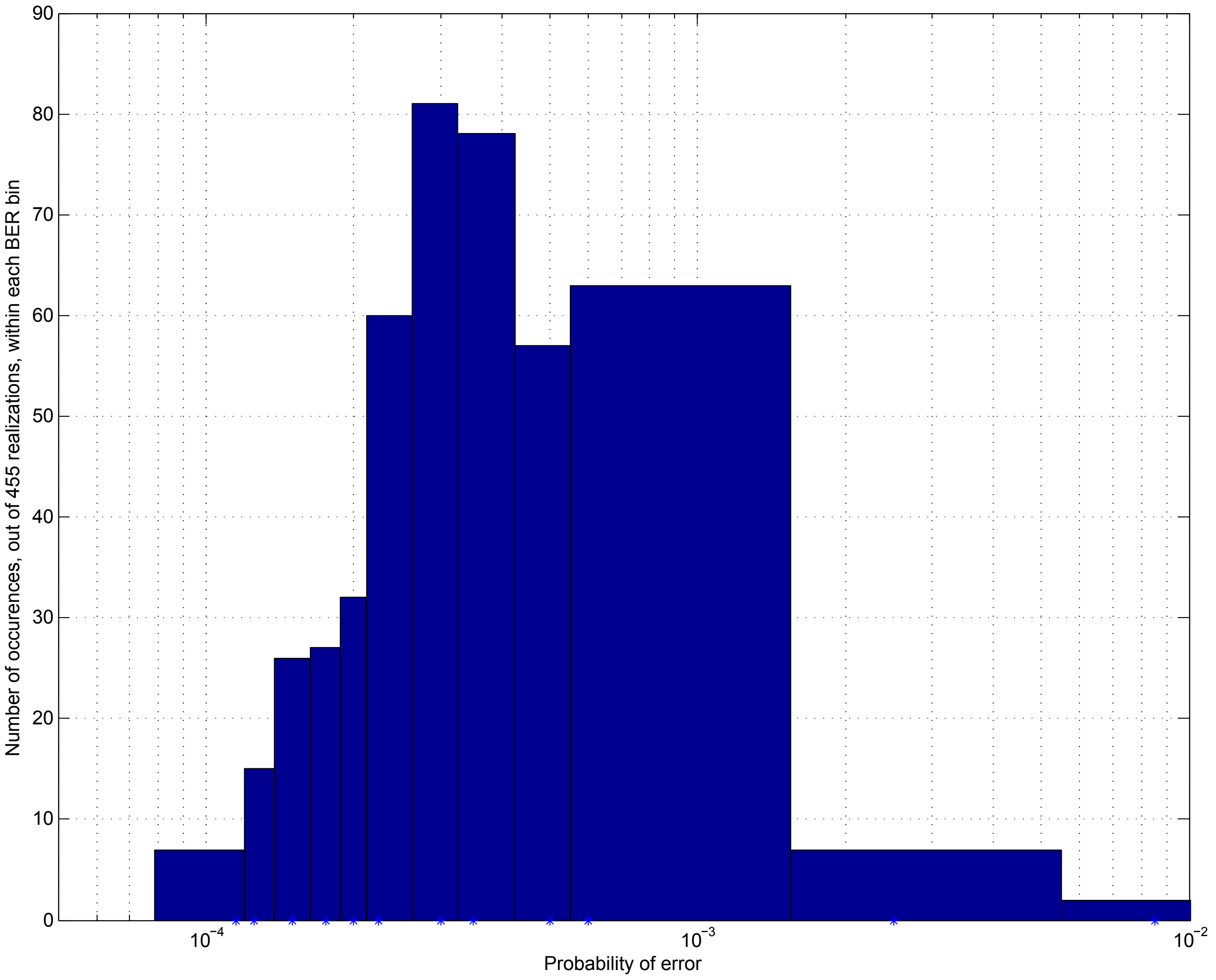

Figure 9.12: Histogram

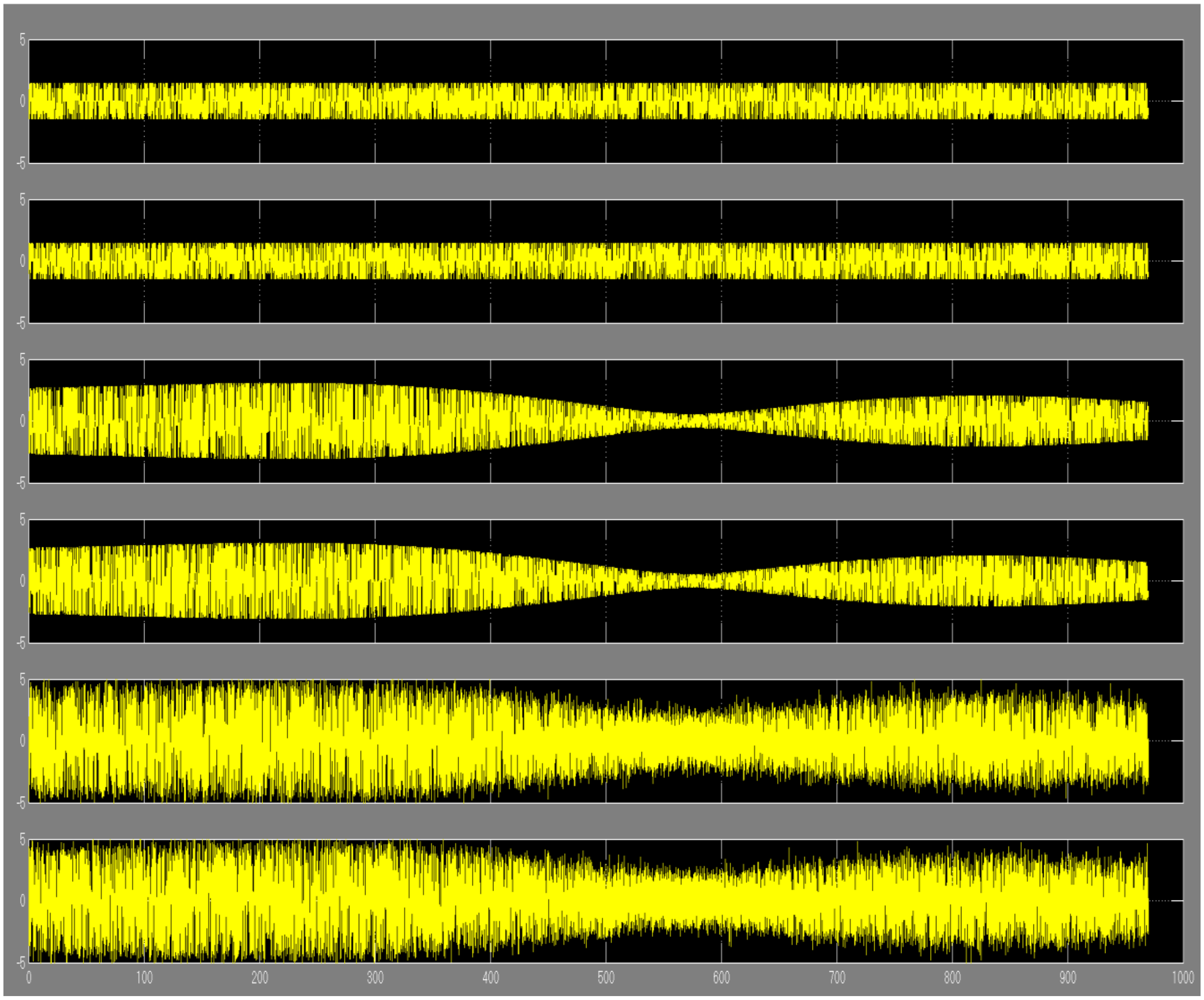

Figure 9.13: Waveforms for our CEQ^{2}PSK system in Rayleigh Fading. The waveform on the top is the clean CEQ^{2}PSK signal; the middle waveform is the faded waveform, and the bottom signal is the received signal (faded with AWGN).

9.5 BER Performance Summary and Comparisons

Evaluation and comparison of different schemes in AWGN is always easy. The AWGN performance is very often given as a baseline, and all researchers use identical or very similar definitions of signal-to-noise ratio (SNR), and provide similar plots. The Gaussian pdf is completely determined by the mean, μ (zero in all our simulations), and the variance per channel, σ^2 or, equivalently, the PSD $N_o/2$ (single sided). Furthermore, there are excellent approximations (usually through the union bound) for theoretical evaluation of performance of communication systems in AWGN.

Unfortunately, when it comes to Fading channels, different researchers or authors use a wide range of parameter values, or descriptors for the relevant quantities depending on the physical conditions they are simulating. In the simplest fading case, where Rayleigh fading is assumed, often the Rayleigh parameter (e.g., the parameter b in (2.5) which describes the distribution of the amplitude envelope of the process) is provided and used as a parameter, and then the AWGN SNR is used to obtain the performance plots. Other authors, however, state the maximum Doppler frequency instead. The maximum Doppler frequency, f_d, must be compared to the actual bit or symbol rate, so that 100 Hz, for example, may be fast for a given system while slow for others. Some authors unfortunately do not list any parameters or give incomplete lists so the actual situation is really undetermined.

In the cases of practical fading where both Rician and Rayleigh components are present, the variety of parameters, values, and presentations varies even more. In many instances, it is completely unclear what cases are depicted in plots given; this makes performance comparisons among systems very difficult. To add to the problem, encoders of various types, rates, and memory, as well as different decoding depths are used, and no single combined measure is available or in common use to simply characterize coded systems [31].

Nonetheless, we have compiled just a few of the many results available in the open literature, to compare to our system in Rician fading channels. We have developed two tables which are used together to summarize the systems: Tables 9.5 and 9.6. The former shows, when available, the system and its characteristics, along with the bibliographic reference where the material appears. Table 9.6 lists, for each of the entries in Table 9.5, the probability of error for 6 values of SNR between 10 and 35 dB,if available. We use the first author's last name and a letter if several systems or modes are presented by that author. For our systems, we only list the rate 2/3 encoder with Partition A (or partition 1 into 8 subsets), namely Kaminsky A.

Table 9.5: Description of various schemes to be used for comparison.

System Label	System Description	Parameters	Reference
Ravi D	R=3/4 8-state, 16PSK $\nu = 3$, 2D	N/A, Rician	[42]
Ravi A	R=2/3 4-state, 8PSK $\nu = 2$, 2D	N/A, Rician	[42]
Moose C	Diversity =1 RS(225,205), $\nu = 7$ R=1/2, DQPSK	UHF LOS #1	[11]
Kaminsky A	R=2/3 8-state 16D CEQ^{2}PSK, $\nu = 3$	UHF LOS #1	Here

Refering to Table 9.6, we see that for very low SNRs our system, Kaminsky A, is only worse than Ravi's A system, and versy similar –if somewhat better– than the others. For medium SNRs, around 20 dB, the performance of our system is worse as expected because, as stated before, our metric is still solely based on Euclidean distance and not Hamming distance. For large SNR ther are very few results presented, but Ravi D's continues being better. Our system, however, is more spectrally efficient than the others. The system most similar to ours, for comparison purposes, is the system labeled Moose C;however, the constraint length of Moose C is 7 and ours is only 3. Furthermore, Moose's system also uses a Reed

Table 9.6: BER comparison of various schemes in fading channels.

	SNR					
System Label	10 dB	15 dB	20 dB	25 dB	30 dB	35 dB
Ravi D	1.8E-2	2.4E-3	5.5E-4	1.9E-4	5.0E-5	2.0E-5
Ravi A	8.0E-3	1.8E-3	3.0E-4	8.0E-5	2.0E-5	–
Moose C	2.0E-2	1.0E-2	1.5E-3	–	–	–
Kaminsky A	1.7E-2	7.1E-3	2.4E-3	9.7E-4	3.1E-4	1.2E-4

Solomon encoder along with the rate-1/2 convolutional encoder, making it a more powerful error correcting system. Moose's plot for system C shows a very limited range of SNR, so to compare our system to theirs a bit more accurately, we show the performance of these two, side-by-side, in Table 9.7.

Table 9.7: BER Comparison of Moose's C and our (Kaminsky A) systems in UHF LOS #1

SNR(dB)	Moose C	Kaminsky A
10	4.0E-2	1.6E-2
12	2.0E-2	1.5E-2
14	1.5E-2	9.0E-3
16	7.0E-3	6.0E-3
18	3.0E-3	5.0E-3
20	2.0E-3	2.4E-3

For lower values of SNR (between 10 and 16), our system performs slightly better than Moose's C. As SNR increases, Moose C starts performing better. However, we remind the reader that for high SNR our systen is expected to become worse as currently implemented because we are still using SED as the sole branch metric. When a compound or weighted metric, which uses HD as primary criterion and SED as secondary is incorporated into our simulator, the performance of the Kaminsky A system will improve when fading is the main channel imperfection (i.e. for higher values of SNR such that ED becomes less important).

Chapter 10 Computer Simulation Description

In this chapter a survey of the implemented systems using Matlab and Simulink software is presented.

10.1 Soft Decision Viterbi Decoder

The Soft Decision Viterbi Decodes consist of: Path Metric Unit (PMU), Add Compare Select Unit (ACSU), Traceback Unit. The receiver also needs the following matrices: Subset Matrix, Output Table State, Next State Matrix, and Index Past States. Each of the matrix are utilized in the units, and their purpose will be explained in the following subsections.

10.2 Subset Matrix

This matrix is defined as follows:

$$C = \begin{pmatrix} c_1^1 & c_1^2 & \cdots & c_1^n \\ c_2^1 & c_2^2 & \cdots & c_2^n \\ \vdots & \vdots & \ddots & \vdots \\ c_m^1 & c_m^2 & \cdots & c_m^n \end{pmatrix}, \tag{10.1}$$

where the subscript represents the number of points in the signal set, and the superscript is the dimensionality of the constellation. The order of the signal points are located in the subset matrix has to be similar to the subset partition. For our system, we have eight subset matrices A1,A2,A3,A4 for Saha's and B1,B2,B3,B4 for Cartwright. In simulink the constellation matrix are concatenated into a three dimensional matrix through the use of the command:

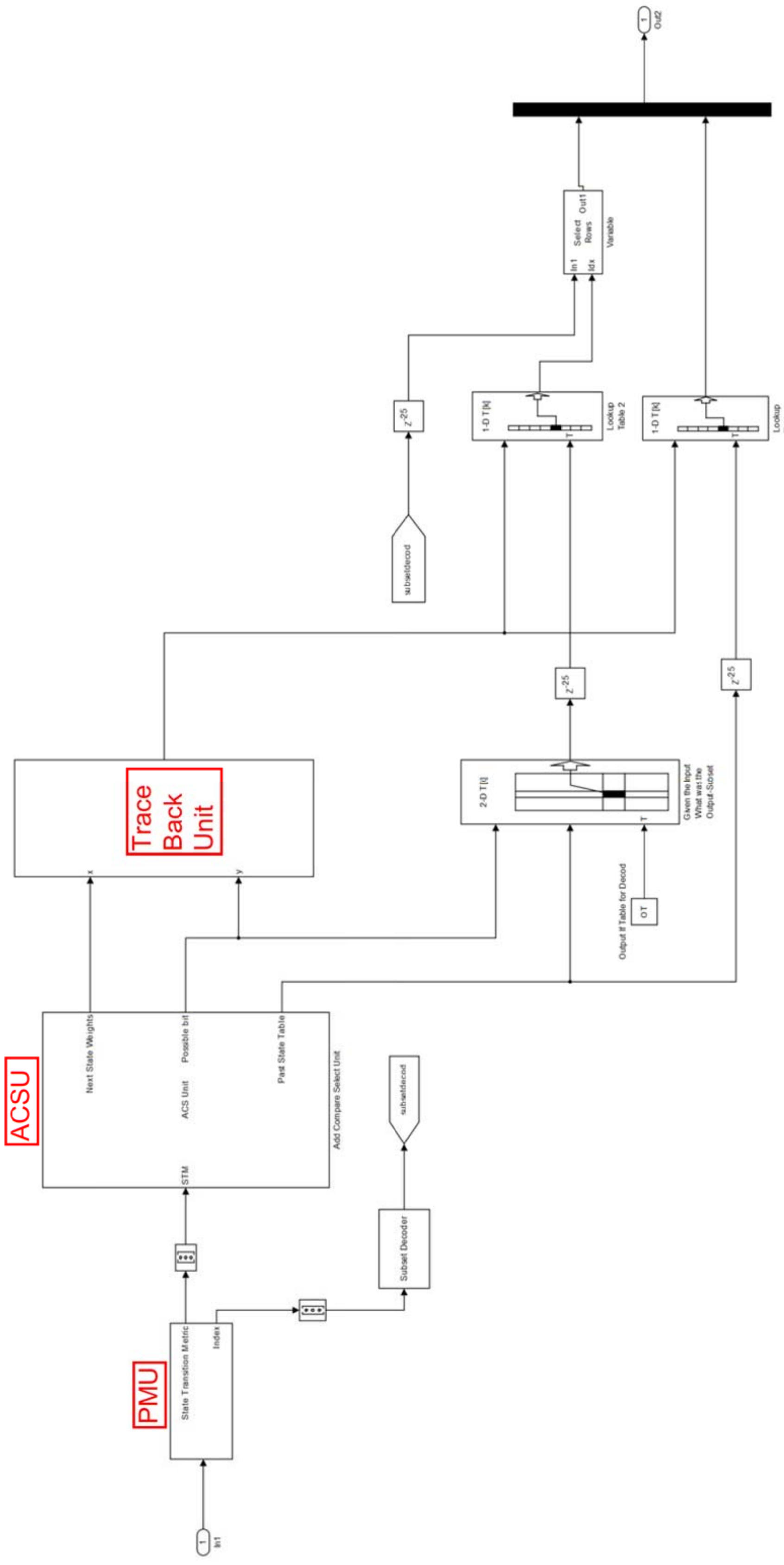

Figure 10.1: Viterbi Decoder Implementation.

Table 10.1: Subset Mapping for 16-D CEQ^{2}PSK TCM

z_2	z_1	z_0	Decimal	16-D Subset Assigned
0	0	0	0	A1
0	0	1	1	B1
0	1	0	2	A2
0	1	1	3	B2
1	0	0	4	A3
1	0	1	5	B3
1	1	0	6	A4
1	1	1	7	B4

```
cat(3,A1,B1,A2,B2,A3,B3,A4,B4).
```

Notice that the arrangement of the matrices has to follow the subset partition of the TCM system. Table 10.1 shows the partition used in the TCM and how the order match the code above.

10.3 Output Table Matrix

In order to obtain the information of the trellis, three matrices are defined: Output Table Matrix, Index Next State and Index Past State. The output table matrix is defined as follows:

$$OT = \begin{pmatrix} O_1^1 & O_1^2 & \cdots & O_1^n \\ O_2^1 & O_2^2 & \cdots & O_2^n \\ \vdots & \vdots & \ddots & \vdots \\ O_m^1 & O_m^2 & \cdots & O_m^n \end{pmatrix}, \tag{10.2}$$

where n represent the number of possible input bits in the encoder, and m represents the number of states of the encoder. The O_m^n element is the output corresponding to the n input from the m current state. The simple convolutional encoder for 16-D CEQ^{2}PSK TCM system uses two bit input encoder with three bit output, and has memory of eight possible states. The following matrix represents the output matrix used in the simulations.

$$OT = \begin{pmatrix} 0 & 2 & 4 & 6 \\ 1 & 3 & 5 & 7 \\ 0 & 2 & 4 & 6 \\ 1 & 3 & 5 & 7 \\ 0 & 2 & 4 & 6 \\ 1 & 3 & 5 & 7 \\ 0 & 2 & 4 & 6 \\ 1 & 3 & 5 & 7 \end{pmatrix}, \tag{10.3}$$

10.4 Next State Matrix

The next state matrix is a matrix where the rows represent the current state, the columns the current input, and the elements inside the matrix are all the combinations of the current state and the current input. For the encoder used in the simulation, we have the following matrix:

$$NXTA = \begin{pmatrix} 1 & 3 & 5 & 7 \\ 3 & 1 & 7 & 5 \\ 5 & 7 & 1 & 3 \\ 7 & 5 & 3 & 1 \\ 2 & 4 & 6 & 8 \\ 4 & 2 & 8 & 6 \\ 6 & 8 & 2 & 4 \\ 8 & 6 & 4 & 2 \end{pmatrix}, \tag{10.4}$$

10.5 Path Metric Unit

The Path metric unit block compute distance of the received point to all the 8192 points of the subset matrix. It determines the minimum distance to the point, and the corresponding subset that the point belongs. Figure 10.2 shows the PMU subsystem implemented in Simulink.

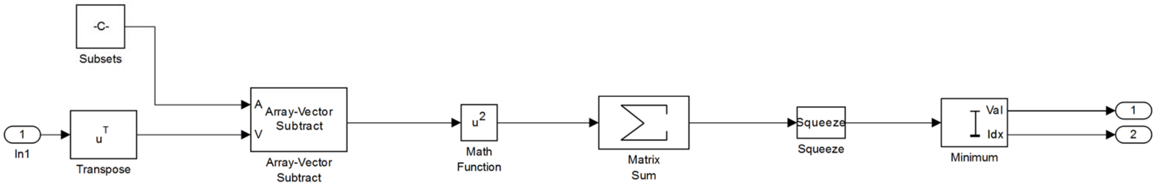

Figure 10.2: Simulink Path Metric Unit subsystem.

10.6 Add compare and select Unit

This subsystem is a sequential algorithm that accumulates the survivors of the path metric unit. This system needs the Output Table matrix, and the Next State matrix to generate three possible inputs. A weight matrix that contains the accumulated weight of the survivors, the current and possible future state input that consist of the decimal representation of the state. Figure 10.3 shows a block diagram of the implementation.

10.7 Trace Back Unit

The Trace Back Unit has two main branches of data one receives the weight matrix from the ADCSU, and the other receives possible bit vectors stores into memory block with size of the constraint length. For our simulation, we use 24 symbols in memory. After the memory is full, then shift out the first element stored to give space to the new element by the delay line block in Simulink. The Trace Back Unit block also has a Matlab function which is described below:

```
function y= TBA(Idx,path)
%#eml
%This function performs a trace back using the State transition Table call
%path.
p1=path(Idx,1); %starting path
%This is a traceback function that follows the state path
for i=2:size(path,2)
    p2=path(p1,i);
    p1=p2;
end

y=p2-1; %Past State
```

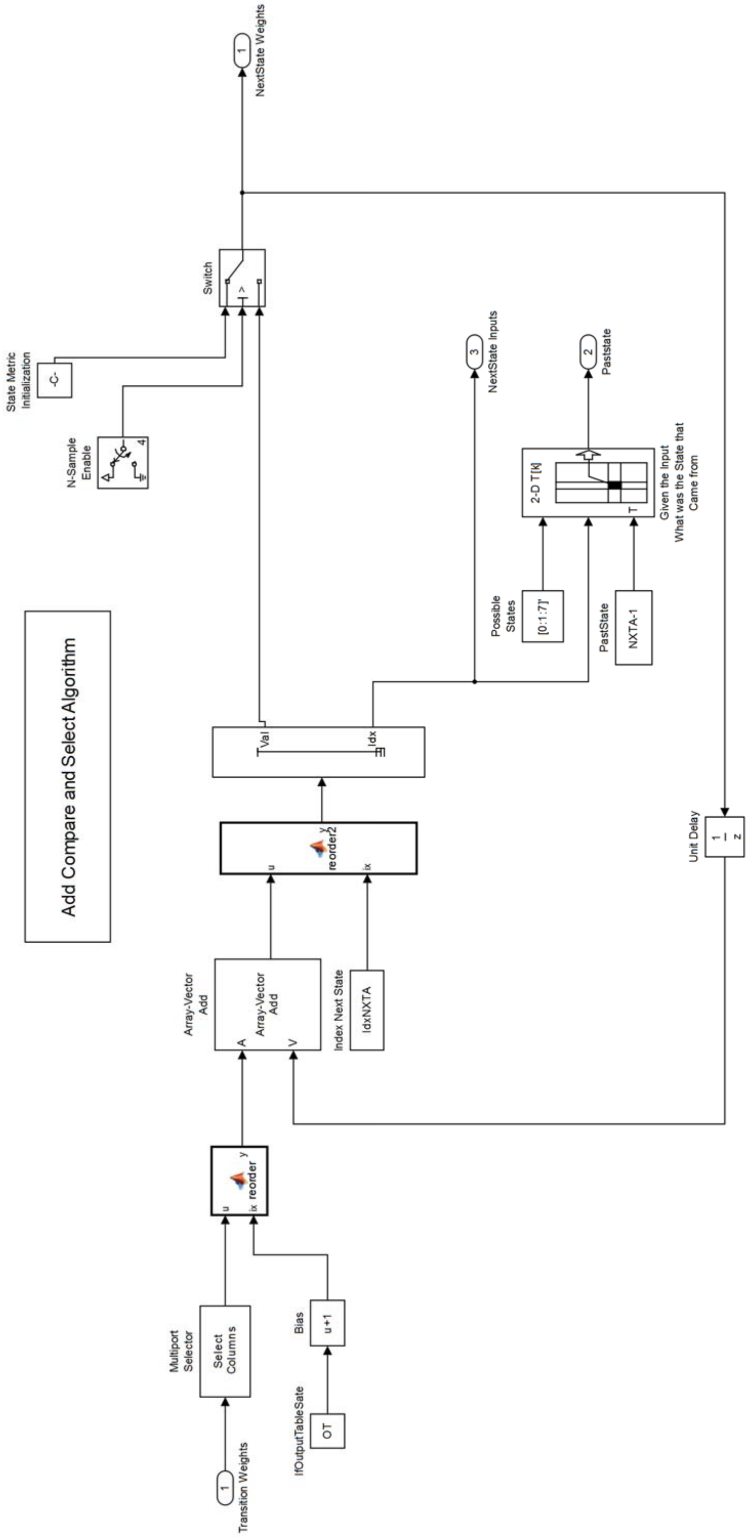

Figure 10.3: Simulink Path Metric Unit subsystem.

The function "TBA" is a for loop that traverses back to the trellis path vector to obtain the past state. The output is stored in the variable "y".

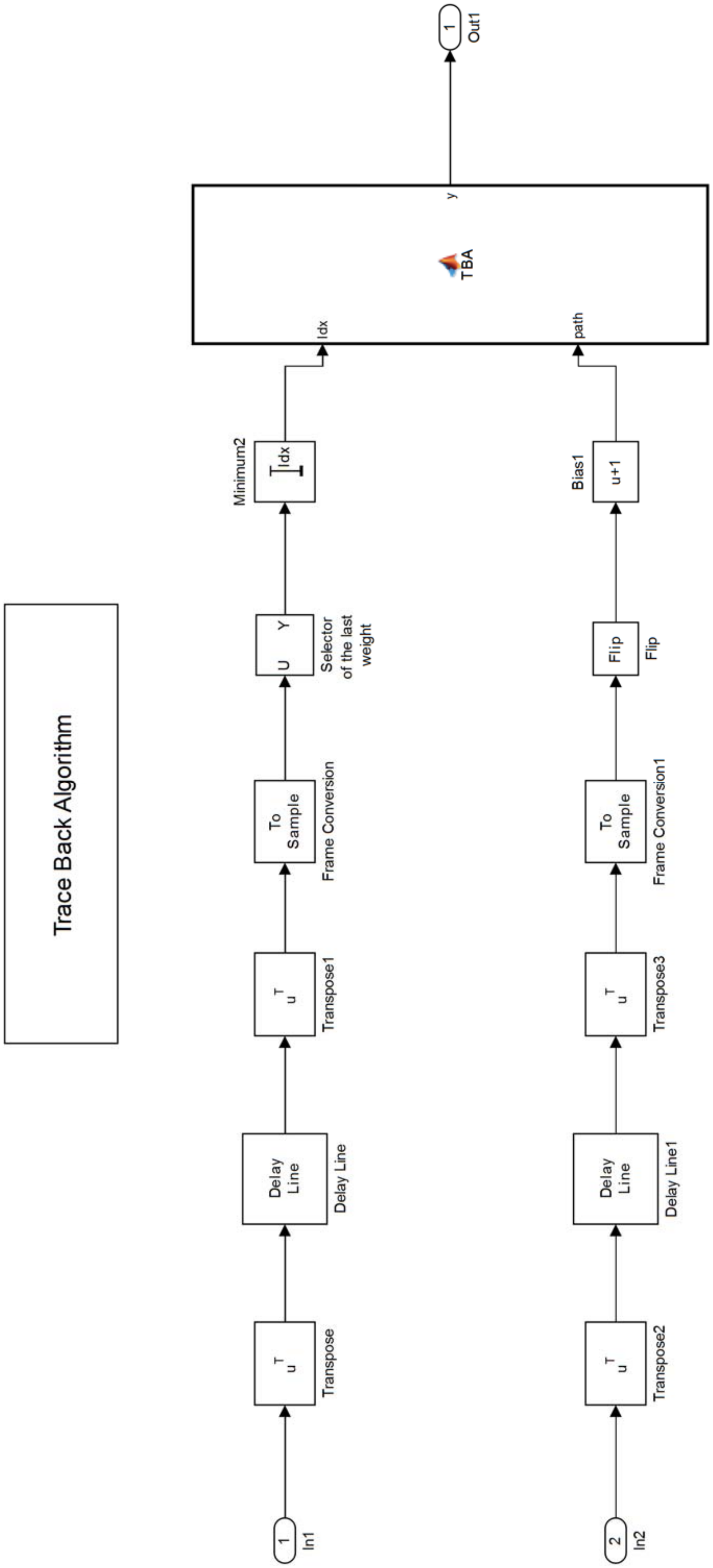

Figure 10.4: Simulink Trace Back Unit subsystem.

Chapter 11 Conclusions and Suggestions for Further Work

The main contribution of this thesis was to show the design and performance of a TCM system using the expanded 16D CEQ^{2}PSK constellation that allows the introduction of 1 bit of redundancy every 12 bits without constellation expansion penalty. We used two simple convolutional encoders of rates 2/3 and 3/4 to achieve moderate coding gains while maintaining constant envelope and without reducing the bandwidth efficiency over the uncoded CEQ^{2}PSK reference system. Considerably higher gains may be obtained with the same constellation by using more complex encoders. The system was simulated first in AWGN and then in Fading channels. Spectral analysis was performed.

Future work will include an analysis of the actual bandwidth efficiency of the system by simulating band-limited channels. This may be accomplished by placing bandlimiting filters in our Simulink model. The effects of non-linearities in the channel will be incorporated into the study, and the performance in fading channels will also be evaluated.

For fading channels, it is important to use an Interleaver in the transmitter and the corresponding de-interleaver at the receiver. This should be done and simulations should then be run. Interleaving needs to be performed prior to transmission of the encoded bits. This way, when error bursts or fading events occur, the event will not affect more than a bit of a given symbol or several consecutive symbols as is the case with slow fading without interleaving. Instead, the effect of fading is split into many different non-consecutive bits of different symbols and therefore errors will be spread and easier to correct.

Indeed, for the fading environment, much longer simulations are needed; the author shall investigate the best way to accurately and efficiently evaluate performance in fading channels.

In our simulations we assumed that the phase out of the fading channels was removed or, more accurately, was assumed known. Phase estimators should be developed and implemented and then simulations run to determine how the probability of bit error deteriorates with imperfect phase knowledge.

Additional analysis using a Morlet wavelet transform can be implemented to mitigate and find local disturbances such as the impulse noise or changes from slow fading to fast fading.

Finally, a longer-term project would be to implement the system in hardware by using, for example, FPGAs. Field trials could then be performed.

Bibliography

[1] C. E. Shannon, "Communication in the presence of noise," *Proc. of the IRE*, vol. 37, no. 1, pp. 10–21, 1949.

[2] G. Forney and G. Ungerboeck, "Modulation and coding for linear Gaussian channels," *IEEE Trans. Inf. Theory*, vol. 44, no. 6, pp. 2384–2415, 1998.

[3] E. Biglieri and M. Elia, "Multidimensional modulation and coding for band-limited digital channels," *IEEE Trans. Inf. Theory*, vol. 34, no. 4, pp. 803–809, 1988.

[4] A. Gersho and V. Lawrence, "Multidimensional signal constellations for voiceband data transmission," *IEEE J. Sel. Areas Commun.*, vol. 2, no. 5, pp. 687–702, 1984.

[5] B. Sklar, "Rayleigh fading channels in mobile digital communication systems .I. Characterization," *IEEE Commun. Mag.*, vol. 35, no. 7, pp. 90–100, 1997.

[6] ——, "Rayleigh fading channels in mobile digital communication systems part II: Mitigation," *IEEE Commun. Mag.*, vol. 35, no. 9, pp. 148–155, 1997.

[7] Q. Xie, J. Song, K. Peng, F. Yang, and Z. Wang, "Coded modulation with signal space diversity," *IEEE Trans. Wireless Commun.*, vol. 10, no. 2, pp. 660–669, 2011.

[8] Z. Shi, J. Li, and Z. Zhang, "New strategies for coded modulation diversity over Rayleigh fading channels," in *Wireless Communications and Networking Conference (WCNC), 2010 IEEE*, 2010, pp. 1–6.

[9] Y. Li, X.-G. Xia, and G. Wang, "Simple iterative methods to exploit the signal-space diversity," *IEEE Trans. Commun.*, vol. 53, no. 1, pp. 32–38, 2005.

[10] E. Biglieri, J. Proakis, and S. Shamai, "Fading channels: information-theoretic and communications aspects," *IEEE Trans. Inf. Theory*, vol. 44, no. 6, pp. 2619–2692, 1998.

[11] P. H. Moose, D. Roderick, R. North, and M. Geile, "A COFDM-based radio for HDR LOS networked communications," in *Proceedings of the 1999 International Conference on Communications*, vol. 1, 1999, pp. 187–192.

[12] J. Boutros and E. Viterbo, "Signal space diversity: a power- and bandwidth-efficient diversity technique for the Rayleigh fading channel," *IEEE Trans. Inf. Theory*, vol. 44, no. 4, pp. 1453–1467, 1998.

[13] S. X. Ng and L. Hanzo, "On the MIMO channel capacity of multidimensional signal sets," *IEEE Trans. Veh. Technol.*, vol. 55, no. 2, pp. 528–536, 2006.

[14] G. Guvensen and A. Yilmaz, "Iterative decision feedback equalization and decoding for rotated multidimensional constellations in block fading channels," in *Vehicular Technology Conference, 2009. VTC Spring 2009. IEEE 69th*, 2009, pp. 1–6.

[15] Y.-M. Chen, C.-W. Chen, Y.-L. Ueng, and H.-C. Lee, "Look-up table based differential amplitude/phase modulation schemes for Rayleigh block fading channels," in *Vehicular Technology Conference 2013. VTC Fall 2013 IEEE 78th.*, 2013, pp. 1–5.

[16] A. Fabregas and G. Caire, "Multidimensional coded modulation in block-fading channels," in *Information Theory, 2007. ISIT 2007. IEEE International Symposium on*, 2007, pp. 1816–1820.

[17] A. Guillen i Fabregas and G. Caire, "Multidimensional coded modulation in block-fading channels," *IEEE Trans. Inf. Theory*, vol. 54, no. 5, pp. 2367–2372, 2008.

[18] M. Alfasi and Y. Shayan, "Multi-dimensional signal mapping for MIMO-BICM-ID over block fading channels," in *Personal, Indoor and Mobile Radio Communications, 2009 IEEE 20th International Symposium on*, 2009, pp. 1327–1331.

[19] D. Saha, "Channel coding with quadrature-quadrature phase shift-keying (Q^2PSK) signals," *IEEE Trans. Commun.*, vol. 38, pp. 409–417, Apr. 1990.

[20] M. I. Quinteros, E. J. Kaminsky, K. V. Cartwright, and R. U. Gallegos, "A novel expanded 16-dimensional constant envelope Q^2PSK constellation," in *Proc. IEEE TechCon 2008, Region 5 Conference.* Kansas City, MO: IEEE, April 17-20 2008, pp. 1–6.

[21] M. Quinteros, E. J. Kaminsky, and K. Cartwright, "A trellis-coded modulation scheme with a novel expanded 16-dimensional constant envelope Q^2PSK constellation," in *Proc. IEEE GLOBECOM 2009.* Honolulu, HI, USA: IEEE, December 2009, pp. 1–6.

[22] E. Kaminsky, J. Ayo, and K. Cartwright, "TCM without constellation expansion penalty," *IKCS-IEEE Journal of Communications and Networks*, vol. 4, no. 2, pp. 90–96, June 2002.

[23] C.-D. Iskander, "A matlab-based object-oriented approach to multipath fading channel simulation," *MATLAB White Paper*, 2008.

[24] D. Saha and T. G. Birdsall, "Quadrature-quadrature phase shift keying," *IEEE Trans. Commun.*, vol. 37, no. 4, pp. 437–448, 1989.

[25] J. Forney, G.D. and L.-F. Wei, "Multidimensional constellations. I. Introduction, figures of merit, and generalized cross constellations," *IEEE J. Sel. Areas Commun.*, vol. 7, no. 6, pp. 877–892, 1989.

[26] G. D. Forney, "Coset codes. Part 1: Introduction and geometrical classification," *IEEE Trans. Inf. Theory*, vol. 34, no. 5, pp. 1123–1151, Sept. 1988.

[27] M. Visintin, E. Biglieri, and V. Castellani, "Four-dimensional signaling for bandlimited channels," *IEEE Trans. Commun.*, vol. 42, no. 234, pp. 403–409, 1994.

[28] G. Ungerboeck, "Trellis-coded modulation with redundant signal sets, part I: Introduction," *IEEE Commun. Magazine*, vol. 25, no. 2, pp. 5–11, Feb. 1987.

[29] E. J. Kaminsky, K. V. Cartwright, and A. B. Martinez, "Constant envelope eight dimensional TCM schemes," in *Conf. Proc. IEEE ICC'91, International Conf. Commun.*, IEEE. Denver, CO: IEEE Press, June 1991, pp. 231–235.

[30] C. Durand, E. Bejjani, and J. Boutros, "Multidimensional signals with correlated frequencies for noncoherent detection over the Rayleigh channel," in *Proc. IEEE International Symposium on Information Theory*, Sorrento, Italy, 2000.

[31] E. J. Kaminsky, "Trellis coding and adaptive estimation in dually polarized systems," Ph.D. Dissertation, Tulane University, Department of Electrical Engineering, New Orleans, LA 70118, June 1991.

[32] G. Forney and R. Gallagher, "Efficient modulation for bandlimited channels," *IEEE J. on Selected Areas in Communic.*, vol. SAC-2, no. 5, Sept. 1984.

[33] D. Saha and A. Arbor, "Quadrature-quadrature phase shift keying," U.S. Patent Office, US Patent 4,680,777, July 14, 1987.

[34] M. Quinteros, E. J. Kaminsky, and K. Cartwright, "Performance and spectral analysis of Q^2PSK and CEQ^2PSK systems in ideal bandlimited channels," in *Proc. IEEE GLOBECOM 2014*, Dec. 2014, pp. 1–6.

[35] K. V. Cartwright and E. J. Kaminsky, "An optimum hardware detector for constant envelope quadrature-quadrature phase-shift keying (CEQ^{2}PSK)," in *Proc. IEEE GLOBECOM'05*. St. Louis, MO: IEEE, 28 Nov.–2 Dec. 2005, pp. 393–396.

[36] J. Anderson and C.-E. Sundberg, "Advances in constant envelope coded modulation," *IEEE Commun. Mag.*, vol. 29, no. 12, pp. 36–45, 1991.

[37] G. Ungerboeck, "Channel coding with multilevel/phase signals," *IEEE Trans. Info. Theory*, vol. IT-28, no. 1, pp. 55–66, Jan. 1982.

[38] ——, "Trellis-coded modulation with redundant signal sets, part II: State of the art," *IEEE Commun. Magazine*, vol. 25, no. 2, pp. 12–20, Feb. 1987.

[39] L.-F. Wei, "Trellis-coded modulation with multidimensional constellations," *IEEE Trans. Inf. Theory*, vol. IT-33, no. 4, pp. 483–501, July 1987.

[40] J. G. Proakis, M. Salehi, N. Zhou, and X. Li, *Communication systems engineering.* Prentice-hall Englewood Cliffs, 1994, vol. 2.

[41] K. Shanmugam and P. Balaban, "A modified monte-carlo simulation technique for the evaluation of error rate in digital communication systems," *IEEE Trans. Commun.*, vol. 28, no. 11, pp. 1916–1924, 1980.

[42] K. V. Ravi and H. K. Ratha, "Error performance of rate-5/6 multidimensional TCM in Rician and Rayleigh fading mobile channels," in *Proc. IEEE GLOBECOM'97*, vol. 3. Phoenix, AZ: IEEE, Nov. 3–8 1997, pp. 1534–1538.

[43] C. Sterian, F. Laue, and M. Pätzold, "Trellis-coded quadrature amplitude modulation with 2N-dimensional constellations for mobile radio channels," *IEEE Trans. Vehicular Tech.*, vol. 48, no. 5, pp. 1475–1487, Sept. 1999.

[44] D. Saha, "Quadrature-quadrature phase shift keying with constant envelope," US Patent 4,730,344, March, 1988.

[45] B. H. Waldeck, S. A. Swanepoel, and L. P. Linde, "TFO Q^{2}PSK: A multi-dimensional spectrally efficient modulation scheme," in *Proc. 1998 South African Symp. Commun. Signal Proc.*, Sep 1998, pp. 39–42.

[46] M. Fertat, W. Zschunke, and A. Berraissoul, "Spectral optimization of QPSK and Q^{2}PSK systems using timelimited and zero-ISI pulse shaping," *Frequenz*, vol. 57, no. 9-10, pp. 197–203.

[47] B. Westra, D. Van Wyk, J. Cilliers, and L. Linde, "Performance evaluation of multilevel four-dimensional Q^{2}PSK in Gaussian noise," in *Proc. COMSIG 97, South African Symp. Commun. Signal Proc.*, Sept. 1997, pp. 141–146.

[48] D. Saha and O. El-Ghandour, "Differentially coherent quadrature-quadrature phase shift keying (Q^{2}PSK)," in *Conf. Record IEEE MILCOM '90, Military Commun. Conf.*, vol. 2, Sep 1990, pp. 585–589.

[49] V. Acha and R. Carrasco, "A new digital implementation of quadrature-quadrature phase shift keying," in *Proc. Third IEE Conference on Telecommunic.*, Edinburgh, Mar 1991, pp. 29–34.

[50] I. Korn and L. Wei, "Q^{2}DPSK in the satellite mobile channel with ISI and CSI," *IEEE Trans. Veh. Technol.*, vol. 43, no. 1, pp. 69–78, Feb. 1994.

[51] J. Cilliers and L. P. Linde, "Performance of an adaptive multi-dimensional lattice equaliser for Q^2PSK over multipath channels," in *Proc. IEEE AFRICON 2001, 6th. Africon Conf. in Africa*, vol. 1, Oct 2002, pp. 155–160.

[52] V. Acha and R. Carrasco, "Trellis coded Q^2PSK signals. I. AWGN and nonlinear satellite channels," *IEE Proc. -Commun.*, vol. 141, no. 3, pp. 151–158, June 1994.

[53] J. S. Han and M. J. Kim, "Offset quadrature-quadrature phase shift keying with half-sine pulse shaping," in *Proc. ICTC 2013, Internat. Conf. Convergence*, 2013, pp. 931–935.

[54] K. Priya and M. Tamilarasi, "A trellis-coded modulation scheme with 32-dimensional constant envelope Q^2PSK constellation," in *Proc. ICCSP 2013 conf., Commun. Signal Proc.*, 2013, pp. 821–825.

[55] J. M. Wozencraft and I. M. Jacobs, *Principles of communication engineering.* John Wiley & Sons, 1965.

[56] O. Shimbo and M. Celebiler, "The probability of error due to intersymbol interference and Gaussian noise in digital communication systems," *IEEE Trans. Commun. Technol.*, vol. 19, no. 2, pp. 113–119, 1971.

[57] D. Van Wyk, "Four-dimensional Q^2PSK modulation and coding for mobile digital communication," Master's Thesis, University of Pretoria, South Africa, April 1996.

[58] J. E. Cilliers, "Multi-dimensional lattice equaliser for Q^2PSK," Master's thesis, University of Pretoria, 2002.

[59] S. Drakul and E. Biglieri, "A class of constant envelope multi-dimensional modulation schemes for non-linearly amplified channels," in *Singapore ICCS '94. Conference Proceedings.*, vol. 1, Nov 1994, pp. 114–118 vol.1.

[60] E. Malan, "Multi-dimensional direct-sequence spread spectrum multiple-access communication with adaptive channel coding," Master's thesis, University of Pretorra, November 2006.

[61] A. J. Viterbi, "Error bounds for convolutional codes and an asymptotically optimum decoding algorithm," *IEEE Trans. Inf. Theory*, vol. IT-13, no. 2, pp. 260–269, Apr. 1967.

[62] G. C. Clark and J. B. Cain, *Error-Correction Coding for Digital Communications.* New York, NY, USA: Plenum Press, 1981, ch. Convolutional Code Structure and Viterbi Decoding, pp. 262–263.

[63] R. A. Carrasco and P. G. Farrell, "Ring-TCM for fixed and fading channels: Land-mobile satellite fading channels with QAM," *IEE Proc. Commun.*, vol. 143, no. 5, pp. 281–287, Oct. 1996.

[64] D. Divsalar and M. K. Simon, "The design of trellis coded MPSK for fading channels: Performance criteria," *IEEE Trans. Commun.*, vol. 36, no. 9, pp. 1004–1012, Sept. 1988.

Appendix A General Equation for filtered signals

The expressions for the filtered half-cosine and half-sine pulses, p_{1f} and p_{2f} are presented here. The low pass filter with support band from $[0,\omega_b]$, where $\omega_b = 2\pi B$ is the radians/sec bandwidth and B is the bandwidth in Hz which is defined as follows:

$$H(\omega) = \begin{cases} 1 \quad \text{if} \quad |\omega| \leq \omega_b \\ \\ 0 \quad \text{if} \quad |\omega| > \omega_b. \end{cases}$$

The impulse response is defined as follows:

$$\begin{aligned} h(t) &= \frac{1}{2\pi}\int_{-\infty}^{\infty} H(\omega)e^{j\omega t}d\omega \\ &= \frac{1}{2\pi}\int_{-\omega_b}^{\omega_b} H(\omega)e^{j\omega t}d\omega \\ &= \frac{1}{t\pi}\frac{[e^{j\omega_b t} - e^{j\omega_b t}]}{j2} \\ &= \frac{\omega_b}{\pi} \times \frac{\sin(\omega_b t)}{\omega_b t}, \end{aligned} \tag{A.1}$$

where the sinc function is:

$$Sinc(x) = \frac{\sin(x)}{x}. \tag{A.2}$$

Now replacing (A.2) in (A.1), we have the following:

$$h(t) = \frac{\omega_b}{\pi} \times Sinc(\omega_b t). \tag{A.3}$$

Now, lets defined the unit step function as:

$$\mu(t) = \begin{cases} 1 & \text{if} \quad t \geq 0 \\ 0 & \text{if} \quad t < 0 \end{cases},$$

and the unitbox function is defined as:

$$\begin{aligned} UB(\frac{t}{2T}) &= \mu(t+T) - \mu(t-T) \\ UB(\frac{t}{2T}) &= \begin{cases} 1 & \text{if} \quad |t| \leq T \\ 0 & \text{if} \quad |t| > T \end{cases}, \end{aligned}$$

where $2T$ is the symbol interval for a Q^{2}PSK signal.

$$\begin{aligned} P_1(t) &= A \times \cos(\frac{\pi}{2T}t) \times UB(\frac{t}{2T}) \\ &= A \times \cos(\omega_\alpha t) \times UB(\frac{t}{2T}), \end{aligned} \tag{A.4a}$$

where $\omega_\alpha = \frac{\pi}{2T}$. and A for simplicity is equal to 1.

To filter $P_1(t)$ we convolve with $h(t)$ and the band-limited version is defined as $P_{1b}(t)$

$$
\begin{aligned}
p_{1f}(t) &= P_1(t) \circledast h(t) \\
&= \int_{-\infty}^{\infty} P_1(\tau) \times h(t-\tau) \times d\tau, \\
&= \int_{-\infty}^{\infty} P_1(t-\tau) \times h(\tau) \times d\tau.
\end{aligned} \tag{A.5}
$$

In (A.5) place (A.4a), and (A.3) and the value is as follows:

$$
\begin{aligned}
p_{1f}(t) &= \int_{-\infty}^{\infty} P_1(t-\tau) \times h(\tau) \times d\tau \\
&= \int_{-\infty}^{\infty} A \times \cos(\omega_\alpha(t-\tau)) \times UB(\frac{t-\tau}{2T}) \times \frac{\omega_b}{\pi} \times Sinc(\omega_b\tau) \times d\tau \\
&= \int_{-\infty}^{\infty} A \times \cos(\omega_\alpha t - \omega_\alpha \tau) \times UB(\frac{t-\tau}{2T}) \times \frac{\omega_b}{\pi} \times \frac{\sin(\omega_b t)}{\omega_b t} \times d\tau \\
&= A \times \frac{\omega_b}{\pi} \times \int_{-\infty}^{\infty} \cos(\omega_\alpha t - \omega_\alpha \tau) \times \frac{\sin(\omega_b \tau)}{\omega_b \tau} \times UB(\frac{t-\tau}{2T}) \times d\tau.
\end{aligned} \tag{A.6}
$$

In this derivation, we are going to use the following trigonometric identities:

$$\cos(a-b) = \cos(a)\cos(b) + \sin(b)\sin(a) \tag{A.7}$$

$$\cos(a) \times \sin(b) = \frac{\sin(a+b) - \sin(a-b)}{2} \tag{A.8}$$

$$\sin(a) \times \sin(b) = \frac{\cos(a-b) - \cos(a+b)}{2}. \tag{A.9}$$

Use (A.7) in (A.6)

$$\begin{aligned} p_{1f}(t) = A \times \frac{\omega_b}{\pi} \times \int_{-\infty}^{\infty} (\cos(\omega_\alpha t) \times \cos(\omega_\alpha \tau) + \sin(\omega_\alpha \tau) \times \\ \times \sin(\omega_\alpha t)) \times \frac{\sin(\omega_b \tau)}{\omega_b \tau} \times UB(\frac{t-\tau}{2T}) \times d\tau \end{aligned} \tag{A.10a}$$

The above equation can be simplified:

$$\begin{aligned} p_{1f}(t) &= A \times \frac{\omega_b}{\pi} \times \int_{-\infty}^{\infty} (\cos(\omega_\alpha t) \times \cos(\omega_\alpha \tau) \times \frac{\sin(\omega_b \tau)}{\omega_b \tau} \times UB(\frac{t-\tau}{2T}) \times d\tau + \\ &+ A \times \frac{\omega_b}{\pi} \times \int_{-\infty}^{\infty} \sin(\omega_\alpha t) \times \sin(\omega_\alpha \tau) \times \frac{\sin(\omega_b \tau)}{\omega_b \tau} \times UB(\frac{t-\tau}{2T}) \times d\tau \\ &= A \times \frac{\omega_b}{\pi} \times \cos(\omega_\alpha t) \int_{-\infty}^{\infty} \cos(\omega_\alpha \tau) \times \frac{\sin(\omega_b \tau)}{\omega_b \tau} \times UB(\frac{t-\tau}{2T}) \times d\tau + \\ &+ A \times \frac{\omega_b}{\pi} \times \sin(\omega_\alpha t) \int_{-\infty}^{\infty} \sin(\omega_\alpha \tau) \times \frac{\sin(\omega_b \tau)}{\omega_b \tau} \times UB(\frac{t-\tau}{2T}) \times d\tau \\ &= A \times \frac{\omega_b}{\pi} \times \cos(\omega_\alpha t) \int_{-\infty}^{\infty} \frac{\sin([\omega_\alpha + \omega_b]\tau) - \sin([\omega_\alpha - \omega_b]\tau)}{2\omega_b \tau} \times UB(\frac{t-\tau}{2T}) \times d\tau + \\ &+ A \times \frac{\omega_b}{\pi} \times \sin(\omega_\alpha t) \int_{-\infty}^{\infty} \frac{\cos([\omega_\alpha - \omega_b]\tau) - \cos([\omega_\alpha + \omega_b]\tau)}{2\omega_b \tau} \times UB(\frac{t-\tau}{2T}) \times d\tau \\ &= A \times \frac{1}{2\pi} \times \cos(\omega_\alpha t) \int_{-\infty}^{\infty} \frac{\sin([\omega_\alpha + \omega_b]\tau)}{\tau} \times UB(\frac{t-\tau}{2T}) \times d\tau + \\ &- A \times \frac{1}{2\pi} \times \cos(\omega_\alpha t) \int_{-\infty}^{\infty} \frac{\sin([\omega_\alpha - \omega_b]\tau)}{\tau} \times UB(\frac{t-\tau}{2T}) \times d\tau + \\ &+ A \times \frac{1}{2\pi} \times \sin(\omega_\alpha t) \int_{-\infty}^{\infty} \frac{\cos([\omega_\alpha - \omega_b]\tau)}{\tau} \times UB(\frac{t-\tau}{2T}) \times d\tau + \\ &- A \times \frac{1}{2\pi} \times \sin(\omega_\alpha t) \int_{-\infty}^{\infty} \frac{\cos([\omega_\alpha + \omega_b]\tau)}{\tau} \times UB(\frac{t-\tau}{2T}) \times d\tau \end{aligned} \tag{A.11}$$

Before to continue with the mathematical manipulation let's define two functions:

$$\mathrm{Si}(x) = \int_{0}^{x} \frac{\sin(t)}{t} dt \tag{A.12}$$

$$\operatorname{Ci}(x) = -\int_{x}^{\infty} \frac{\cos(t)}{t} dt \tag{A.13}$$

Let's also define the following integral

$$\begin{aligned}
\int_{\tau=t-T}^{\tau=t+T} \frac{\sin(A\tau)}{\tau} \times d\tau &= \int_{\tau=0}^{\tau=t+T} \frac{\sin(A\tau)}{\tau} \times d\tau + \int_{\tau=t-T}^{\tau=0} \frac{\sin(A\tau)}{\tau} \times d\tau \\
&= \int_{\tau=0}^{\tau=t+T} \frac{A\sin(A\tau)}{A\tau} \times d\tau + \int_{\tau=t-T}^{\tau=0} \frac{A\sin(A\tau)}{A\tau} \times d\tau \\
&= \int_{u=0}^{u=A(t+T)} \frac{\sin(A\tau)}{A\tau} \times A d\tau - \int_{u=0}^{u=(t-T)A} \frac{\sin(A\tau)}{A\tau} \times A d\tau \\
&= \operatorname{Si}(A(t+T))) - \operatorname{Si}(A(t-T))).
\end{aligned} \tag{A.14}$$

Now for the integral with the cosine, we have the following:

$$\begin{aligned}
\int_{\tau=t-T}^{\tau=t+T} \frac{\cos(A\tau)}{\tau} \times d\tau &= \int_{\tau=t-T}^{\tau=\infty} \frac{\cos(A\tau)}{\tau} \times d\tau - \int_{\tau=t+T}^{\tau=\infty} \frac{\cos(A\tau)}{\tau} \times d\tau \\
&= -\left[-\int_{\tau=t-T}^{\tau=\infty} \frac{A\cos(A\tau)}{A\tau} \times d\tau \right] - \int_{\tau=t+T}^{\tau=\infty} \frac{A\cos(A\tau)}{A\tau} \times d\tau \\
&= -\left[-\int_{u=A(t-T)}^{u=\infty} \frac{\cos(A\tau)}{A\tau} \times A d\tau \right] - \left[\int_{u=A(t+T)}^{u=\infty} \frac{\cos(A\tau)}{A\tau} \times A d\tau \right] \\
&= \operatorname{Ci}(A(t+T)) - \operatorname{Ci}(A(t-T)).
\end{aligned} \tag{A.15}$$

In(A.11) use (A.14) and (A.15) the final expression for the cosine pulse filtered:

$$\begin{aligned}
p_{1f}(t) &= A \times \frac{1}{2\pi} \times \cos(\omega_\alpha t)\left[\int_{\tau=t-T}^{\tau=t+T} \frac{\sin([\omega_\alpha + \omega_b]\tau)}{\tau} \times d\tau\right] + \\
&- A \times \frac{1}{2\pi} \times \cos(\omega_\alpha t)\left[\int_{\tau=t-T}^{\tau=t+T} \frac{\sin([\omega_\alpha - \omega_b]\tau)}{\tau} \times d\tau\right] + \\
&+ A \times \frac{1}{2\pi} \times \sin(\omega_\alpha t)\left[\int_{\tau=t-T}^{\tau=t+T} \frac{\cos([\omega_\alpha - \omega_b]\tau)}{\tau} \times d\tau\right] + \\
&- A \times \frac{1}{2\pi} \times \sin(\omega_\alpha t)\left[\int_{\tau=t-T}^{\tau=t+T} \frac{\cos([\omega_\alpha + \omega_b]\tau)}{\tau} \times d\tau\right] \\
&= A \times \frac{1}{2\pi} \times \cos(\omega_\alpha t)\left[\mathrm{Si}((t+T)(\omega_\alpha + \omega_b))\right] - A \times \frac{1}{2\pi} \times \cos(\omega_\alpha t)\left[\mathrm{Si}((t-T)(\omega_\alpha + \omega_b))\right] + \\
&- A \times \frac{1}{2\pi} \times \cos(\omega_\alpha t)\left[\mathrm{Si}((t+T)(\omega_\alpha - \omega_b)) - \mathrm{Si}((t-T)(\omega_\alpha - \omega_b))\right] + \\
&+ A \times \frac{1}{2\pi} \times \sin(\omega_\alpha t)\left[\mathrm{Ci}((t+T)(\omega_\alpha - \omega_b)) - \mathrm{Ci}((t-T)(\omega_\alpha - \omega_b))\right] + \\
&- A \times \frac{1}{2\pi} \times \sin(\omega_\alpha t)\left[\mathrm{Ci}((t+T)(\omega_\alpha + \omega_b)) - \mathrm{Ci}((t-T)(\omega_\alpha + \omega_b))\right].
\end{aligned}$$

Finally the expression for $p_{1f}(t)$ is:

$$\begin{aligned}
p_{1f}(t) = \frac{1}{2\pi}\sin(\omega_\alpha t)\left[\mathrm{Ci}\left((t-T)\left(\omega_\alpha + \omega_\beta\right)\right) + \right. \\
- \mathrm{Ci}\left((t+T)\left(\omega_\alpha + \omega_\beta\right)\right) + \mathrm{Ci}\left((t+T)\left(\omega_\beta - \omega_\alpha\right)\right) + \\
\left. - \mathrm{Ci}((t-T)(\omega_\beta - \omega_\alpha))\right] + \\
+\frac{1}{2\pi}\cos(\omega_\alpha t)\left[\mathrm{Si}((t+T)(\omega_\beta - \omega_\alpha)) + \right. \\
- \mathrm{Si}((t-T)(\omega_\beta - \omega_\alpha)) + \mathrm{Si}((t+T)(\omega_\alpha + \omega_\beta)) + \\
\left. - \mathrm{Si}((t-T)(\omega_\alpha + \omega_\beta))\right].
\end{aligned} \tag{A.16}$$

Finally, $P_2(t)$ which is defined in equation A.17 is convolved with $h(t)$. The bandlimited version of $P_2(t)$ is defined as $p_{2f}(t)$.

$$\begin{aligned} P_2(t) &= A \times \sin(\frac{\pi}{2T}t) \times UB(\frac{t}{2T}) \\ &= A \times \sin(\omega_\alpha t) \times UB(\frac{t}{2T}), \end{aligned} \tag{A.17}$$

$$\begin{aligned} p_{2f}(t) &= P_2(t) \circledast h(t) \\ &= \int_{-\infty}^{\infty} P_2(\tau) \times h(t-\tau) \times d\tau \\ &= \int_{-\infty}^{\infty} P_2(t-\tau) \times h(\tau) \times d\tau \end{aligned} \tag{A.18}$$

In (A.18) place (A.17), and (A.3) and the value is as follows:

$$\begin{aligned} p_{2f}(t) &= \int_{-\infty}^{\infty} A \times \sin(\omega_\alpha(t-\tau)) \times UB(\frac{t-\tau}{2T}) \times \frac{\omega_b}{\pi} \times Sinc(\omega_b\tau) \times d\tau \\ &= \int_{-\infty}^{\infty} A \times \sin(\omega_\alpha t - \omega_\alpha\tau) \times UB(\frac{t-\tau}{2T}) \times \frac{\omega_b}{\pi} \times \frac{\sin(\omega_b t)}{\omega_b t} \times d\tau \\ &= A \times \frac{\omega_b}{\pi} \times \int_{-\infty}^{\infty} \sin(\omega_\alpha t - \omega_\alpha\tau) \times \frac{\sin(\omega_b\tau)}{\omega_b\tau} \times UB(\frac{t-\tau}{2T}) \times d\tau \end{aligned} \tag{A.19}$$

Use (A.9) in (A.19)

$$\begin{aligned} p_{2f}(t) = A \times \frac{\omega_b}{\pi} \times \int_{-\infty}^{\infty} &(\sin(\omega_\alpha t) \times \cos(\omega_\alpha\tau) - \sin(\omega_\alpha\tau) \times \cos(\omega_\alpha t)) \times \\ &\times \frac{\sin(\omega_b\tau)}{\omega_b\tau} \times UB(\frac{t-\tau}{2T}) \times d\tau \end{aligned} \tag{A.20a}$$

The equation (A.20a) can be simplified:

$$
\begin{aligned}
p_{2f}(t) &= A \times \frac{\omega_b}{\pi} \times \int_{-\infty}^{\infty} (\sin(\omega_\alpha t) \times \cos(\omega_\alpha \tau) \times \frac{\sin(\omega_b \tau)}{\omega_b \tau} \times UB(\frac{t-\tau}{2T}) \times d\tau + \\
&- \frac{\omega_b}{\pi} \times \int_{-\infty}^{\infty} \cos(\omega_\alpha t) \times \sin(\omega_\alpha \tau) \times \frac{\sin(\omega_b \tau)}{\omega_b \tau} \times UB(\frac{t-\tau}{2T}) \times d\tau \\
&= A \times \frac{\omega_b}{\pi} \times \sin(\omega_\alpha t) \int_{-\infty}^{\infty} \cos(\omega_\alpha \tau) \times \frac{\sin(\omega_b \tau)}{\omega_b \tau} \times UB(\frac{t-\tau}{2T}) \times d\tau + \\
&- \frac{\omega_b}{\pi} \times \cos(\omega_\alpha t) \int_{-\infty}^{\infty} \sin(\omega_\alpha \tau) \times \frac{\sin(\omega_b \tau)}{\omega_b \tau} \times UB(\frac{t-\tau}{2T}) \times d\tau \\
&= A \times \frac{\omega_b}{\pi} \times \sin(\omega_\alpha t) \int_{-\infty}^{\infty} \frac{\sin([\omega_\alpha + \omega_b]\tau) - \sin([\omega_\alpha - \omega_b]\tau)}{2\omega_b \tau} \times UB(\frac{t-\tau}{2T}) \times d\tau + \\
&- \frac{\omega_b}{\pi} \times \cos(\omega_\alpha t) \int_{-\infty}^{\infty} \frac{\cos([\omega_\alpha - \omega_b]\tau) - \cos([\omega_\alpha + \omega_b]\tau)}{2\omega_b \tau} \times UB(\frac{t-\tau}{2T}) \times d\tau \\
&= A \times \frac{1}{2\pi} \times \sin(\omega_\alpha t) \int_{-\infty}^{\infty} \frac{\sin([\omega_\alpha + \omega_b]\tau)}{\tau} \times UB(\frac{t-\tau}{2T}) \times d\tau + \\
&- \frac{1}{2\pi} \times \sin(\omega_\alpha t) \int_{-\infty}^{\infty} \frac{\sin([\omega_\alpha - \omega_b]\tau)}{\tau} \times UB(\frac{t-\tau}{2T}) \times d\tau + \\
&- \frac{1}{2\pi} \times \cos(\omega_\alpha t) \int_{-\infty}^{\infty} \frac{\cos([\omega_\alpha - \omega_b]\tau)}{\tau} \times UB(\frac{t-\tau}{2T}) \times d\tau + \\
&+ \frac{1}{2\pi} \times \cos(\omega_\alpha t) \int_{-\infty}^{\infty} \frac{\cos([\omega_\alpha + \omega_b]\tau)}{\tau} \times UB(\frac{t-\tau}{2T}) \times d\tau \qquad \text{(A.21)}
\end{aligned}
$$

In(A.21) use (A.14) and (A.15) the final expression for the sine pulse filtered:

$$
\begin{aligned}
p_{2f}(t) &= A \times \frac{1}{2\pi} \times \sin(\omega_\alpha t) \left[\int_{\tau=t-T}^{\tau=t+T} \frac{\sin([\omega_\alpha + \omega_b]\tau)}{\tau} \times d\tau \right] + \\
&- A \times \frac{1}{2\pi} \times \sin(\omega_\alpha t) \left[\int_{\tau=t-T}^{\tau=t+T} \frac{\sin([\omega_\alpha - \omega_b]\tau)}{\tau} \times d\tau \right] + \\
&- A \times \frac{1}{2\pi} \times \cos(\omega_\alpha t) \left[\int_{\tau=t-T}^{\tau=t+T} \frac{\cos([\omega_\alpha - \omega_b]\tau)}{\tau} \times d\tau \right] + \\
&+ A \times \frac{1}{2\pi} \times \cos(\omega_\alpha t) \left[\int_{\tau=t-T}^{\tau=t+T} \frac{\cos([\omega_\alpha + \omega_b]\tau)}{\tau} \times d\tau \right] \\
&= A \times \frac{1}{2\pi} \times \sin(\omega_\alpha t) \left[\mathrm{Si}((t+T)(\omega_\alpha + \omega_b)) \right] - A \times \frac{1}{2\pi} \times \sin(\omega_\alpha t) \left[\mathrm{Si}((t-T)(\omega_\alpha + \omega_b)) \right] + \\
&- A \times \frac{1}{2\pi} \times \sin(\omega_\alpha t) \left[\mathrm{Si}((t+T)(\omega_\alpha - \omega_b)) - \mathrm{Si}((t-T)(\omega_\alpha - \omega_b)) \right] + \\
&- A \times \frac{1}{2\pi} \times \cos(\omega_\alpha t) \left[\mathrm{Ci}((t+T)(\omega_\alpha - \omega_b)) - \mathrm{Ci}((t-T)(\omega_\alpha - \omega_b)) \right] + \\
&+ A \times \frac{1}{2\pi} \times \cos(\omega_\alpha t) \left[\mathrm{Ci}((t+T)(\omega_\alpha + \omega_b)) - \mathrm{Ci}((t-T)(\omega_\alpha + \omega_b)) \right].
\end{aligned}
$$

Finally the expression for $p_{2f}(t)$ is:

$$
\begin{aligned}
p_{2f}(t) = \frac{1}{2\pi} \sin(\omega_\alpha t) \, [\mathrm{Si}((t+T)(\omega_\alpha + \omega_\beta)) + \\
- \mathrm{Si}((t-T)(\omega_\alpha + \omega_\beta)) + \mathrm{Si}((t+T)(\omega_\beta - \omega_\alpha)) + \\
- \mathrm{Si}((t-T)(\omega_\beta - \omega_\alpha))] + \\
+ \frac{1}{2\pi} \cos(\omega_\alpha t) \, [\mathrm{Ci}((t+T)(\omega_\alpha + \omega_\beta)) + \\
- \mathrm{Ci}((t-T)(\omega_\alpha + \omega_\beta)) - \mathrm{Ci}((t+T)(\omega_\beta - \omega_\alpha)) + \\
+ \mathrm{Ci}((t-T)(\omega_\beta - \omega_\alpha))].
\end{aligned}
\tag{A.22}
$$

Convolution of the channel impulse response $h(t)$ with the Q^{2}PSK pulses yields:

$$\begin{aligned}
p_{1f}(t) = \frac{1}{2\pi}\sin(\omega_\alpha t)\,[\mathrm{Ci}\left((t-T)\left(\omega_\alpha+\omega_\beta\right)\right)+ \\
-\,\mathrm{Ci}\left((t+T)\left(\omega_\alpha+\omega_\beta\right)\right)+\mathrm{Ci}\left((t+T)\left(\omega_\beta-\omega_\alpha\right)\right)+ \\
-\,\mathrm{Ci}((t-T)(\omega_\beta-\omega_\alpha))]+ \\
+\frac{1}{2\pi}\cos(\omega_\alpha t)\,[\mathrm{Si}((t+T)(\omega_\beta-\omega_\alpha))\,+ \\
-\,\mathrm{Si}((t-T)(\omega_\beta-\omega_\alpha))+\mathrm{Si}((t+T)(\omega_\alpha+\omega_\beta))+ \\
-\,\mathrm{Si}((t-T)(\omega_\alpha+\omega_\beta))]\,.
\end{aligned} \tag{A.23}$$

$$\begin{aligned}
p_{2f}(t) = \frac{1}{2\pi}\sin(\omega_\alpha t)\,[\mathrm{Si}((t+T)(\omega_\alpha+\omega_\beta))+ \\
-\,\mathrm{Si}((t-T)(\omega_\alpha+\omega_\beta))+\mathrm{Si}((t+T)(\omega_\beta-\omega_\alpha))+ \\
-\,\mathrm{Si}((t-T)(\omega_\beta-\omega_\alpha))]+ \\
+\frac{1}{2\pi}\cos(\omega_\alpha t)\,[\mathrm{Ci}((t+T)(\omega_\alpha+\omega_\beta))+ \\
-\,\mathrm{Ci}((t-T)(\omega_\alpha+\omega_\beta))-\mathrm{Ci}((t+T)(\omega_\beta-\omega_\alpha))+ \\
+\,\mathrm{Ci}((t-T)(\omega_\beta-\omega_\alpha))]\,.
\end{aligned} \tag{A.24}$$

where $\omega_\alpha = \frac{\pi}{2T}$ and $\omega_\beta = 2\pi B$, and the cosine and sine integrals, Ci and Si, are defined in (A.12) and (A.10a) respectively.

Appendix B General Equation for received signals without filter

$$
\begin{aligned}
p_1(t) &= \cos(\omega_\alpha t), \quad |t| \leq T && \text{(B.1a)} \\
p_2(t) &= \sin(\omega_\alpha t), \quad |t| \leq T && \text{(B.1b)}
\end{aligned}
$$

where $\omega_\alpha = \frac{\pi}{2T}$.

In this derivation, we use the following trigonometric identities:

$$
\begin{aligned}
\cos(a)\cos(b) &= \frac{\cos(a-b)+\cos(a+b)}{2}, && \text{(B.1c)} \\
\sin(a)\sin(b) &= \frac{\cos(a-b)-\cos(a+b)}{2}, && \text{(B.1d)} \\
\cos(a)\sin(b) &= \frac{\sin(a+b)-\sin(a-b)}{2}. && \text{(B.1e)}
\end{aligned}
$$

Convolution of p_1 with p_1.

$$
\begin{aligned}
y'_{11}(t) &= p_1(t) * p_1(t) && \text{(B.2)} \\
&= \int_{-\infty}^{\infty} p_1(\tau)p_1(t-\tau)d\tau,
\end{aligned}
$$

where

$$
\begin{aligned}
p_1(t-\tau) &= \cos(\omega_\alpha(t-\tau)), \quad |t-\tau| \leq T \\
&= \cos(\omega_\alpha t - \omega_\alpha \tau), \quad |t-\tau| \leq T.
\end{aligned}
$$

Now, we use trigonometric identities (B.1c) in (B.2) to simplify.

$$\begin{aligned}
y'_{11}(t) &= \int_{-\infty}^{\infty} \cos(\omega_\alpha \tau)\cos(\omega_\alpha(t-\tau))d\tau, \\
& \quad (|t-\tau| \leq T) \cap (|\tau| \leq T). \\
&= \int_{-\infty}^{\infty} \frac{\cos(\omega_\alpha \tau - \omega_\alpha t + \omega_\alpha \tau) + \cos(\omega_\alpha \tau + \omega_\alpha t - \omega_\alpha \tau)}{2} d\tau, \\
& \quad (|t-\tau| \leq T) \cap (|\tau| \leq T). \\
&= \int_{-\infty}^{\infty} \frac{\cos(\omega_\alpha t)}{2} d\tau + \int_{-\infty}^{\infty} \frac{\cos(2\omega_\alpha \tau - \omega_\alpha t)}{2} d\tau, \qquad \text{(B.4a)} \\
& \quad (|t-\tau| \leq T) \cap (|\tau| \leq T).
\end{aligned}$$

The non-trivial regions of t in (B.4a) are: $-2T \leq t \leq 0$ and $0 \leq t \leq 2T$.

$$
\begin{aligned}
y'_{11}(t) &= \begin{cases}
\int_{-T}^{t+T} \frac{\cos(\omega_\alpha t)}{2} d\tau + \int_{-T}^{t+T} \frac{\cos(2\omega_\alpha \tau - \omega_\alpha t)}{2} d\tau, & -2T \le t \le 0 \\
\int_{t-T}^{T} \frac{\cos(\omega_\alpha t)}{2} d\tau + \int_{t-T}^{T} \frac{\cos(2\omega_\alpha \tau - \omega_\alpha t)}{2} d\tau, & 0 \le t \le 2T \\
0, & \text{Otherwise}
\end{cases} \\
&= \begin{cases}
\frac{\cos(\omega_\alpha t)}{2} \int_{-T}^{t+T} d\tau + \int_{-T}^{t+T} \frac{\cos(2\omega_\alpha \tau - \omega_\alpha t)}{2} d\tau, & -2T \le t \le 0 \\
\frac{\cos(\omega_\alpha t)}{2} \int_{t-T}^{T} d\tau + \int_{t-T}^{T} \frac{\cos(2\omega_\alpha \tau - \omega_\alpha t)}{2} d\tau, & 0 \le t \le 2T \\
0, & \text{Otherwise}
\end{cases} \\
&= \begin{cases}
\frac{\cos(\omega_\alpha t)}{2} \tau \Big|_{-T}^{t+T} + \frac{\sin(2\omega_\alpha \tau - \omega_\alpha t)}{4\omega_\alpha} \Big|_{-T}^{t+T}, & -2T \le t \le 0 \\
\frac{\cos(\omega_\alpha t)}{2} \tau \Big|_{t-T}^{T} + \frac{\sin(2\omega_\alpha \tau - \omega_\alpha t)}{4\omega_\alpha} \Big|_{t-T}^{T}, & 0 \le t \le 2T \\
0, & \text{Otherwise}
\end{cases} \\
&= \begin{cases}
\frac{\cos(\omega_\alpha t)}{2} (t + T + T) + \frac{\sin(2\omega_\alpha t + 2\omega_\alpha T - \omega_\alpha t) - \sin(-2\omega_\alpha T - \omega_\alpha t)}{4\omega_\alpha}, & -2T \le t \le 0 \\
\frac{\cos(\omega_\alpha t)}{2} (T - t + T) + \frac{\sin(2\omega_\alpha T - \omega_\alpha t) - \sin(2\omega_\alpha t - 2\omega_\alpha T - \omega_\alpha t)}{4\omega_\alpha}, & 0 \le t \le 2T \\
0, & \text{Otherwise}
\end{cases}
\end{aligned}
$$

$$= \begin{cases} \frac{\cos(\omega_\alpha t)}{2}(t+2T) + \frac{\sin(\omega_\alpha t + \frac{\pi}{2T}2T) - \sin(-\omega_\alpha t - \frac{\pi}{2T}2T)}{4\omega_\alpha}, & -2T \le t \le 0 \\ \frac{\cos(\omega_\alpha t)}{2}(-t+2T) + \frac{\sin(\frac{\pi}{2T}2T - \omega_\alpha t) - \sin(\omega_\alpha t - \frac{\pi}{2T}2T)}{4\omega_\alpha}, & 0 \le t \le 2T \\ 0, & \text{Otherwise} \end{cases}$$

$$= \begin{cases} \frac{\cos(\omega_\alpha t)}{2}(t+2T) + \frac{\sin(\omega_\alpha t + \pi) + \sin(\omega_\alpha t + \pi)}{4\omega_\alpha}, & -2T \le t \le 0 \\ \frac{\cos(\omega_\alpha t)}{2}(-t+2T) + \frac{\sin(\pi - \omega_\alpha t) + \sin(\pi - \omega_\alpha t)}{4\omega_\alpha}, & 0 \le t \le 2T \\ 0, & \text{Otherwise} \end{cases}$$

$$= \begin{cases} \frac{\cos(\omega_\alpha t)}{2}(t+2T) - \frac{\sin(\omega_\alpha t)}{2\omega_\alpha}, & -2T \le t \le 0 \\ \frac{\cos(\omega_\alpha t)}{2}(-t+2T) + \frac{\sin(\omega_\alpha t)}{2\omega_\alpha}, & 0 \le t \le 2T \\ 0, & \text{Otherwise} \end{cases}$$

$$= \begin{cases} \frac{\cos(\omega_\alpha t)}{2}(2T - |t|) + \frac{\sin(\omega_\alpha |t|)}{2\omega_\alpha}, & |t| \le 2T. \end{cases} \tag{B.6}$$

Convolution of p_2 with p_2.

$$\begin{aligned} y'_{22}(t) &= p_2(t) * p_2(t) \\ &= \int_{-\infty}^{\infty} p_2(\tau) p_2(t-\tau) d\tau, \end{aligned} \tag{B.7}$$

where

$$\begin{aligned} p_2(t-\tau) &= \sin(\omega_\alpha(t-\tau)), \quad |t-\tau| \le T \\ &= \sin(\omega_\alpha t - \omega_\alpha \tau), \quad |t-\tau| \le T. \end{aligned}$$

We use trigonometric identities (B.1d) in (B.7) to simplify.

$$\begin{aligned}
y'_{22}(t) &= \int_{-\infty}^{\infty} \sin(\omega_\alpha \tau)\sin(\omega_\alpha(t-\tau))d\tau, \\
&\quad (|t-\tau| \leq T) \cap (|\tau| \leq T). \\
&= \int_{-\infty}^{\infty} \frac{\cos(\omega_\alpha \tau - \omega_\alpha t + \omega_\alpha \tau) - \cos(\omega_\alpha \tau - \omega_\alpha t + \omega_\alpha \tau)}{2} d\tau, \\
&\quad (|t-\tau| \leq T) \cap (|\tau| \leq T). \\
&= -\int_{-\infty}^{\infty} \frac{\cos(\omega_\alpha t)}{2} d\tau + \int_{-\infty}^{\infty} \frac{\cos(2\omega_\alpha \tau - \omega_\alpha t)}{2} d\tau \qquad \text{(B.9a)} \\
&\quad (|t-\tau| \leq T) \cap (|\tau| \leq T).
\end{aligned}$$

The non-trivial regions of t in (B.9a) are: $-2T \leq t \leq 0$ and $0 \leq t \leq 2T$.

$$
\begin{aligned}
y'_{22}(t) &= \begin{cases} -\int_{-T}^{t+T} \frac{\cos(\omega_\alpha t)}{2} d\tau + \int_{-T}^{t+T} \frac{\cos(2\omega_\alpha \tau - \omega_\alpha t)}{2} d\tau, & -2T \leq t \leq 0 \\ -\int_{t-T}^{T} \frac{\cos(\omega_\alpha t)}{2} d\tau + \int_{t-T}^{T} \frac{\cos(2\omega_\alpha \tau - \omega_\alpha t)}{2} d\tau, & 0 \leq t \leq 2T \\ 0, & \text{Otherwise} \end{cases} \\
&= \begin{cases} -\frac{\cos(\omega_\alpha t)}{2} \int_{-T}^{t+T} d\tau + \int_{-T}^{t+T} \frac{\cos(2\omega_\alpha \tau - \omega_\alpha t)}{2} d\tau, & -2T \leq t \leq 0 \\ -\frac{\cos(\omega_\alpha t)}{2} \int_{t-T}^{T} d\tau + \int_{t-T}^{T} \frac{\cos(2\omega_\alpha \tau - \omega_\alpha t)}{2} d\tau, & 0 \leq t \leq 2T \\ 0, & \text{Otherwise} \end{cases} \\
&= \begin{cases} -\frac{\cos(\omega_\alpha t)}{2} \tau \Big|_{-T}^{t+T} + \frac{\sin(2\omega_\alpha \tau - \omega_\alpha t)}{4\omega_\alpha} \Big|_{-T}^{t+T}, & -2T \leq t \leq 0 \\ -\frac{\cos(\omega_\alpha t)}{2} \tau \Big|_{t-T}^{T} + \frac{\sin(2\omega_\alpha \tau - \omega_\alpha t)}{4\omega_\alpha} \Big|_{t-T}^{T}, & 0 \leq t \leq 2T \\ 0, & \text{Otherwise} \end{cases} \\
&= \begin{cases} -\frac{\cos(\omega_\alpha t)}{2} (t + T + T) + \frac{\sin(2\omega_\alpha t + 2\omega_\alpha T - \omega_\alpha t) - \sin(-2\omega_\alpha T - \omega_\alpha t)}{4\omega_\alpha}, & -2T \leq t \leq 0 \\ -\frac{\cos(\omega_\alpha t)}{2} (T - t + T) + \frac{\sin(2\omega_\alpha T - \omega_\alpha t) - \sin(2\omega_\alpha t - 2\omega_\alpha T - \omega_\alpha t)}{4\omega_\alpha}, & 0 \leq t \leq 2T \\ 0, & \text{Otherwise} \end{cases}
\end{aligned}
$$

$$= \begin{cases} -\frac{\cos(\omega_\alpha t)}{2}(t+2T) + \frac{\sin(\omega_\alpha t + \frac{\pi}{2T}2T) - \sin(-\omega_\alpha t - \frac{\pi}{2T}2T)}{4\omega_\alpha}, & -2T \leq t \leq 0 \\ -\frac{\cos(\omega_\alpha t)}{2}(-t+2T) + \frac{\sin(\frac{\pi}{2T}2T - \omega_\alpha t) - \sin(\omega_\alpha t - \frac{\pi}{2T}2T)}{4\omega_\alpha}, & 0 \leq t \leq 2T \\ 0, & \text{Otherwise} \end{cases}$$

$$= \begin{cases} -\frac{\cos(\omega_\alpha t)}{2}(t+2T) + \frac{\sin(\omega_\alpha t + \pi) + \sin(\omega_\alpha t + \pi)}{4\omega_\alpha}, & -2T \leq t \leq 0 \\ -\frac{\cos(\omega_\alpha t)}{2}(-t+2T) + \frac{\sin(\pi - \omega_\alpha t) + \sin(\pi - \omega_\alpha t)}{4\omega_\alpha}, & 0 \leq t \leq 2T \\ 0, & \text{Otherwise} \end{cases}$$

$$= \begin{cases} -\frac{\cos(\omega_\alpha t)}{2}(t+2T) - \frac{\sin(\omega_\alpha t)}{2\omega_\alpha}, & -2T \leq t \leq 0 \\ -\frac{\cos(\omega_\alpha t)}{2}(-t+2T) + \frac{\sin(\omega_\alpha t)}{2\omega_\alpha}, & 0 \leq t \leq 2T \\ 0, & \text{Otherwise} \end{cases}$$

$$= \begin{cases} -\frac{\cos(\omega_\alpha t)}{2}(2T - |t|) + \frac{\sin(\omega_\alpha |t|)}{2\omega_\alpha}, & |t| \leq 2T. \end{cases} \tag{B.11}$$

Third Part Convolution between p_1 and p_2.

$$y'_{12}(t) = \int_{-\infty}^{\infty} p_1(\tau) p_2(t-\tau) d\tau \tag{B.12}$$

$$y'_{21}(t) = \int_{-\infty}^{\infty} p_2(\tau) p_1(t-\tau) d\tau. \tag{B.13}$$

Notice that equation (B.12) is equal to (B.13) becuase of convolution properties.

$$y'_{21}(t) = y'_{12}(t). \tag{B.14}$$

Now, we use trigonometric identities (B.1e) in (B.12) to simplify.

$$\begin{aligned}
y'_{12}(t) &= \int_{-\infty}^{\infty} \cos(\omega_\alpha \tau)\sin(\omega_\alpha(t-\tau))d\tau, \\
&\quad (|t-\tau| \le T) \cap (|\tau| \le T). \\
&= \int_{-\infty}^{\infty} \frac{\sin(\omega_\alpha\tau + \omega_\alpha t - \omega_\alpha\tau) - \sin(\omega_\alpha\tau - \omega_\alpha t + \omega_\alpha\tau)}{2} d\tau, \\
&\quad (|t-\tau| \le T) \cap (|\tau| \le T). \\
&= \int_{-\infty}^{\infty} \frac{\sin(\omega_\alpha t)}{2} d\tau - \int_{-\infty}^{\infty} \frac{\sin(2\omega_\alpha\tau - \omega_\alpha t)}{2} d\tau \qquad \text{(B.15a)} \\
&\quad (|t-\tau| \le T) \cap (|\tau| \le T).
\end{aligned}$$

Equation(B.15a) is a simplified version of (B.12).

The non-trivial regions of t are: $-2T \le t \le 0$ and $0 \le t \le 2T$.

$$
\begin{aligned}
y'_{12}(t) &= \begin{cases} \int_{-T}^{t+T} \frac{\sin(\omega_\alpha t)}{2} d\tau - \int_{-T}^{t+T} \frac{\sin(2\omega_\alpha \tau - \omega_\alpha t)}{2} d\tau, & -2T \le t \le 0 \\ \int_{t-T}^{T} \frac{\sin(\omega_\alpha t)}{2} d\tau - \int_{t-T}^{T} \frac{\sin(2\omega_\alpha \tau - \omega_\alpha t)}{2} d\tau, & 0 \le t \le 2T \\ 0, & \text{Otherwise} \end{cases} \\
&= \begin{cases} \frac{\sin(\omega_\alpha t)}{2} \int_{-T}^{t+T} d\tau - \int_{-T}^{t+T} \frac{\sin(2\omega_\alpha \tau - \omega_\alpha t)}{2} d\tau, & -2T \le t \le 0 \\ \frac{\sin(\omega_\alpha t)}{2} \int_{t-T}^{T} d\tau - \int_{t-T}^{T} \frac{\sin(2\omega_\alpha \tau - \omega_\alpha t)}{2} d\tau, & 0 \le t \le 2T \\ 0, & \text{Otherwise} \end{cases} \\
&= \begin{cases} \frac{\sin(\omega_\alpha t)}{2} \tau \Big|_{-T}^{t+T} + \frac{\cos(2\omega_\alpha \tau - \omega_\alpha t)}{4\omega_\alpha} \Big|_{-T}^{t+T}, & -2T \le t \le 0 \\ \frac{\sin(\omega_\alpha t)}{2} \tau \Big|_{t-T}^{T} + \frac{\cos(2\omega_\alpha \tau - \omega_\alpha t)}{4\omega_\alpha} \Big|_{t-T}^{T}, & 0 \le t \le 2T \\ 0, & \text{Otherwise} \end{cases} \\
&= \begin{cases} \frac{\sin(\omega_\alpha t)}{2} (t + T + T) + \frac{\cos(2\omega_\alpha t + 2\omega_\alpha T - \omega_\alpha t) - \cos(-2\omega_\alpha T - \omega_\alpha t)}{4\omega_\alpha}, & -2T \le t \le 0 \\ \frac{\sin(\omega_\alpha t)}{2} (T - t + T) + \frac{\cos(2\omega_\alpha T - \omega_\alpha t) - \cos(2\omega_\alpha t - 2\omega_\alpha T - \omega_\alpha t)}{4\omega_\alpha}, & 0 \le t \le 2T \\ 0, & \text{Otherwise} \end{cases}
\end{aligned}
$$

$$
\begin{aligned}
&= \begin{cases} \frac{\sin(\omega_\alpha t)}{2}(t+2T) + \frac{\cos(\omega_\alpha t + \frac{\pi}{2T}2T) - \cos(-\omega_\alpha t - \frac{\pi}{2T}2T)}{4\omega_\alpha}, & -2T \leq t \leq 0 \\ \frac{\sin(\omega_\alpha t)}{2}(-t+2T) + \frac{\cos(\frac{\pi}{2T}2T - \omega_\alpha t) - \cos(\omega_\alpha t - \frac{\pi}{2T}2T)}{4\omega_\alpha}, & 0 \leq t \leq 2T \\ 0, & \text{Otherwise} \end{cases} \\
&= \begin{cases} \frac{\sin(\omega_\alpha t)}{2}(t+2T) + \frac{\cos(\omega_\alpha t + \pi) - \cos(\omega_\alpha t + \pi)}{4\omega_\alpha}, & -2T \leq t \leq 0 \\ \frac{\sin(\omega_\alpha t)}{2}(-t+2T) + \frac{\cos(\pi - \omega_\alpha t) - \cos(\pi - \omega_\alpha t)}{4\omega_\alpha}, & 0 \leq t \leq 2T \\ 0, & \text{Otherwise} \end{cases} \\
&= \begin{cases} \frac{\sin(\omega_\alpha t)}{2}(t+2T), & -2T \leq t \leq 0 \\ \frac{\sin(\omega_\alpha t)}{2}(-t+2T), & 0 \leq t \leq 2T \\ 0, & \text{Otherwise} \end{cases} \\
&= \begin{cases} -\frac{\sin(\omega_\alpha t)}{2}(|t| - 2T), & |t| \leq 2T. \end{cases}
\end{aligned} \tag{B.17}
$$

The output of the matched filter is proportional to a time-shifted correlation function. Instead of using a bank of 4 correlators to generate the coefficients of the geometry of the signal, we use a bank of 4 linear filters $h_k(t) = p_k(t_o - t)$, $k = 1, 2, 3, 4$ and observe the output at the instant T. As pulse shape signals for cosine carrier and sine carrier are similar, we can use: $h_1(t) = h_3(t) = p_1(t_o - t)$ and $h_2(t) = h_4(t) = p_2(t_o - t)$.

The matched filter use in this manuscript forces the output signal to be proportional to the coefficients of the signal's geometry more obvious at the instant T.

Notice that pulse 1 is an even function $p_1(-t) = p_1(t)$ and the pulse 2 is an odd function $-p_2(-t) = p_2(t)$, and consider $\delta(t)$ is an impulse function where $\delta(t) = \delta(-t)$.

Fourier Transform properties use in this procedure are:

$$\mathcal{F}[p_1(t)] = P_1(f) \tag{B.18a}$$

$$\mathcal{F}[p_2(t)] = P_2(f) \tag{B.18b}$$

$$\mathcal{F}[p_1(-t)] = P_1(f) \tag{B.18c}$$

$$\mathcal{F}[p_2(-t)] = -P_2(f) \tag{B.18d}$$

$$\mathcal{F}[p_1(t_o - t)] = P_1(f)e^{-j2\pi f t_o} \tag{B.18e}$$

$$\mathcal{F}[p_2(t_o - t)] = -P_2(f)e^{-j2\pi f t_o}. \tag{B.18f}$$

We defined the following properties given that $*$ is the convolution operation :

$$p_1(t) * p_2(t) = p_1(-t) * p_2(t) = -p_1(t) * p_2(-t) \tag{B.19a}$$

$$\mathcal{F}^{-1}[P_1(f)P_2(f)] = p_1(t) * p_2(t) = p_2(t) * p_1(t) \tag{B.19b}$$

$$\mathcal{F}^{-1}[P_1(f)P_1(f)] = p_1(t) * p_1(t) \tag{B.19c}$$

$$p_1(t) * \delta(t - t_o) = p_1(t - t_o) \tag{B.19d}$$

$$p_2(t) * \delta(t - t_o) = p_2(t - t_o) \tag{B.19e}$$

$$p_1(t) * p_1(t) = p_1(-t) * p_1(-t) \tag{B.19f}$$

$$p_2(t) * p_2(t) = p_2(-t) * p_2(-t) \tag{B.19g}$$

$$\mathcal{F}^{-1}[P_2(f)P_2(f)] = p_2(t) * p_2(t). \tag{B.19h}$$

The equations derive below are used to derive the general equation used to plot the output of the matched filter.

$$y_{11}(t) = p_1(t) * h_1(t)$$

$$y_{11}(t) = p_1(t) * p_1(t_o - t) \tag{B.20a}$$

Taking the Fourier transform of (B.20a) and using properties (B.18e), (B.18e)

$$\begin{aligned}
\mathcal{F}[y_{11}(t)] &= \mathcal{F}[p_1(t)]\mathcal{F}[p_1(t_o - t)] && \text{(B.21a)}\\
&= P_1(f)\mathcal{F}[p_1(t_o - t)] && \text{(B.21b)}\\
&= P_1(f)P_1(f)e^{-j2\pi f t_o}. && \text{(B.21c)}
\end{aligned}$$

Taking the inverse Fourier transform of (B.21c) and using properties (B.19c), (B.19d), we make (B.20a) function of (B.6) delayed

$$\begin{aligned}
\mathcal{F}^{-1}[\mathcal{F}[y_{11}(t)]] &= \mathcal{F}^{-1}[P_1(f)P_1(f)e^{j2\pi f t_o}]\\
y_{11}(t) &= \mathcal{F}^{-1}[P_1(f)P_1(f)e^{j2\pi f t_o}]\\
&= p_1(t) * p_1(t) * \partial(t - t_o)\\
&= y'_{11}(t) * \delta(t - t_o)\\
&= y'_{11}(t - t_o). && \text{(B.22)}
\end{aligned}$$

Now for the sine pulse

$$\begin{aligned}
y_{22}(t) &= p_2(t) * h_2(t)\\
y_{22}(t) &= p_2(t) * p_2(t_o - t). && \text{(B.23a)}
\end{aligned}$$

Taking the Fourier transform of (B.23a) and using properties (B.18b), (B.18f).

$$\begin{aligned}
\mathcal{F}[y_{22}(t)] &= \mathcal{F}[p_2(t)]\mathcal{F}[p_2(t_o - t)] && \text{(B.24a)}\\
&= P_2(f)\mathcal{F}[p_2(t_o - t)] && \text{(B.24b)}\\
&= P_2(f)(-P_2(f)e^{-j2\pi f t_o}). && \text{(B.24c)}
\end{aligned}$$

Taking the inverse Fourier transform of (B.24c) and using properties (B.19h), (B.19e), we make (B.23a) function of (B.11) delayed.

$$\begin{aligned}
\mathcal{F}^{-1}[\mathcal{F}[y_{22}(t)]] &= -\mathcal{F}^{-1}[P_2(f)P_2(f)e^{-j2\pi f t_o}] && \text{(B.25)}\\
y_{22}(t) &= -\mathcal{F}^{-1}[P_2(f)P_2(f)]\mathcal{F}^{-1}[e^{-j2\pi f t_o}] && \text{(B.26)}\\
y_{22}(t) &= -p_2(t) * p_2(t) * \delta(t-t_o) && \text{(B.27)}\\
y_{22}(t) &= -y'_{22}(t) * \delta(t-t_o) && \text{(B.28)}\\
y_{22}(t) &= -y'_{22}(t-t_o). && \text{(B.29)}
\end{aligned}$$

Now for the cosine pulse with the sine pulse

$$\begin{aligned}
y_{12}(t) &= p_1(t) * h_2(t) && \text{(B.30a)}\\
y_{12}(t) &= p_1(t) * p_2(t_o - t). && \text{(B.30b)}
\end{aligned}$$

Taking the Fourier transform of (B.30b) and using properties (B.18b), (B.18f)

$$\begin{aligned}
\mathcal{F}[y_{12}(t)] &= \mathcal{F}[p_1(t)]\mathcal{F}[p_2(t_o - t)] && \text{(B.31a)}\\
&= P_1(f)\mathcal{F}[p_2(t_o - t)] && \text{(B.31b)}\\
&= -P_1(f)P_2(f)e^{-j2\pi f t_o}. && \text{(B.31c)}
\end{aligned}$$

Taking the inverse Fourier transform of (B.31c) and using properties (B.19b), (B.19e), we make (B.30b) function of (B.17) delayed

$$\begin{aligned}
\mathcal{F}^{-1}[\mathcal{F}[y_{12}(t)]] &= -\mathcal{F}^{-1}[P_1(f)P_2(f)e^{-j2\pi f t_o}] && \text{(B.32)}\\
y_{12}(t) &= -\mathcal{F}^{-1}[P_1(f)P_2(f)]\mathcal{F}^{-1}[e^{-j2\pi f t_o}] && \text{(B.33)}\\
&= -p_1(t) * p_2(t) * \delta(t-t_o) && \text{(B.34)}\\
&= -y'_{12}(t) * \delta(t-t_o) && \text{(B.35)}\\
&= -y'_{12}(t-t_o). && \text{(B.36)}
\end{aligned}$$

Now for the sine pulse with the cosine pulse

$$\begin{aligned} y_{21}(t) &= p_2(t) * h_1(t) && \text{(B.37a)} \\ y_{21}(t) &= p_2(t) * p_1(t_o - t). && \text{(B.37b)} \end{aligned}$$

Taking the Fourier transform of (B.37b) and using properties (B.18b), (B.18e)

$$\begin{aligned} \mathcal{F}[y_{21}(t)] &= \mathcal{F}[p_2(t)]\mathcal{F}[p_1(t_o - t)] && \text{(B.38a)} \\ &= P_2(f)\mathcal{F}[p_1(t_o - t)] && \text{(B.38b)} \\ &= P_2(f)P_1(f)e^{-j2\pi f t_o}. && \text{(B.38c)} \end{aligned}$$

Taking the inverse Fourier transform of (B.38c) and using properties (B.19b), (B.19e), we make (B.37b) function of (B.17) delayed

$$\begin{aligned} \mathcal{F}^{-1}[\mathcal{F}[y_{21}(t)]] &= \mathcal{F}^{-1}[P_2(f)P_1(f)e^{-j2\pi f t_o}] && \text{(B.39)} \\ y_{21}(t) &= \mathcal{F}^{-1}[P_2(f)P_1(f)]\mathcal{F}^{-1}[e^{-j2\pi f t_o}] && \text{(B.40)} \\ &= p_2(t) * p_1(t) * \delta(t - t_o) && \text{(B.41)} \\ &= y'_{21}(t) * \delta(t - t_o) && \text{(B.42)} \\ &= y'_{21}(t - t_o) && \text{(B.43)} \\ &= y'_{12}(t - t_o). && \text{(B.44)} \end{aligned}$$

Before we proceed to delay $y'_{11}(t), y'_{22}(t), y'_{12}(t), y'_{21}(t)$ functions, we are going summarize the prime functions in a more simple expression using $i, j = 1, 2$.

$$y'_{11}(t) = \begin{cases} \frac{\cos(\omega_\alpha t)}{2}(2T - |t|) + \frac{\sin(\omega_\alpha |t|)}{2\omega_\alpha}, & |t| \le 2T \end{cases}$$

$$y'_{22}(t) = \begin{cases} -\frac{\cos(\omega_\alpha t)}{2}(2T - |t|) + \frac{\sin(\omega_\alpha |t|)}{2\omega_\alpha}, & |t| \le 2T \end{cases}$$

$$y'_{12}(t) = \begin{cases} -\frac{\sin(\omega_\alpha t)}{2}(|t| - 2T), & |t| \le 2T \end{cases}$$

$$y'_{21}(t) = \begin{cases} -\frac{\sin(\omega_\alpha t)}{2}(|t| - 2T), & |t| \leq 2T \end{cases}$$

By finding some similarities and using some phase shifts we can simplify the four equations above. The final expression is:

$$y'_{ij}(t) = \begin{cases} (-1)^{(i-1)(j-1)} \frac{\cos(\omega_\alpha t - \frac{\pi}{2}|i-j|)}{2}(2T - |t|) + \frac{\sin(\omega_\alpha |t|)}{2\omega_\alpha} \left|3 - i - j\right|, & |t| \leq 2T \end{cases} \tag{B.45a}$$

Finally,

$$\begin{aligned} y_1(t) &= p_1(t) * h_1(t) + p_2(t) * h_1(t) \\ &= y'_{11}(t-T) + y'_{12}(t-T) && \text{(B.46a)} \\ y_2(t) &= p_1(t) * h_2(t) + p_2(t) * h_2(t) \\ &= -y'_{12}(t-T) - y'_{22}(t-T) && \text{(B.46b)} \end{aligned}$$

Appendix C Matlab Code for received signals without filter

```
%% Initialization of variables

clc

clear

T=1;

dt=.01;

%-------------------------------------

wa=pi/(2*T);        %Pulse Low frequency

%-----------------------------------

t=-T:dt:T-dt; %Time interval

n=2;

fc=(n/4*T);         %Carrier Frequency


%----Pulses without Filtering----------

block=rectangularPulse(-T,T,t);

block(t==1)=1;

block(t==-1)=1;

p1=cos(wa*t).*block;

p2=sin(wa*t).*block;


%% Convolution

figure(1)

tx1=linspace(-1*T,1*T,length(p1)+length(p1)-1);

plot(tx1,conv(p2,p2)/100,tx1,conv(p1,p1)/100,t,p2)

grid


%% Sine Cosine
```

```
%Y12 prime which is the convolution of p1 and p2 without shift
t1=-2*T:dt:0;
t2=0:dt:2*T;

y12t1=sin(wa*t1).*(t1+2*T)*0.5;
y12t2=(2*T-t2).*sin(wa*t2)*0.5;

y12=[y12t1 y12t2];
t12=[t1 t2];
figure
plot(conv(p1,p2))
figure
plot(t12,y12)

tx12=-2*T:0.01:2*T;
y12db=-0.5*sin(wa*(tx12)).*(abs(tx12)-2*T);
figure;
plot(tx12,y12db);


%% cosine cosine
%Y11 prime which is the convolution of p1 and p2 without shift
t1=-2*T:dt:0;
t2=0:dt:2*T;
y11t1=cos(wa*t1).*(t1+2*T)*0.5-(sin(wa*t1)/(2*wa));
y11t2=cos(wa*t2).*(2*T-t2)*0.5-(sin(wa*t1)/(2*wa));
y11=[y11t1 y11t2];
t11=[t1 t2];
figure
```

```
plot(conv(p1,p1)/100)

figure

plot(t11,y11)


%% sine sine

%Y22 prime which is the convolution of p1 and p2 without shift

t1=-2*T:dt:0;

t2=0:dt:2*T;


y22t1=-cos(wa*t1).*(t1+2*T)*0.5-(sin(wa*t1)/(2*wa));

y22t2=-cos(wa*t2).*(2*T-t2)*0.5+(sin(wa*t2)/(2*wa));


y22=[y22t1 y22t2];

t22=[t1 t2];

figure

plot(conv(p2,p2)/100)

figure

plot(t22,y22)



%%

%Dr. B simplifaction

tx12=-2*T:0.01:2*T; %time for theoretical

tx1=linspace(-2*T,2*T,length(p1)+length(p1)-1); %time for convolution

y12db=-0.5*sin(wa*(tx12)).*(abs(tx12)-2*T);

y11db=(0.5*cos(wa*tx12).*(2*T-abs(tx12)))+(sin(wa*abs(tx12))/(2*wa));

y22db=-(0.5*cos(wa*tx12).*(2*T-abs(tx12)))+(sin(wa*abs(tx12))/(2*wa));


figure(1);
```

```
subplot(3,1,1)
plot(tx12,y11db);
subplot(3,1,2)
plot(tx12,y22db);
subplot(3,1,3)
plot(tx12,y12db)

%% Matlab convolution
figure(1);
subplot(3,1,1)
plot(tx1,conv(p1,p1)/100);
ylim([0 1]);
subplot(3,1,2)
plot(tx1,conv(p2,p2)/100);
subplot(3,1,3)
plot(tx1,conv(p1,p2)/100)



%% General formula
t=-2*T:0.01:2*T; %time for theoretical
figure(2)
        i=1;j=1;
        y=(-1)^(i+j-(i*j)+3)*cos(wa*t-(pi/2)*abs(i-j)).*(1*T-0.5*abs(t))...
            +(sin(wa*abs(t))/(2*wa))*(abs(3-(i+j)));
        subplot(3,1,1)
        plot(t,y)
        i=2;j=2;
        y=(-1)^(i+j-(i*j)+3).*cos(wa*t-(pi/2)*abs(i-j)).*(1*T-0.5*abs(t))...
            +(sin(wa*abs(t))/(2*wa))*(abs(3-(i+j)));
```

```
        subplot(3,1,2)
        plot(t,y)
        i=1;j=2;
        y=(-1)^(i+j-(i*j)+3).*cos(wa*t-(pi/2)*abs(i-j)).*(1*T-0.5*abs(t))...
            +(sin(wa*abs(t))/(2*wa))*(abs(3-(i+j)));
        subplot(3,1,3)
        plot(t,y)

%% General formula Dr B
t=-2*T:0.01:2*T; %time for theoretical
figure(2)
        i=1;j=1;
        y=(-1)^((i-1)*(j-1))*cos(wa*t-(pi/2)*abs(i-j)).*(1*T-0.5*abs(t))...
            +(sin(wa*abs(t))/(2*wa))*(abs(3-(i+j)));
        subplot(3,1,1)
        plot(t,y)
        i=2;j=2;
        y=(-1)^((i-1)*(j-1)).*cos(wa*t-(pi/2)*abs(i-j)).*(1*T-0.5*abs(t))...
            +(sin(wa*abs(t))/(2*wa))*(abs(3-(i+j)));
        subplot(3,1,2)
        plot(t,y)
        i=1;j=2;
        y=(-1)^((i-1)*(j-1)).*cos(wa*t-(pi/2)*abs(i-j)).*(1*T-0.5*abs(t))...
            +(sin(wa*abs(t))/(2*wa))*(abs(3-(i+j)));
        subplot(3,1,3)
        plot(t,y)

%% General formula shifted by T
t=-1*T:0.01:3*T; %time for theoretical
```

```
figure(3)

        i=1;j=1;

        y=(-1)^((i-1)*(j-1))*cos(wa*(t-T)-(pi/2)*abs(i-j)).*(1*T-0.5*abs(t-T))...

            +(sin(wa*abs(t-T))/(2*wa))*(abs(3-(i+j)));

        y11=y;

        subplot(3,1,1)

        plot(t,y)

        xlim([-1 3])

        ylim([-1 1])

        i=2;j=2;

        y=(-1)^((i-1)*(j-1)).*cos(wa*(t-T)-(pi/2)*abs(i-j)).*(1*T-0.5*abs(t-T))...

            +(sin(wa*abs(t-T))/(2*wa))*(abs(3-(i+j)));

        subplot(3,1,2)

        y22=y;

        plot(t,y)

        xlim([-1 3])

        ylim([-1 1])

        i=1;j=2;

        y=(-1)^((i-1)*(j-1)).*cos(wa*(t-T)-(pi/2)*abs(i-j)).*(1*T-0.5*abs(t-T))...

            +(sin(wa*abs(t-T))/(2*wa))*(abs(3-(i+j)));

        y12=y;

        subplot(3,1,3)

        plot(t,y)

        xlim([-1 3])

        ylim([-1 1])


        figure(4)

        plot(t,y11+y12)

        grid
```

```
        figure(5)

        plot(t,-y22-y12)

        grid


%%

figure(4)

%match filter matlab

t1=-3*T:dt:4*T-dt;

block=rectangularPulse(-T,T,1*T-t1);

dummy1=1*T-t1;

block(dummy1==1)=1;

block(dummy1==-1)=1;

p1matchf=cos(wa*(1*T-t1)).*block;

p2matchf=sin(wa*(1*T-t1)).*block;


tmatch=linspace(-4*T,5*T,length(p1matchf)+length(p1)-1);

subplot(3,1,1)

plot(tmatch,conv(p1matchf,p1)/100)

xlim([-1 3])

ylim([-1 1])

subplot(3,1,2)

plot(tmatch,conv(p2matchf,p2)/100)

xlim([-1 3])

ylim([-1 1])

subplot(3,1,3)

plot(tmatch,conv(p1matchf,p2)/100)

xlim([-1 3])

ylim([-1 1])
```

```
%% Maltab convolution and comparison between values

plot(tx12,y12db,tx1,conv(p1,p2)/100);

figure(2)

plot(tx12,y22db,tx1,conv(p2,p2)/100);

figure(3)

plot(tx12,y11db,tx1,conv(p1,p1)/100)
```

Appendix D Constellation generation

```
% CEQQ16constellation
% Edit Bourgeois
% January 2011
%%%%%%%%%%%%%%%%%%%%%%%%%%%%%%%%%%%%%%%%%%%%%%%%%%%%%%%%%%%
% 4D CEQQPSK-Saha
S=[ 1 1 1 -1;
    1 1 -1 1;
    1 -1 1 1;
    1 -1 -1 -1;
    -1 -1 -1 1;
    -1 -1 1 -1;
    -1 1 -1 -1;
    -1 1 1 1];
C=[ 0 sqrt(2) sqrt(2) 0;
    0 sqrt(2) -sqrt(2) 0;
    sqrt(2) 0 0 sqrt(2);
    sqrt(2) 0 0 -sqrt(2);
    0 -sqrt(2) -sqrt(2) 0;
    0 -sqrt(2) sqrt(2) 0;
    -sqrt(2) 0 0 -sqrt(2);
    -sqrt(2) 0 0 sqrt(2)];
% Generate not-quite-cartesian product (i.e., all possible 16D points, not
% including mixed ones.  This is 16D-CEQQPSK constellation.
%initialize S16 and C16
S16=zeros(8*8*8*8,16);
C16=S16;
```

```
for i=1:8
    for j=1:8
        for k=1:8
            for l=1:8
                S16(l+(k-1)*8+(j-1)*64+(i-1)*64*8,1:16)=...
                [S(i,1:4) S(j,1:4) S(k,1:4) S(l,1:4)];
                C16(l+(k-1)*8+(j-1)*64+(i-1)*64*8,1:16)=...
                [C(i,1:4) C(j,1:4) C(k,1:4) C(l,1:4)];
            end
        end
    end
end
clear i j k l
% compute Hamming Distances (all possible)
S16dist=pdist(S16,'Hamming')*16;
C16dist=pdist(round(C16*100),'Hamming')*16;
SC16dist=pdist2(S16,round(C16*100),'Hamming')*16;
% Sort and count how many of each possible distance (H dist distribution)
S16distu = unique(S16dist);
S16distu=sort(S16distu);
C16distu = unique(C16dist);
C16distu=sort(C16distu);
SC16distu = unique(SC16dist);
SC16distu=sort(SC16distu);
% Comments of importance:
% 1) For Rayleigh Channels, it is the Hamming distance that matters
% 2) The HD among Saha's CEQQPSK points is twice as big (2) than for
% Carthwright's CEQQPSK points (due to the 0's).  This means that standard
% CEQQPSK with Saha's will perform better in Rayleigh fading thant
```

```
% Cartwright's CEQQPSK.  BAD NEWS.
% 3) When implementing TCM, we kept, on purpose, Saha's 16D and
% Cartwright's 16 D separately (i.e., different subsets) to avoid reducing
% the Euclidean distance (because Saha to Saha or Cart to Cart EDs are
% better than Saha to Cartwright's.
% 4) However, for fading, ED is not of primary concern, HD is.  So...
% it would be better to mix Saha's and Cartwright's 16 D points into the
% same subset, because the HD across the two CEQQPSK is better (much
% better, 16 actually) than within either Saha's or Cartwright's alone.
% 5) if a partition with mixed Saha/Cart points is possible, we should be
% able to achieve considerably better performance with mixed than with
% non-mixed.
% Partition MIXED
%
% Here is the entire 8192-point Expanded 16D QQPSK Constellation and HDs
E=[S16;C16];
[hd,ind] = pdist2(E,E,'hamming','smallest',2);
```

Appendix E Partition into 8 subsets - optimum in AWGN

The code that generates the 8 subsets E0 through E7 is given below.

```
% split16QQPSK.m
% By Dr. Kaminsky
% 19 July 2011
%%%%%%%%%%%%%%%%%%%%%%%%%%%%%%%%%%%%%%%%%%%%%%%%%%%%%%%%%%%
% Splits the 8192 16D points into several groups trying to keep
% MSED as large as possible.
% Case 1: 128 groups, 4 points in each, rate 6/7 encoder
% Case 2: 64 groups, 8 points in each, rate 5/6 encoder
% Case 3: 32 groups, 16 points in each, rate 4/5 encoder
% Case 4: 16 groups, 32 points in each, rate 3/4 encoder
% Case 5: 8 groups, 64 points in each, rate 2/3 encoder
% Case 6: 4 groups, 128 points in each, rate 1/2 encoder
% Case 7: 2 groups, 256 points in each, no encoder
% First create the 16D points, then group, and/or split
%%%%%%%%%%%%%%%%%%%%%%%%%%%%%%%%%%%%%%%%%%%%%%%%%%%%%%%%%
clear
s2=sqrt(2);
% 4D sublattices: 8 for each subset, of 1 point each
A=[1 1 1 -1];C=[1 1 -1 1];E=[1 -1 1 1];G=[1 -1 -1 -1];
B=[-1 -1 -1 1];D=[-1 -1 1 -1];F=[-1 1 -1 -1];H=[-1 1 1 1];
Ar=[0 s2 s2 0];Cr=[0 -s2 -s2 0];Er=[0 -s2 s2 0];Gr=[0 s2 -s2 0];
Br=[s2 0 0 s2];Dr=[s2 0 0 -s2];Fr=[-s2 0 0 s2];Hr=[-s2 0 0 -s2];
% 8D types: 64 types of 1 point each for each subset
T0=[A A]; T1= [A B]; T2 =[A C]; T3 = [A D];
T0r=[Ar Ar]; T1r= [Ar Br]; T2r =[Ar Cr]; T3r= [Ar Dr];
```

```
T4=[A E]; T5= [A F]; T6 =[A G]; T7 = [A H];
T4r=[Ar Er]; T5r= [Ar Fr]; T6r =[Ar Gr]; T7r = [Ar Hr];
T8=[B A]; T9= [B B]; T10 =[B C]; T11 = [B D];
T8r=[Br Ar]; T9r= [Br Br]; T10r =[Br Cr]; T11r= [Br Dr];
T12=[B E]; T13= [B F]; T14 =[B G]; T15 = [B H];
T12r=[Br Er]; T13r= [Br Fr]; T14r =[Br Gr]; T15r = [Br Hr];
T16=[C A]; T17= [C B]; T18 =[C C]; T19 = [C D];
T16r=[Cr Ar]; T17r= [Cr Br]; T18r =[Cr Cr]; T19r= [Cr Dr];
T20=[C E]; T21= [C F]; T22 =[C G]; T23 = [C H];
T20r=[Cr Er]; T21r= [Cr Fr]; T22r =[Cr Gr]; T23r = [Cr Hr];
T24=[D A]; T25= [D B]; T26 =[D C]; T27 = [D D];
T24r=[Dr Ar]; T25r= [Dr Br]; T26r =[Dr Cr]; T27r = [Dr Dr];
T28=[D E]; T29= [D F]; T30 =[D G]; T31 = [D H];
T28r=[Dr Er]; T29r= [Dr Fr]; T30r =[Dr Gr]; T31r = [Dr Hr];
T32=[E A]; T33= [E B]; T34 =[E C]; T35 = [E D];
T32r=[Er Ar]; T33r= [Er Br]; T34r =[Er Cr]; T35r = [Er Dr];
T36=[E E]; T37= [E F]; T38 =[E G]; T39 = [E H];
T36r=[Er Er]; T37r= [Er Fr]; T38r =[Er Gr]; T39r = [Er Hr];
T40=[F A]; T41= [F B]; T42 =[F C]; T43 = [F D];
T40r=[Fr Ar]; T41r= [Fr Br]; T42r =[Fr Cr]; T43r = [Fr Dr];
T44=[F E]; T45= [F F]; T46 =[F G]; T47 = [F H];
T44r=[Fr Er]; T45r= [Fr Fr]; T46r =[Fr Gr]; T47r = [Fr Hr];
T48=[G A]; T49= [G B]; T50 =[G C]; T51 = [G D];
T48r=[Gr Ar]; T49r= [Gr Br]; T50r =[Gr Cr]; T51r = [Gr Dr];
T52=[G E]; T53= [G F]; T54 =[G G]; T55 = [G H];
T52r=[Gr Er]; T53r= [Gr Fr]; T54r =[Gr Gr]; T55r = [Gr Hr];
T56=[H A]; T57= [H B]; T58 =[H C]; T59 = [H D];
T56r=[Hr Ar]; T57r= [Hr Br]; T58r =[Hr Cr]; T59r = [Hr Dr];
T60=[H E]; T61= [H F]; T62 =[H G]; T63 = [H H];
```

```
T60r=[Hr Er]; T61r= [Hr Fr]; T62r =[Hr Gr]; T63r = [Hr Hr];
% 8D sublattices: 32 sublattices of 2 points each, for each subset
s0=[T0; T9]; s1=[T18; T27]; s2=[T1; T8]; s3=[T19; T26];
s4=[T2 ;T11]; s5=[T17; T24]; s6=[T3; T10]; s7=[T16; T25];
s8=[T36; T45]; s9=[T54; T63]; s10=[T37; T44]; s11=[T55; T62];
s12=[T38 ;T47]; s13=[T53; T60]; s14=[T39; T46]; s15=[T52; T61];
s16=[T0; T45]; s17=[T18; T63]; s18=[T1; T44]; s19=[T19; T62];
s20=[T2 ;T47]; s21=[T17; T60]; s22=[T3; T46]; s23=[T16; T61];
s24=[T36; T9]; s25=[T54; T27]; s26=[T37; T8]; s27=[T55; T26];
s28=[T38 ;T11]; s29=[T53; T24]; s30=[T39; T10]; s31=[T52; T25];
s0r=[T0r; T9r]; s1r=[T18r; T27r]; s2r=[T1r; T8r]; s3r=[T19r; T26r];
s4r=[T2r ;T11r]; s5r=[T17r; T24r]; s6r=[T3r; T10r]; s7r=[T16r; T25r];
s8r=[T36r; T45r]; s9r=[T54r; T63r]; s10r=[T37r; T44r]; s11r=[T55r; T62r];
s12r=[T38r ;T47r]; s13r=[T53r; T60r]; s14r=[T39r; T46r]; s15r=[T52r; T61r];
s16r=[T0r; T45r]; s17r=[T18r; T63r]; s18r=[T1r; T44r]; s19r=[T19r; T62r];
s20r=[T2r ;T47r]; s21r=[T17r; T60r]; s22r=[T3r; T46r]; s23r=[T16r; T61r];
s24r=[T36r; T9r]; s25r=[T54r; T27r]; s26r=[T37r; T8r]; s27r=[T55r; T26r];
s28r=[T38r ;T11r]; s29r=[T53r; T24r]; s30r=[T39r; T10r]; s31r=[T52r; T25r];
% Case I
% 16D types:  1024 types for each subset, each with 4 points.
% This gives a total of 1024 subsets.
% These are the 1024 subsets of 4 points each for
% the encoder of rate 9/10.  The MSED is 16.
for k=0:31
   for m=0:31
for i=1:2
         for j=1:2
            eval(['t' num2str(k) '_' num2str(m) '(j+(i-1)*2,:)' ' =...
             [s' num2str(k) '(i,:)' ' ' 's' num2str(m) '(j,:)];']);
```

```
            eval(['t' num2str(k) '_' num2str(m) 'r' '(j+(i-1)*2,:)' ' =...
             [s' num2str(k) 'r' '(i,:)' ' ' 's' num2str(m) 'r' '(j,:)];']);
        end
end
   end
end
% Check MSED for the 1024 subsets of 4 points each
% and count how many are at that distance:
% There are 2, i.e. N(dfree=16) = 2
smallest1=100;smallest2=100;
for i=0:31
   for j=0:31
    eval(['temp1=sort(dist(t' num2str(i) '_'...
     num2str(j) ',transpose(t' num2str(i) '_' num2str(j) ')));']);
    eval(['temp2=sort(dist(t' num2str(i) '_'...
     num2str(j) 'r,transpose(t' num2str(i) '_' num2str(j) 'r)));']);
    temp1=temp1(:,1).*temp1(:,1);
    temp2=temp2(:,1).*temp2(:,1);
    eval(['nt' num2str(i) '_' num2str(j) '=sum(temp1>15.9 & temp1<16.1);'])
    eval(['ntr' num2str(i) '_' num2str(j) '=sum(temp2>15.9 & temp2<16.1);'])
end
end
% Case III:
% 16D sub-lattices: 256 for reach subset
% 256 sets for rate 7/8 encoder.  MSED = 16.
% for all these, the ED's are:
% 0    4 (14 times) 5.6569, so the MSED is still 16
%
S0=[t00;t11;t22;t33]; S0r=[t00r;t11r;t22r;t33r];
```

```
S1=[t01;t10;t23;t32];S1r=[t01r;t10r;t23r;t32r];

S2=[t02;t13;t20;t31];S2r=[t02r;t13r;t20r;t31r];

S3=[t03;t12;t21;t30];S3r=[t03r;t12r;t21r;t30r];

S4=[t44;t55;t66;t77];S4r=[t44r;t55r;t66r;t77r];

S5=[t45;t54;t67;t76];S5r=[t45r;t54r;t67r;t76r];

S6=[t46;t57;t64;t75];S6r=[t46r;t57r;t64r;t75r];

S7=[t47;t56;t65;t74];S7r=[t47r;t56r;t65r;t74r];

S8=[t04;t15;t26;t37];S8r=[t04r;t15r;t26r;t37r];

S9=[t05;t14;t27;t36];S9r=[t05r;t14r;t27r;t36r];

S10=[t06;t17;t24;t35];S10r=[t06r;t17r;t24r;t35r];

S11=[t07;t16;t25;t34];S11r=[t07r;t16r;t25r;t34r];

S12=[t40;t51;t62;t73];S12r=[t40r;t51r;t62r;t73r];

S13=[t41;t50;t63;t72];S13r=[t41r;t50r;t63r;t72r];

S14=[t42;t53;t60;t71];S14r=[t42r;t53r;t60r;t71r];

S15=[t43;t52;t61;t70];S15r=[t43r;t52r;t61r;t70r];

for i=0:15

   eval(['temp1=sort(dist(S' num2str(i) ',transpose(S' num2str(i) ')));']);

   eval(['temp2=sort(dist(S' num2str(i) 'r,transpose(S' num2str(i) 'r)));']);

   temp1=temp1(:,1).*temp1(:,1);

   temp2=temp2(:,1).*temp2(:,1);

   eval(['ns' num2str(i) '=sum(temp1>15.9 & temp1<16.1);'])

   eval(['nsr' num2str(i) '=sum(temp2>15.9 & temp2<16.1);'])

end

% There are 14 neighbours in each set at MSED=16

%

% Case II:  Need 64 subsets (32 from each group)

% to be used with the rate 5/6 encoder. Each subset has

% 8 8D points.

% For this we gather split the above into two so that the
```

```
% MSED is still 16.
for k=0:15
  eval(['u1' num2str(k) '(:,:)' ' = [S' num2str(k) '(1:8,:)];']);
  eval(['u2' num2str(k) '(:,:)' ' = [S' num2str(k) '(9:16,:)];']);
  eval(['u1' num2str(k) 'r(:,:)' ' = [S' num2str(k) 'r(1:8,:)];']);
  eval(['u2' num2str(k) 'r(:,:)' ' = [S' num2str(k) 'r(9:16,:)];']);
end
% Check the MSED and the N(dfree)
% The ED's are 0  4.0000 (6 times) and 5.6569 (1 time)
% There are 6 neighbours (for each point) at MSED=16.
for i=0:15
   eval(['temp1=sort(dist(u1' num2str(i) ',transpose(u1' num2str(i) ')));']);
   temp1=temp1(:,1).*temp1(:,1);
   eval(['nu1' num2str(i) '=sum(temp1>16-.1 & temp1<16+.1);']);
   eval(['temp2=sort(dist(u2' num2str(i) ',transpose(u2' num2str(i) ')));']);
   temp2=temp2(:,1).*temp2(:,1);
eval(['nu2' num2str(i) '=sum(temp2>16-.1 & temp2<16+.1);']);
   eval(['temp3=sort(dist(u1' num2str(i) 'r,transpose(u1' num2str(i) 'r)));']);
   temp3=temp3(:,1).*temp3(:,1);
eval(['nu1r' num2str(i) '=sum(temp3>16-.1 & temp3<16+.1);']);
   eval(['temp4=sort(dist(u2' num2str(i) 'r,transpose(u2' num2str(i) 'r)));']);
   temp4=temp4(:,1).*temp4(:,1);
eval(['nu2r' num2str(i) '=sum(temp4>16-.1 & temp4<16+.1);']);
end
% Now make only 16 subsets for rate 3/4 encoder
% MSED is now reduced to 10.34
% the ED's are:
% 3.2161 (8 times), 4.6537 (8 times); ie. the MSED is 10.3431.
% Finally 16 subsets are:
```

```
FS0=[S0;S5r];FS1=[S1;S4r];FS2=[S2;S0r];FS3=[S3;S1r];
FS4=[S4;S6r];FS5=[S5;S7r];FS6=[S6;S3r];FS7=[S7;S2r];
FS8=[S8;S10r];FS9=[S9;S11r];FS10=[S10;S8r];FS11=[S11;S9r];
FS12=[S12;S14r];FS13=[S13;S15r];FS14=[S14;S12r];FS15=[S15;S13r];
for i=0:15
   eval(['temp=sort(dist(FS' num2str(i) ',transpose(FS' num2str(i) ')));']);
   temp=temp(:,1).*temp(:,1);
eval(['nf' num2str(i) '=sum(temp>10.3 & temp<10.4);']);
end
% There are 8 neighbours at MSED=10.3431 in each of the 16 subsets
%
% Case 5:  Make 8 subsets, each made up of 64 points.
% This is used for an encoder with rate 2/3.
% For only 8 subsets, MSED becomes 8:
E0=[FS0;FS6]; E1=[FS1;FS7]; E2=[FS2;FS5]; E3=[FS3; FS4];
E4=[FS8;FS13];E5=[FS9;FS12]; E6=[FS10;FS15]; E7=[FS11;FS14];
for i=0:7
   eval(['temp=sort(dist(E' num2str(i) ',transpose(E' num2str(i) ')));']);
   temp=temp(:,1).*temp(:,1);
eval(['ne' num2str(i) '=sum(temp>7.9 & temp<8.01);']);
end
% there are 4 neighbours at MSED=8 in each of the 8 subsets
% (note this is 12 for the subset in my paper, 4, is of course, better.
%
% Case 6:
% For a rate 1/2 encoder we need 4 subsets; each subset
% has 128 points.  To do this, we recreate the above somewhat
% differently;  to obtain a total of 4, still with MSED=8.
% the new N(dfree) is now
```

```
e0=[S0;S1;S2;S3]; e1=[S4;S5;S6;S7];e2=[S8;S9;S10;S11];
e3=[S12;S13;S14;S15];
e4=[S0r;S1r;S2r;S3r]; e5=[S4r;S5r;S6r;S7r];
e6=[S8r;S9r;S10r;S11r];e7=[S12r;S13r;S14r;S15r];
for i=0:7
   eval(['temp=sort(dist(e' num2str(i) ',transpose(e' num2str(i) ')));']);
   temp=temp(:,1).*temp(:,1);
eval(['ne' num2str(i) '=sum(temp>7.9 & temp<8.01);']);
end
e01 = [e0;e1]; e23=[e2;e3]; e45=[e4;e5]; e67=[e6;e7];
% Check'd that MSED = 8 and N(dfree)= 28.
% Group above to have only 2 groups, if can keep MSED at 8, great.
e0167=[e01;e67];
e2345=[e23;e45];
```

Appendix F Partition into 8 subsets - Fading channels

The file QQ16Dgroups.mat contains the eight groups G1 through G8. This file is being sent along with the Matlab code in a separate package.

Appendix G   Partition into 16 subsets

```
% Partion code to maximize the symbol distance,

% Author: Milton I Quinteros

% Date:  02/16/11

% Updated: 02/20/11

%% Genration of points

clc

clear

%---------------------------------------------------------------------------

%Saha’s Constant Envelope Q2PSK Constellation

%These eight symbols are stored

%inside the variable S1

Sa1(:,1)=[1 1 1 -1];

Sa1(:,2)=[1 1 -1 1];

Sa1(:,3)=[1 -1 1 1];

Sa1(:,4)=[1 -1 -1 -1];

Sa1(:,5)=[-1 -1 -1 1];

Sa1(:,6)=[-1 -1 1 -1];

Sa1(:,7)=[-1 1 -1 -1];

Sa1(:,8)=[-1 1 1 1];

Sa1=Sa1’;


% Maximum E distances sets Sahas and Maximum Hamming Distance

Q1=[Sa1(1,1:4); Sa1(5,1:4)];

Q2=[Sa1(2,1:4); Sa1(6,1:4)];

Q3=[Sa1(7,1:4); Sa1(3,1:4)];

Q4=[Sa1(4,1:4); Sa1(8,1:4)];
```

```
c=sqrt(2);

Sb2(:,1)=[0 c c 0];

Sb2(:,2)=[0 c -c 0];

Sb2(:,3)=[c 0 0 c];

Sb2(:,4)=[c 0 0 -c];

Sb2(:,5)=[0 -c -c 0];

Sb2(:,6)=[0 -c c 0];

Sb2(:,7)=[-c 0 0 -c];

Sb2(:,8)=[-c 0 0 c];

Sb2=Sb2';


% Minimu E distances sets Cartwright and Maximum Hamming Distance

QR1=[Sb2(1,:); Sb2(3,:)];

QR2=[Sb2(2,:); Sb2(4,:)];

QR3=[Sb2(5,:); Sb2(7,:)];

QR4=[Sb2(6,:); Sb2(8,:)];


%%  8-D Saha's and Cartwright's constellations

%Saha's 8-D

% Q1 and Q1r

Q11=cartp(Q1,Q1);

Q12=cartp(Q1,Q2);

Q13=cartp(Q1,Q3);

Q14=cartp(Q1,Q4);

QR11=cartp(QR1,QR1);

QR12=cartp(QR1,QR2);

QR13=cartp(QR1,QR3);

QR14=cartp(QR1,QR4);
```

```
% Q2 and Q2r
Q21=cartp(Q2,Q1);
Q22=cartp(Q2,Q2);
Q23=cartp(Q2,Q3);
Q24=cartp(Q2,Q4);
QR21=cartp(QR2,QR1);
QR22=cartp(QR2,QR2);
QR23=cartp(QR2,QR3);
QR24=cartp(QR2,QR4);
% Q3 and Q3r
Q31=cartp(Q3,Q1);
Q32=cartp(Q3,Q2);
Q33=cartp(Q3,Q3);
Q34=cartp(Q3,Q4);
QR31=cartp(QR3,QR1);
QR32=cartp(QR3,QR2);
QR33=cartp(QR3,QR3);
QR34=cartp(QR3,QR4);
% Q4 and Q4r
Q41=cartp(Q4,Q1);
Q42=cartp(Q4,Q2);
Q43=cartp(Q4,Q3);
Q44=cartp(Q4,Q4);
QR41=cartp(QR4,QR1);
QR42=cartp(QR4,QR2);
QR43=cartp(QR4,QR3);
QR44=cartp(QR4,QR4);
```

```
% Grouping W
W1=[Q11; Q22; Q33; Q44];
W2=[Q12; Q23; Q34; Q41];
W3=[Q13; Q24; Q31; Q42];
W4=[Q14; Q21; Q32; Q43];

% Grouping WR
WR1=[QR11;QR33];
WR2=[QR22;QR44];
WR3=[QR12;QR34];
WR4=[QR23; QR41];
WR5=[QR13; QR31];
WR6=[QR24; QR42];
WR7=[QR14;QR32];
WR8=[QR21;QR43];



%% 16-D Saha's and Cartwright combination


%Sahas 16-D
W11=cartp(W1,W1);
W12=cartp(W1,W2);
W13=cartp(W1,W3);
W14=cartp(W1,W4);

W21=cartp(W2,W1);
W22=cartp(W2,W2);
W23=cartp(W2,W3);
W24=cartp(W2,W4);
```

```
W31=cartp(W3,W1);
W32=cartp(W3,W2);
W33=cartp(W3,W3);
W34=cartp(W3,W4);

W41=cartp(W4,W1);
W42=cartp(W4,W2);
W43=cartp(W4,W3);
W44=cartp(W4,W4);

%Carwrights 16-D
WR11=cartp(WR1,WR1);
WR12=cartp(WR1,WR2);
WR13=cartp(WR1,WR3);
WR14=cartp(WR1,WR4);
WR15=cartp(WR1,WR5);
WR16=cartp(WR1,WR6);
WR17=cartp(WR1,WR7);
WR18=cartp(WR1,WR8);

WR21=cartp(WR2,WR1);
WR22=cartp(WR2,WR2);
WR23=cartp(WR2,WR3);
WR24=cartp(WR2,WR4);
WR25=cartp(WR2,WR5);
WR26=cartp(WR2,WR6);
WR27=cartp(WR2,WR7);
WR28=cartp(WR2,WR8);
```

```
WR31=cartp(WR3,WR1);
WR32=cartp(WR3,WR2);
WR33=cartp(WR3,WR3);
WR34=cartp(WR3,WR4);
WR35=cartp(WR3,WR5);
WR36=cartp(WR3,WR6);
WR37=cartp(WR3,WR7);
WR38=cartp(WR3,WR8);

WR41=cartp(WR4,WR1);
WR42=cartp(WR4,WR2);
WR43=cartp(WR4,WR3);
WR44=cartp(WR4,WR4);
WR45=cartp(WR4,WR5);
WR46=cartp(WR4,WR6);
WR47=cartp(WR4,WR7);
WR48=cartp(WR4,WR8);


WR51=cartp(WR5,WR1);
WR52=cartp(WR5,WR2);
WR53=cartp(WR5,WR3);
WR54=cartp(WR5,WR4);
WR55=cartp(WR5,WR5);
WR56=cartp(WR5,WR6);
WR57=cartp(WR5,WR7);
WR58=cartp(WR5,WR8);
```

```
WR61=cartp(WR6,WR1);

WR62=cartp(WR6,WR2);

WR63=cartp(WR6,WR3);

WR64=cartp(WR6,WR4);

WR65=cartp(WR6,WR5);

WR66=cartp(WR6,WR6);

WR67=cartp(WR6,WR7);

WR68=cartp(WR6,WR8);


WR71=cartp(WR7,WR1);

WR72=cartp(WR7,WR2);

WR73=cartp(WR7,WR3);

WR74=cartp(WR7,WR4);

WR75=cartp(WR7,WR5);

WR76=cartp(WR7,WR6);

WR77=cartp(WR7,WR7);

WR78=cartp(WR7,WR8);


WR81=cartp(WR8,WR1);

WR82=cartp(WR8,WR2);

WR83=cartp(WR8,WR3);

WR84=cartp(WR8,WR4);

WR85=cartp(WR8,WR5);

WR86=cartp(WR8,WR6);

WR87=cartp(WR8,WR7);

WR88=cartp(WR8,WR8);



%-------------------------Grouping 16D Types-----------------------------
```

```
G1=[WR11;WR22; WR55; WR66];

G2=[WR12;WR21; WR56; WR65];

G3=[WR13;WR24; WR57; WR68];

G4=[WR14;WR23; WR58; WR67];

G5=[WR15;WR26; WR51; WR62];

G6=[WR16;WR25; WR52; WR61];

G7=[WR17;WR28; WR53; WR64];

G8=[WR18;WR27; WR54; WR63];


G9=[WR31;WR42; WR75; WR86];

G10=[WR32;WR41; WR76; WR85];

G11=[WR33;WR44; WR77; WR88];

G12=[WR34;WR43; WR78; WR87];

G13=[WR35;WR46; WR71; WR82];

G14=[WR36;WR45; WR72; WR81];

G15=[WR37;WR48; WR73; WR84];

G16=[WR38;WR47; WR74; WR83];


%---------------------------------------------------------------------------



%% Grouping for mapping with msd of 8 and mhd of 4 called C-group

% 16 Groups of 512 points each with Minimum Hamming distance of 4.

F1=[G1;W11];

F2=[G2;W12];

F3=[G3;W13];

F4=[G4;W14];

F5=[G5;W21];

F6=[G6;W22];
```

```
F7=[G7;W23];

F8=[G8;W24];


F9=[G9;W31];

F10=[G10;W32];

F11=[G11;W33];

F12=[G12;W34];

F13=[G13;W41];

F14=[G14;W42];

F15=[G15;W43];

F16=[G16;W44];
```

Appendix H Coauthor Copyright Letter

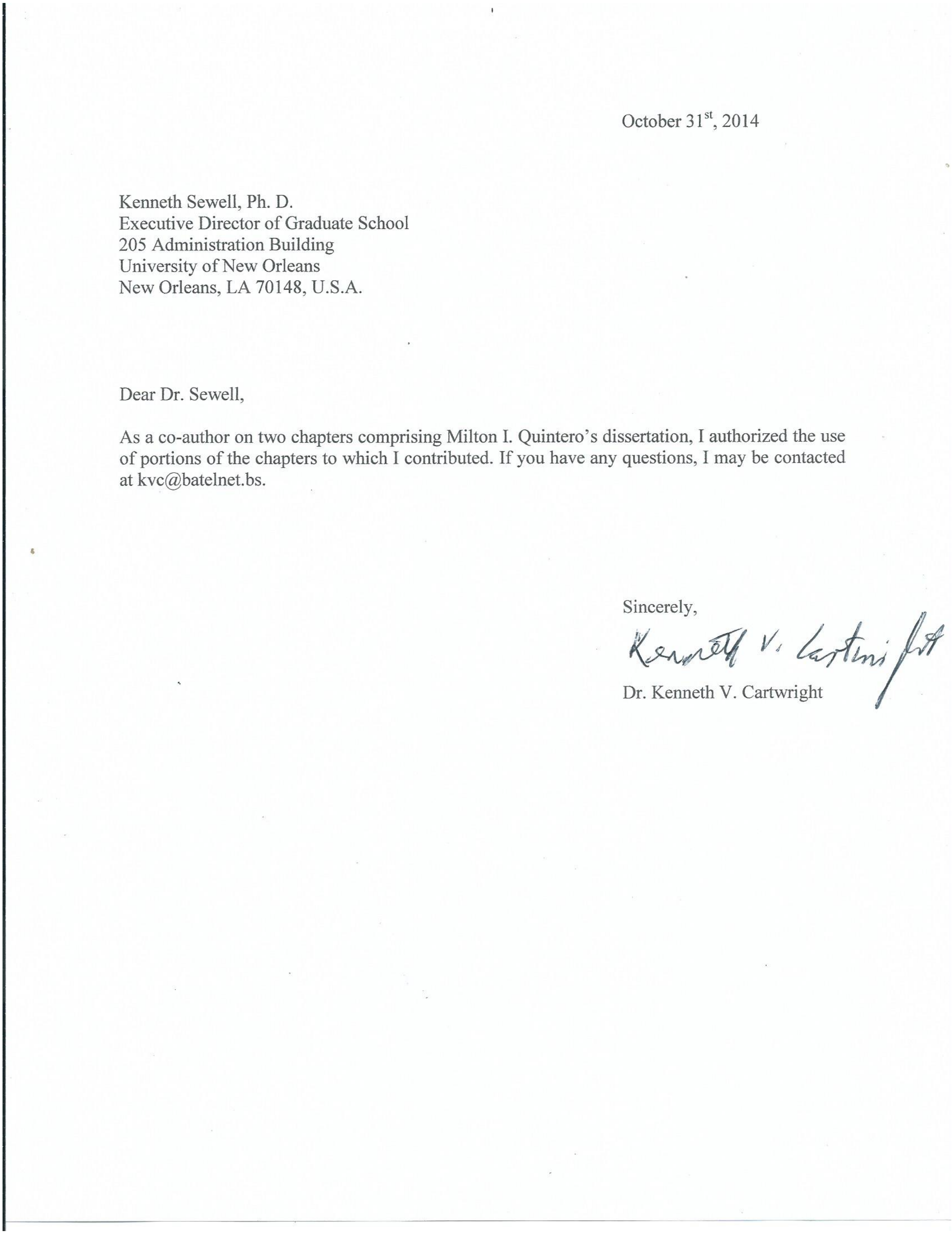

October 31st, 2014

Kenneth Sewell, Ph. D.
Executive Director of Graduate School
205 Administration Building
University of New Orleans
New Orleans, LA 70148, U.S.A.

Dear Dr. Sewell,

As a co-author on two chapters comprising Milton I. Quintero's dissertation, I authorized the use of portions of the chapters to which I contributed. If you have any questions, I may be contacted at kvc@batelnet.bs.

Sincerely,

Kenneth V. Cartwright

Dr. Kenneth V. Cartwright

Vita

Milton Quinteros was born on August 4, 1982, in Guayaquil, Ecuador. He received a Bachelor of Science in Electrical Engineering in May 2007 and his Master of Science in Electrical Engineering in May 2009 from the University of New Orleans. He began working on his Doctoral Degree at the same University on August 2009 under Dr. Edit J. Kaminsky Bourgeois as major professor. He worked at the Intensive English Language Program (IELP) as a student worker from 2003 to 2005, where he suggested the design of a Web-Database application system to keep records of the students, and helped to efficiently transfer data from Access to SQL-server 2005. He worked as a Research Assistant in Electrical Engineering under three research grants: The 16-D Trellis Encoded CEQ^{2}PSK over non-linear mobile communication channels funded by SPAWAR innovations Program with Dr. Edit J. Kaminsky as Principal Investigator (PI), Feature Analysis for Classification of Fish in Underwater Image Sequences funded by National Oceanic and Atmospheric Administration (NOAA) with Dr. Dimitrious Charalambidis, Dr. George E. Ioup, and Dr. Juliette W. Ioup as PIs, and Test Plan Automation for Different Power Protection schemes by Entergy-UNO Research Agreement with Dr. Parviz Rastgoufard as PI. In addition, Milton Quinteros was Adjunct Professor for Escuela Superior Politecnica (ESPOL) in May 2010, and Adjunct Professor for the University of New Orleans in May 2011, and May 2012. His research areas include Digital Telecommunications, Data Base design, Neural Networks, and Digital System Controls. He is currently working as contractor Engineer for IK Power Systems Solutions Inc.